Event-by-Event Fluctuations in Charged Particle Production in Au+Au Collisions at $\sqrt{s_{NN}} = 130$ GeV

Erik S. Jakobsen

Niels Bohr Institute
University of Copenhagen

December 7, 2001

Thesis presented for the Cand. Scient. degree.

Supervisor: Jens Jørgen Gaardhøje

Preface

I wrote my Bachelor thesis on time of flight measurements in the BRAHMS experiment. I have been working with the experimental High Energy Heavy Ion physics group at the Niels Bohr Institute since then. During this period, I have got to know many people from the BRAHMS collaboration whom I would like to thank for their help and support.

I owe a special thanks to Jens Jørgen Gaardhøje and Henning Heiselberg for guidance, discussions and encouragements. Also a special thank to Christian Holm for discussions and for teaching me principles of analysis. My thanks also go to Claus Ekman Jørgensen, Peter Christiansen, Djamel Ouerdane, Ian Bearden, Hans Bøggild, Flemming Videbæk, Ole Hansen, Anders Holm, Pawel Staszel, David Sandberg and Mads Gammeltoft for discussions and corrections.

Finally I would like to thank Gert Jacobsen, Karen Jacobsen and Louise Hauerberg for their continuous support during the entire process.

Copenhagen, December 2001

Erik Jakobsen

Contents

List of Figures

List of Tables

Chapter 1

Introduction

The purpose of modern heavy ion physics is to study the properties of very hot and dense nuclear matter. It is believed that quark-gluon plasma can be created for a short time (10^{-23} to 10^{-22} sec) in ultra relativistic collisions of heavy ions. The search for and study of this plasma has been the motivation for building the Relativistic Heavy Ion Collider (RHIC) at Brookhaven National Laboratory. In the summer of year 2000 RHIC began colliding gold nuclei at $\sqrt{s_{NN}} = 130$ GeV. The first results were eagerly awaited, since this energy was more than a factor 7 higher than what was previously achieved at the CERN SPS accelerator.

There are four experiments at RHIC (BRAHMS, PHOBOS, PHENIX and STAR), which will be discussed in section 2.6. The analysis of fluctuations in this thesis is based on data from the first period of running (∼2 weeks in year 2000) at $\sqrt{s_{NN}} = 130$ GeV from the BRAHMS experiment.

The aim of this thesis is to examine fluctuations of the charged particle multiplicity density. Fluctuations in physical observables in ultrarelativistic heavy ion collisions is becoming a more and more interesting topic as it may provide new signals regarding the formation of a quark-gluon plasma. It is believed that supercooling in a first order phase transition, may cause density fluctuations resulting in droplet formations, which may be detected in a rapidity distribution. At $\sqrt{s_{NN}} = 130$ GeV approximately 4000 new particles were produced in each collision, which makes it feasible to study fluctuations in charged particle multiplicity density on an event-by-event basis.

In chapter 2 the theoretical framework for quark-gluon plasma formation is presented. The basic concepts of heavy ion collisions are described. RHIC and the BRAHMS experiment is described in chapter three. Chapter four describes the simulation program BRAG and the event generators FRITIOF 7.02 and HIJING, that have been used in the analysis. The analysis for the multiplicity and fluctuations are described in chapters 5 and 6, respectively. Chapter 7 summarizes and discusses the analysis results and finally the conclusion if found in chapter 8.

Throughout the thesis common variables will be used. Definitions of these can be found in appendix A. Appendix B contains information on how to use FRITIOF and HIJING event generators. Instructions on how to use BRAG and make detectors inactive are also found in this appendix. In the end of appendix B some omitted graphs in section 5.6 are showed. In appendix C the statistical error on the fluctuation is calculated and in appendix D the *participant model* is discussed. In appendix E figures from the impact parameter fluctuation and the intrinsic fluctuation analysis are found. Finally in appendix F the BRAHMS collaboration is listed.

Chapter 2

Quark-Gluon Plasma & Heavy Ion Collisions

2.1 The Early Universe

Accordingly to current astrophysical and cosmological knowledge, the Universe was created about 15 billion years ago. So far, nobody knows what happened *before* the beginning, but the Big Bang theory entails that the Universe evolved from a singularity with an infinite temperature and density. Measurements of the microwave background radiation, the description of the expanding universe by Hubble and the abundance of light elements have confirmed the theory of an expanding universe, but many questions are still unanswered. Assuming that the Universe has evolved adiabatically and in equilibrium, one can extrapolate back to t = 10^{-43} second. The temperature and density would at this time have been 10^{19} GeV and 10^{97}g/cm^3, respectively [1]. As the Universe expanded and cooled, the temperature and energy density decreased and at approximately t = 10^{-5} second, the quarks and gluons became confined by the strong interaction, and so hadronic matter, such as baryons (qqq or $\bar{q}\bar{q}\bar{q}$) and mesons ($q\bar{q}$), was created for the first time. It is the reproduction of the phase transition, from quark-gluon plasma to confined hadrons, that is a main goal of ultra relativistic heavy ion physics [2].

2.2 Quantum Chromo Dynamics

So far it has not been possible to liberate a *single* quark from the hadrons. It seems that the quarks are *confined* in regions with the size of hadrons. Furthermore it has been revealed in deep inelastic scattering experiments that the quarks at very short distances move almost freely, as if they were not bound at all [3]. This is often referred to as the *asymptotic freedom.* The theory that describes the strong interaction between the quarks is called *quantum chromo dynamics*, QCD. Without going into details of this complex theory, a description of the distinguishing features in this theory is presented in the following.

QCD introduces a color field in analogous with the electric field, known from *quantum*

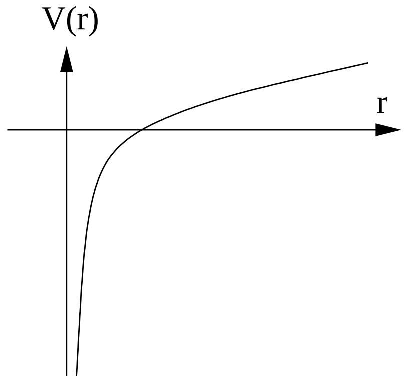

Figure 2.1: The potential between quarks. At small distances (r) the potential becomes insignificant. For larger r, the potential grows proportionally to r.

electro dynamics, QED. In QCD there are three color charges; red, green and blue (r, g or b), where as QED only has one - the electrical charge. The hadrons are color neutral objects, which means that the quarks in a baryon are described as a composition of a red, green and a blue quark (r, g and b). The quark in a meson has a color (r, g or b) and the anti quark has the corresponding anti color ($\bar{r}, \bar{g}$ or $\bar{b}$). The field carriers in QCD are called gluons. They carry color charge and it is possible for them to self interact. The color charged gluons makes QCD complex to describe mathematically. In QED an electron does not change its charge if photons are emitted. If a quark emits a gluon, it must itself change color charge. The color charge is therefore *smeared out* as a sphere with a radius of 0.5 to 1 fm. If another quark moves within this *smeared* volume, the color field will be reduced. If the distance is small compared to 1 fm, only a small fraction of the color charge will be observed and it would appear that the two quarks are almost free. This is what is understood by *asymptotic freedom* [3, 4].

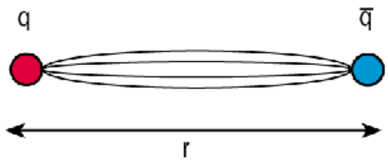

Figure 2.2: The field between two quarks.

The possibility of gluon-gluon interactions, gives rise to the linear part of the potential at long distances, shown on figure 2.1. The gluon-gluon interactions forces the color field between two quarks into a tube at larger distances, i.e. $r > 1$ fm, as shown in figure 2.2. The energy density in the tube is roughly constant, as r increases. At some distance, it will be energetically favorable to create a $q\bar{q}$ pair. Therefore will an attempt to isolate quarks only lead to production of more quarks. This is what is understood by *confinement* [3, 5].

2.3 Quark-Gluon Plasma

Inside the nucleon, the quarks are bound by the color field from the gluons, as described in the previous section. Imagine that the nucleon density increases, so the boundaries of the quarks would overlap. The color field would break up and the quarks would then be in a collective state and the hadrons would effectively loose their identity. This is illustrated in figure 2.3.

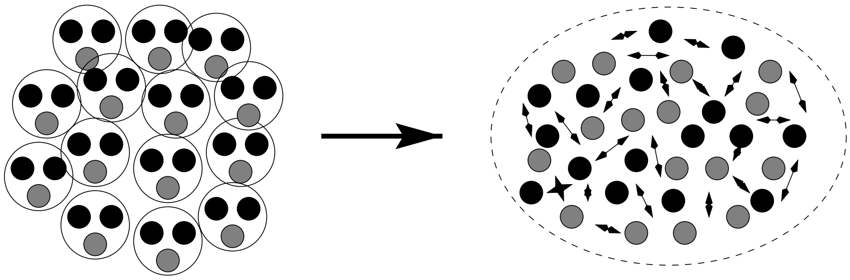

Figure 2.3: To the left quarks are confined in in hadrons. To the right the density has increased and it is believed that the quarks and gluons will form a quark-gluon plasma [6].

The effect is called *color screening*, and is similar to *Debye screening* in QED, where the Coulomb potential screens the charged particles from other charged particles.

Lattice QCD calculations and the MIT bag model predicts a phase transition from hadronic matter to QGP at high temperatures and densities. This is illustrated in figure 2.5. The calculations predicts a phase transition at $T_c \simeq 150$ MeV for low densities and for low temperature at a critical density of $\rho_c = 5 - 10$ GeV/fm^3 [7] [8].

Four different situations where matter can be in the QGP phase state is illustrated in figure 2.4. The arrow pointing downwards indicates the possibility of QGP in the early Universe, as mentioned in section 2.1 on page 3. The other solid line shows how a very dense region in a neutron star[1] may contain a *cold* QGP. The lower dashed line indicate relativistic heavy ion collisions at the two experiments, AGS ($\sqrt{s_{NN}} = 5$ GeV) at BNL and the SPS ($\sqrt{s_{NN}} = 17$ GeV) at CERN. The upper dashed lines shows what is expected at the two colliders, RHIC at BNL ($\sqrt{s_{NN}} = 200$ GeV) and LHC at CERN which will open in 2006 and is designed for $\sqrt{s_{NN}} = 5.5$ TeV.

2.4 Nuclear Collisions

In the following sections the basic concepts of relativistic nuclear collisions will be briefly described.

[1] A neutron star is great gravitationally bound nucleus of the order of one solar mass and is the remnants of a supernova explosion.

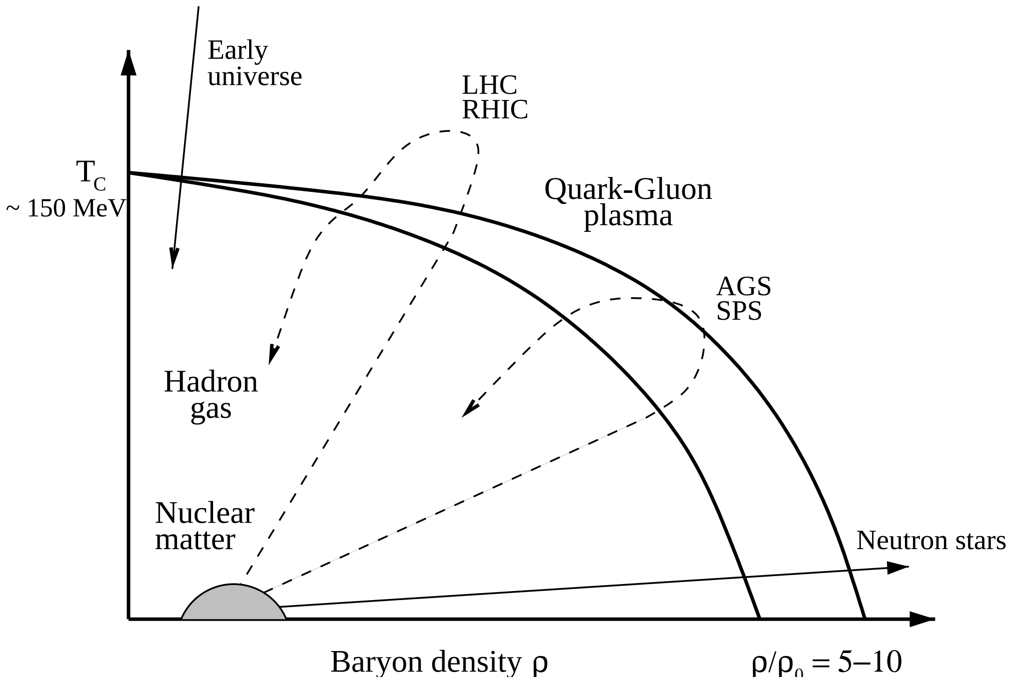

Figure 2.4: Phase diagram for nuclear matter. The hadron gas and the QGP are separated by a transition zone. Nuclear density (ρ_n) is approximately 0.15 baryons/fm^3.

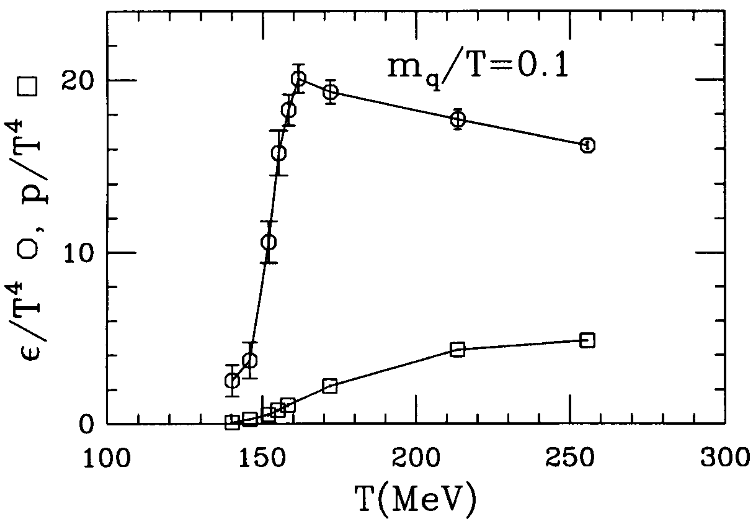

Figure 2.5: QCD lattice calculations based on light quark flavors. The circles show the energy density ϵ/T^4 and the squares show the pressure P $/T^4$ as a function of temperature [8].

2.4.1 Collision Geometry

When two nuclei collide at relativistic energies, they will appear Lorentz contracted when viewed from the center of mass (CM) system, as seen in figure 2.6. This is the situation in the laboratory frame at RHIC where, for symmetric collision e.g. Au+Au, the CM is at rest in the laboratory frame of reference. At $\sqrt{s_{NN}} = 130$ GeV each nucleon sees the approaching nucleon with a speed corresponding to a γ factor of 9600. Because of the high energy it is expected that only the particles in the overlapping region will interact. The interacting matter is called the participating matter, where as the non-interacting matter is referred to as the spectator matter, and thus the name of the model: *The participant-spectator model.* The larger the participating zone is, the more energy is available and therefore more particles are produced. At lower energies than RHIC, the participant zone is also often referred to as the *fireball.*

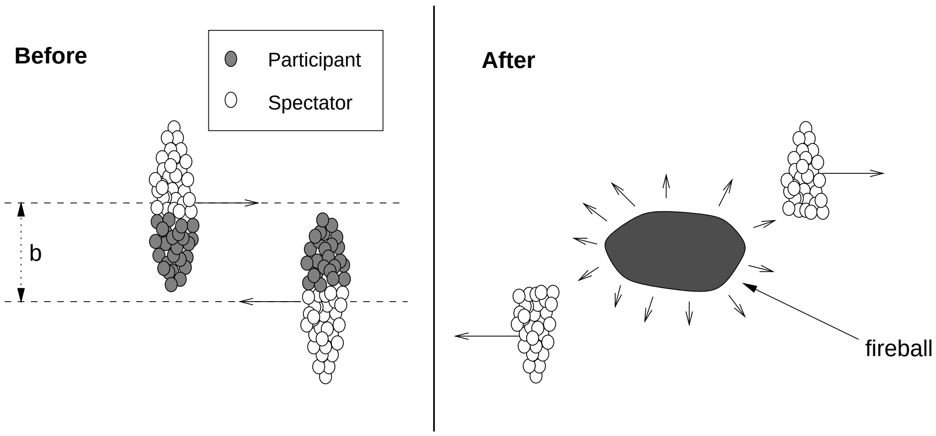

Figure 2.6: The participant-spectator model. The impact parameter b is the radial distance between the centers of the two nuclei [9].

The size of the participant zone depends on the centrality of the collision, which can be measured by the impact parameter b, i.e. the transverse distance between the center of the two nuclei. The number of particles produced is therefore dependent on b. Experimentally b is not measured, and so experimentalists often refer to a centrality percentage.

The centrality is experimentally determined by evaluating the particle production, the *multiplicity.* A high multiplicity corresponds to a central event, and so by investigating a large ensemble of events, one can identify events within a given centrality percentage range. Centrality determination is discussed in section 5.5.

The relation between the number of participants and the impact parameter based on a HIJING simulation is shown in figure 2.7. Various centrality cuts are shown on the top figure.

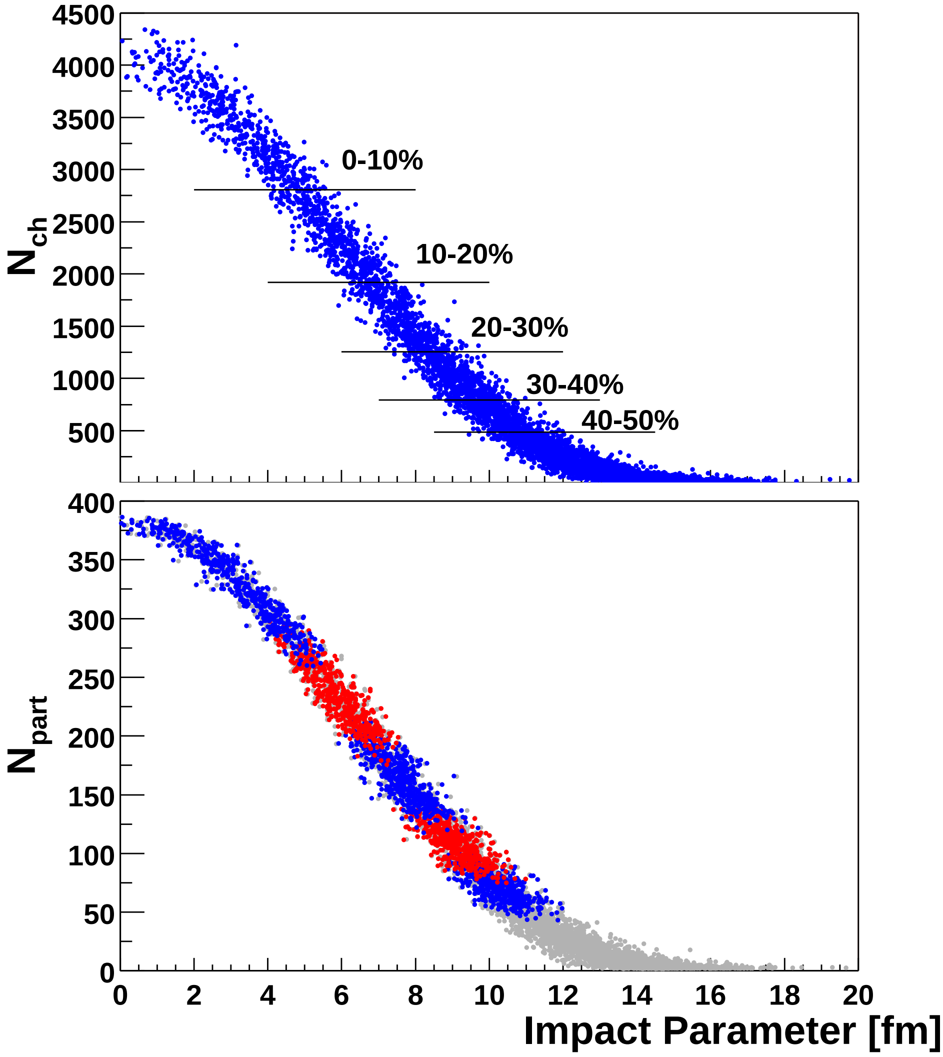

Figure 2.7: HIJING simulation showing number of participants as a function of impact parameter measured in fermi for Au + Au collisions at $\sqrt{s_{NN}} = 130$ GeV. Upper panel shows number of charged particles vs. impact parameter for various centrality cuts. Lower panel shows number of participants vs. impact parameter [10]. Experimental collision centrality is often done by selecting fractions of the total multiplicity distribution for charged particles, as shown on top. The conversion to impact parameter is unfortunately ambiguous and model dependent.

2.4.2 Collision Scenarios

Two extreme scenarios are useful to illustrate relativistic heavy ion collisions: The stopping scenario and the transparent scenario. Stopping is when the two colliding nuclei are fully stopped and all the kinetic energy is converted into internal degrees of freedom in the collision zone. This scenario is illustrated in figure 2.8 and can be described by the Landau model [11]. Nuclear collisions at low energies will experience a high degree of stopping [12].

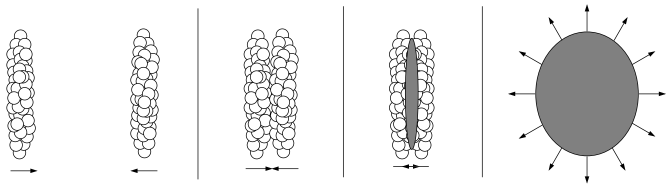

Figure 2.8: The stopping scenario. The two nuclei are viewed orthogonal to the beam axis and they therefore appear Lorentz contracted to the observer.

The transparency scenario, shown in figure 2.9, assumes that the energy available in the collision is so large, that the *formation time* (τ_0) for new particles to be created, is larger than the time it takes for the two nuclei to pass each other. Thus the new particles are first created after the nuclei have passed. In order to have a transparent scenario, the requirement is

$$\gamma \geq \frac{2R}{c\tau_0} \tag{2.1}$$

where R denotes the nucleon radius and $\tau_0 \simeq \hbar/m_\pi c^2$. For gold $R \simeq 14$ fm. The predicted energy for a scenario that is dominantly transparent is at $\sqrt{s_{NN}} \geq 100$ GeV.

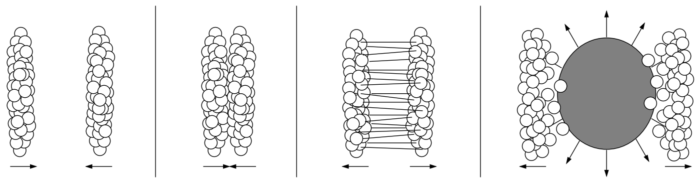

Figure 2.9: The transparent scenario. The two Lorentz contracted nuclei are transparent to each other. The color field created after penetration condensates and a region of hot and dense matter is created.

A way to determine the degree of transparency or stopping in a collision, is to examine the anti-particle to particle ratios. The ratio $N(\bar{p})/N(p)$ has been measured at several experiments [13, 14], as shown on figure 2.10. Because of baryon number conservation, there are created an equal number of particles and anti-particles in the collision. If more protons than anti-protons are measured, it indicates that some of the primary protons are among the measured protons, and that the collision can be described with a high degree of *stopping*. Therefore the ratio $N(\bar{p})/N(p)$ at midrapidity should be less than one, if some of the primary nucleons are stopped. If the collision is completely transparent the ratio $N(\bar{p})/N(p) = 1$, because none of the primary protons are shifted from the beam rapidity to midrapidity.

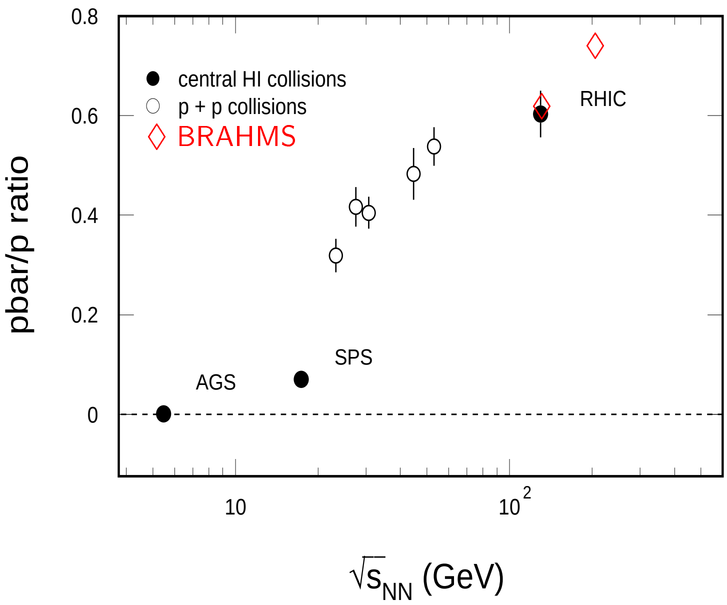

Figure 2.10: The ratio $N(\bar{p})/N(p)$ as a function of $\sqrt{s_{NN}}$ at midrapidity for several experiments, including BRAHMS data at RHIC taken at $\sqrt{s_{NN}}$ = 130 GeV and 200 GeV. Error bars for BRAHMS are not shown, but the value for $\sqrt{s_{NN}}$ = 130 GeV is $N(\bar{p})/N(p) = 0.64 \pm 0.04_{stat.} \pm 0.06_{syst.}$ and for $\sqrt{s_{NN}}$ = 200 GeV the ratio is $0.75 \pm 0.06_{syst.}$ (preliminary). At low energies the two nuclei are experiencing a high degree of stopping. As the energy increases the collision scenario becomes more transparent [13, 14].

Information on the charge distribution of the collision zone, can be extracted from the ratios $N(\pi^-)/N(\pi^+)$ and $N(K^-)/N(K^+)$ as a function of transverse energy. In heavy ion collisions the ratios should be 1 at midrapidity, because the charge of the primary protons are at higher rapidities [15].

The Bjorken Scenario

In 1983 Bjorken described the transparent scenario with his famous space-time picture of relativistic nuclear collisions, shown on figure 2.11. At a time of the order 1 fm/c ($\sim 3 \cdot 10^{-24}$ s) after the collision, partons are created in the color dense region. This time is called the *formation time*. After a few fm/c the system has expanded so much, that the temperature has dropped to the critical value T_c (~ 150 MeV). If the phase transition occurs at this point, the system will stay in the *mixed phase* for 10 fm/c. The phase with hadron gas exists until the mean free path between the hadrons is large enough in order for interactions to cease. The hadrons will then stream out from the collision zone. This time is referred to as the *freeze out time*. The number of particles produced are related to the amount of energy in the collision zone [16].

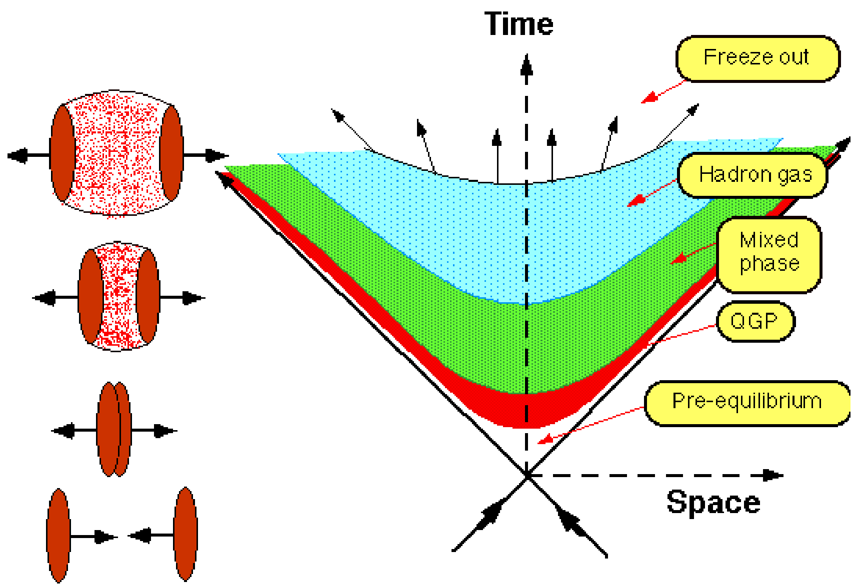

Figure 2.11: The Bjorken scenario. A space-time evolution in longitudinal direction of the quark-gluon plasma. The different stages of the expansion are shown.

2.5 Quark-Gluon Plasma Signatures

What signals can be interpreted as signatures of the quark-gluon plasma? In the following sections some of the proposed signatures will be reviewed, and results from SPS will be shown and discussed.

2.5.1 J/Ψ Suppression

It has been predicted [17] that the production of the J/Ψ meson ($c\bar{c}$) will be suppressed in a quark-gluon plasma. In a QGP the c and $\bar{c}$ are free to move around and since there are more light quarks (u and d) in the collision zone, it is more likely that c and $\bar{c}$ will bind to them, than creating a J/Ψ. The creation of a D ($c\bar{u}$), or $\overline{D}$, is thus more probable. If a QGP is created, the production of D mesons will be enhanced and the production of J/Ψ will be suppressed. The short life time of the D mesons ($\simeq 10^{-12}$ second), it is hard for experimentalists to detect whether the measured D mesons come from decay products or the collision zone, since the decay length is only 0.3 mm. But high momentum can boost lifetime, i.e. $\gamma = 10 \Rightarrow 3$ mm. This can be done at the ALICE [18].

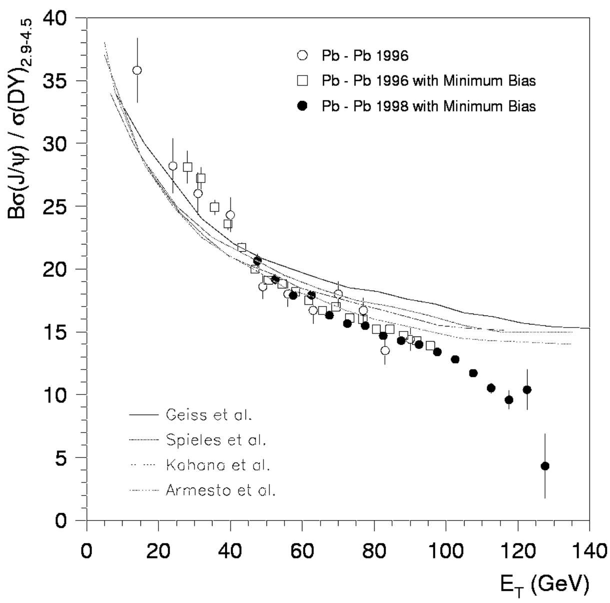

Figure 2.12: NA50 measured J/Ψ to the Drell-Yang cross section as a function of the transverse energy. The lines show different calculations of suppression based on nuclear absorption [19].

J/Ψ can be detected by evaluating the $\mu^+\mu^-$ decay. CERN claimed evidence that this effect has been found at the NA50 experiment in Pb + Pb collisions, as shown in figure 2.12. The figure shows that the observed cross section is below various model calculations. The interpretation that a quark-gluon plasma state had been created at SPS has so far not been accepted yet [20].

2.5.2 Strangeness Enhancement

In heavy ion collisions, the only quarks present before the collision are u and d quarks, the constituents of the two colliding nuclei. All measured particles containing s quarks, has therefore been created in the collision. The most abundant particles that contain s quarks are the kaons, i.e. $K^+(u\bar{s})$, $K^-(\bar{u}s)$, $K^0(d\bar{s})$ and $\overline{K}^0(\bar{d}s)$. 70% of the of the s quarks leave the collision zone in these kaons [9].

The mass of the s quark is 60 - 170 MeV/c^2, which is more than the u (1.5 - 5 MeV/c^2) and d (3 - 9 MeV/c^2). Therefore production of the heavier $s\bar{s}$ is energetically unfavorable. If a quark-gluon plasma is formed, the density of u and d quarks is high and because of Pauli blocking of the $u\bar{u}$ and $d\bar{d}$ states on the production of $s\bar{s}$ will be favored leading to an enhancement relative to scaled p+p collisions.

Strangeness enhancement has been measured by several experiments, i.e. NA44 [21] and the WA98 collaboration [22], as shown on figure 2.13. The top figures show the net enhancement of particles containing strange particles, relative to p + Be collisions versus number of participating nucleons. The bottom show the same divided by the number of participating nucleons. The results indicate at these lower plots a threshold behavior, which could be expected if a phase transition occurred.

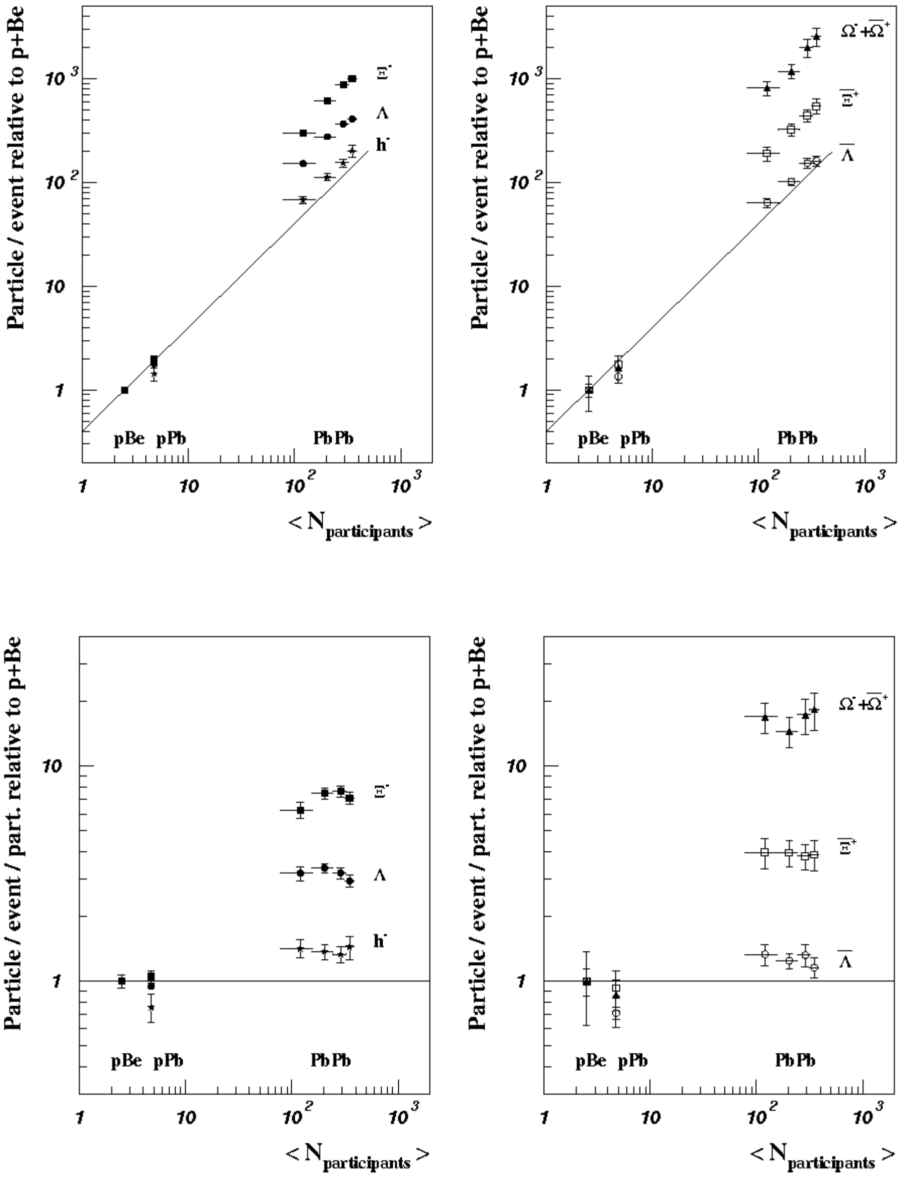

Figure 2.13: Measurements of strangeness production at SPS energies. The production of strange particles is enhanced relative to p + Be collisions [22].

2.5.3 Jet Quenching

If a quark-gluon plasma is formed, it is predicted that high momentum quarks and gluons moving through the dense partonic medium (quarks and gluons) will have a smaller p_t because of the induced energy loss. This effect is called *jet quenching*. This may be measured as a suppression of high p_t hadrons. The energy loss proceeds in multiple scattering between the partons which induces a broadening in transverse momentum of the jet. Thus *jet quenching* can be experimentally studied by measuring total transverse momentum broadening. At CERN experiments such as the WA98 collaboration [23] have attempted to measure *jet quenching*, but did not succeed in detecting this phenomenon.

2.6 RHIC Results

With the opening of RHIC in the summer 2000 new physics were awaited. The four experiments have since then published several articles. Some of these will be discussed in the following.

2.6.1 STAR

The Solenoidal Tracker At RHIC (STAR) [24] is basically a large cylindrical time projection chamber[2] inside a large solenodial magnet. Figure 2.14 show reconstructed tracks seen perpendicular to the beam.

STAR measures charged particles within the pseudorapidity range of $|\eta| \leq 1.8$. STAR has in [25] measured an increase in particle production of 52% at midrapidity, when compared to nuclear collisions at $\sqrt{s_{NN}} = 17$ GeV (CERN). This is illustrated in figure 2.15. Measured midrapidity multiplicity is mentioned in section 2.6.5.

2.6.2 PHENIX

The PHENIX experiment has focused on electro magnetic signals. The experiment consists of different detector subsystems divided into two central spectrometers, and a number of inner detectors that measure the vertex, start time and multiplicity. Figure 2.16 shows the detector setup. PHENIX has published results of measured transverse energy density at midrapidity. They conclude that the energy distribution at $\sqrt{s_{NN}} = 130$ GeV for central collisions is at least 1.6 times higher than at $\sqrt{s_{NN}} = 17.2$ GeV measured at CERN [26].

PHENIX has also measured suppression of hadrons with large transverse momentum at $\sqrt{s_{NN}} = 130$ GeV [27]. They conclude that for central and peripheral collisions that the spectra are suppressed when compared to scaled p+p expectations, which may indicate new nuclear effects at RHIC energies.

[2] Description of such detector can be found in section 3.2.6.

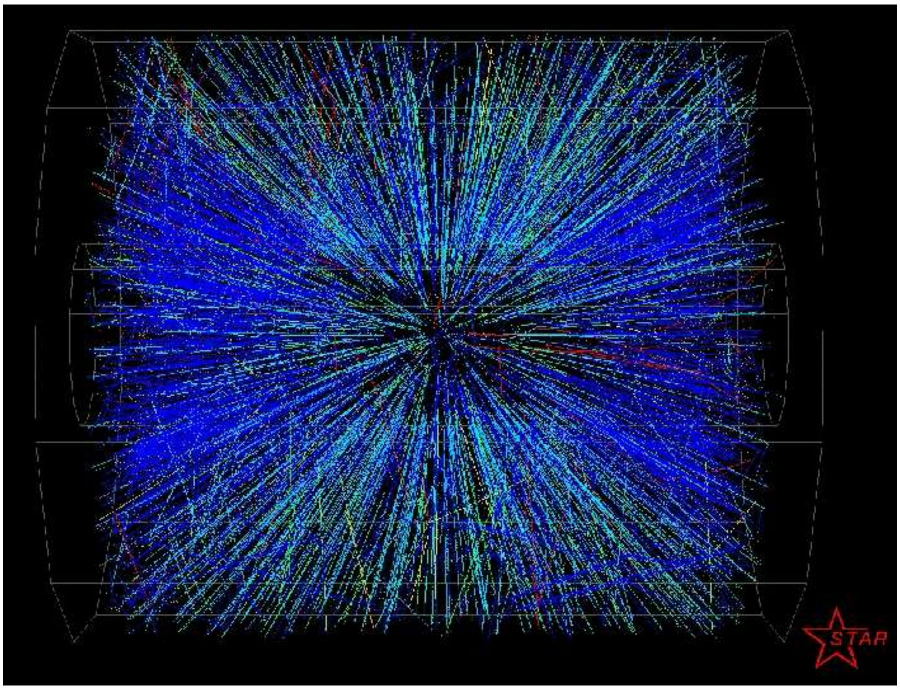

Figure 2.14: STAR event image showing one collision seen perpendicular to beam pipe.

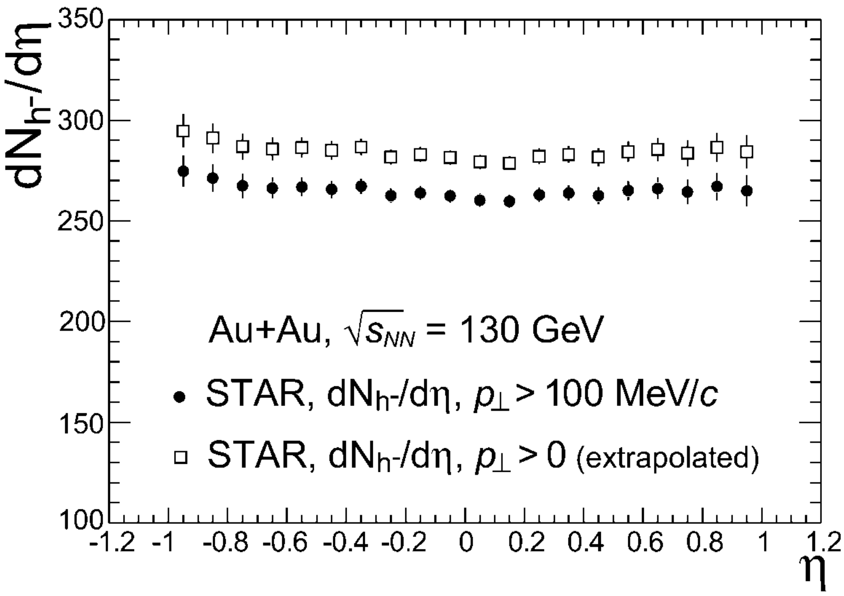

Figure 2.15: $dN/d\eta$ for negatively charged hadrons measured in STAR for the 5% most central events [25].

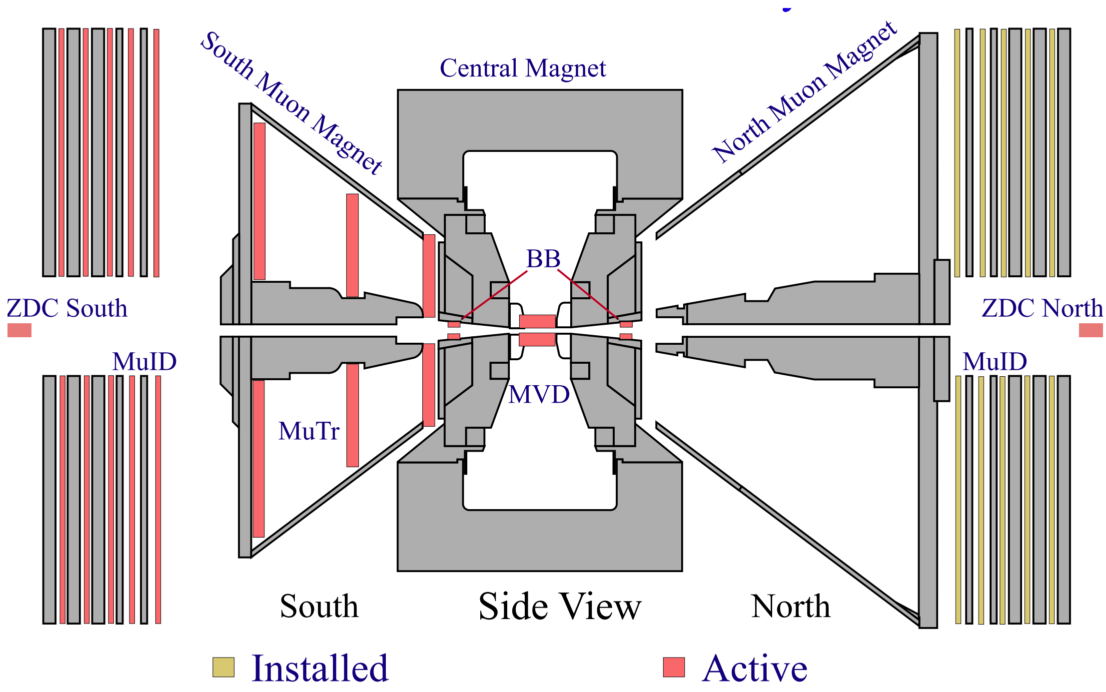

Figure 2.16: PHENIX detector setup for year 2001 physics run [29].

2.6.3 PHOBOS

The PHOBOS experiment is designed to detect a large number of particles at low p_t. It consists of a cylindrical array of silicon detectors and two spectrometer arms surrounding the interaction region, as shown in figure 2.17. PHOBOS has published $N(\bar{p})/N(p)$ at 0.60 $\pm 0.04(stat.) \pm 0.06(syst.)$ in the transverse momentum range of $0.15 < p_t < 1.0$ GeV/c [28].

2.6.4 BRAHMS

The BRAHMS experiment which will be described in chapter 3 has measured $N(\bar{p})/N(p)$ to 0.64 $\pm 0.04(stat.) \pm 0.06(syst.)$ at $y \simeq 0$ for 0-40% central events [13]. Ratios were also found at $y \simeq 0.7$ and $y \simeq 2$ to be respectively 0.66 $\pm 0.03(stat.) \pm 0.06(syst.)$ and 0.41 $\pm 0.04(stat.) \pm 0.06(syst.)$. The ratios are almost independent of collision centrality and transverse momentum. The results indicate a high degree of transparency in the collision, even though the transparent *Bjorken limit* were not reached. In figure 2.18 the measured charge particle distribution at $\sqrt{s_{NN}} = 130$ GeV is shown for different centrality ranges. This result was published in [31]. A preliminary plot for the charged particle multiplicity at $\sqrt{s_{NN}} = 200$ GeV is shown in figure 2.19.

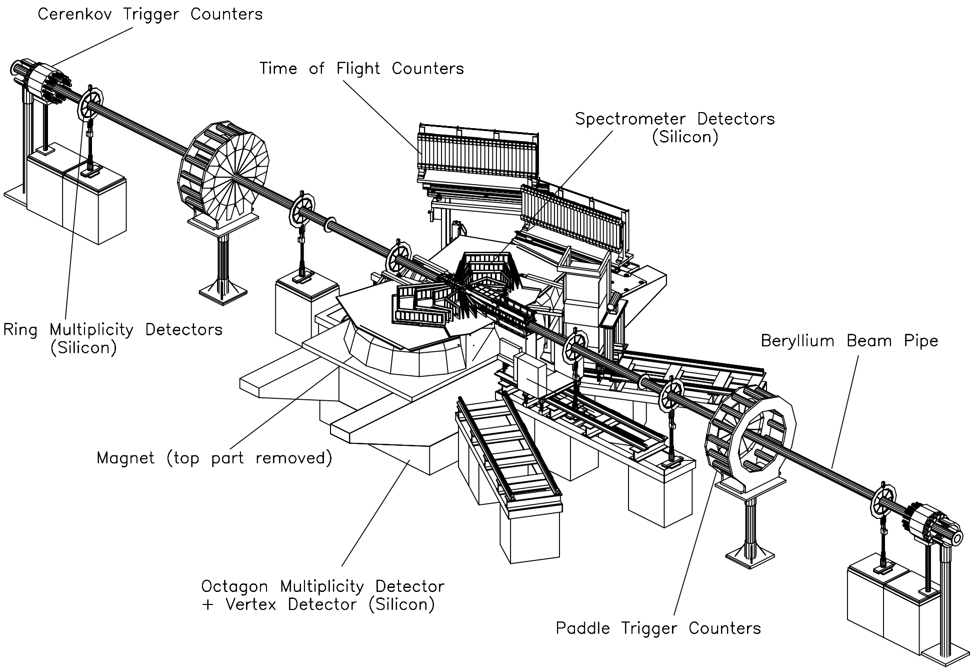

Figure 2.17: PHOBOS detector setup for first run period. Only lower half of the magnet is shown [30].

2.6.5 Measured RHIC Multiplicities

Table 2.1 summarizes the measured charged multiplicities for the most central events at $\sqrt{s_{NN}} = 130$ GeV from BRAHMS, PHENIX, PHOBOS and STAR. Within the uncertainty, the measured multiplicities agree, even though the experimental setup is very different for the RHIC experiments.

Experiment	$dN_{ch}/d\eta$	Centrality
BRAHMS	553 ±36(syst.)	5%
PHENIX	622 ±1(stat.) ±41(syst.)	5%
PHOBOS	555 ±12(stat.) ±35(syst.)	6%
STAR	567 ±1(stat.) ±38(syst.)	5%

Table 2.1: Measured RHIC multiplicities at midrapidity at $\sqrt{s_{NN}} = 130$ GeV from the BRAHMS, PHENIX, PHOBOS and STAR experiments at RHIC [25, 30].

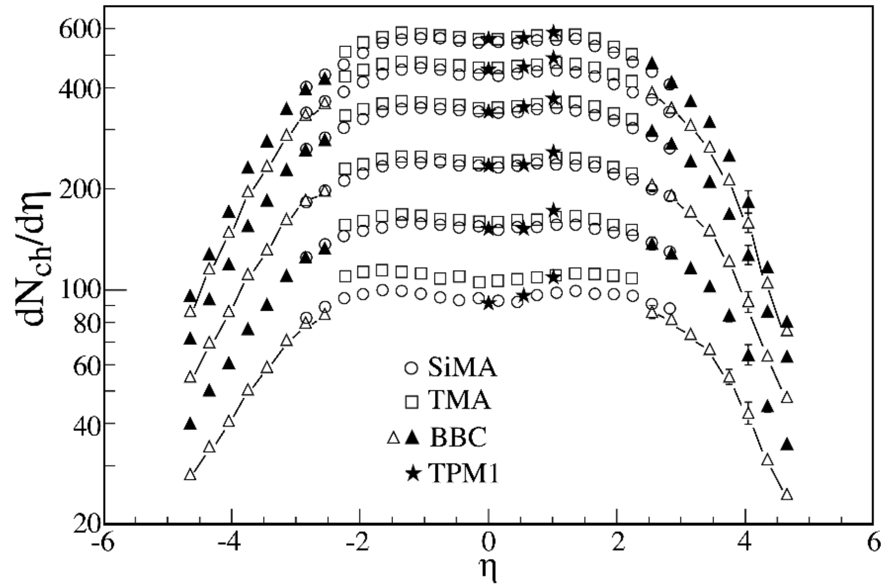

Figure 2.18: BRAHMS charged particle multiplicity distribution at $\sqrt{s_{NN}} = 130$ GeV for centrality ranges of (top to bottom) 0-5%, 5-10%, 10-20%, 20-30%, 30-40% and 40-50%. The lines are drawn to help differentiate the different centralities. It should be noted that since the scale is logarithmic it is hard to see that the top of the *plateau* for 0 to 5% central events is at a multiplicity of approximately 553 particles as listed in table 2.1 [31].

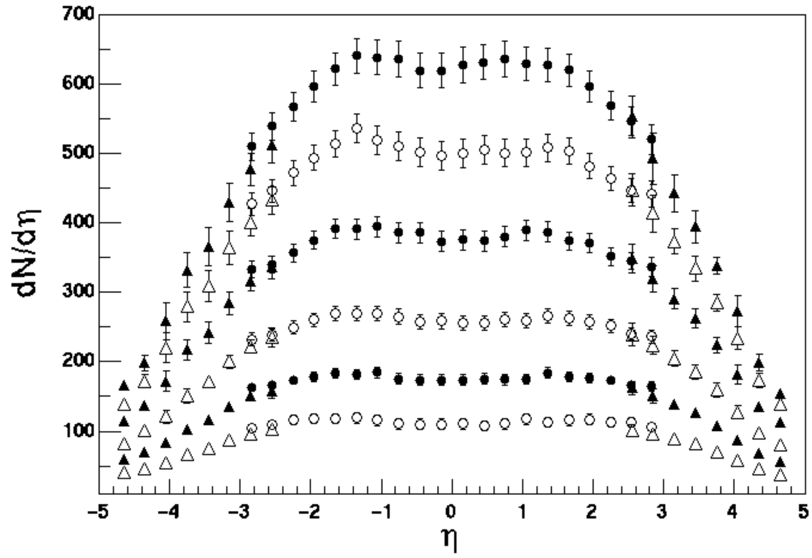

Figure 2.19: BRAHMS charged particle multiplicity distribution at $\sqrt{s_{NN}} = 200$ GeV for the same centrality ranges as shown in figure 2.18 [32].

2.7 Multiplicity Fluctuations

A phase transition from QGP to hadronic gas, has been predicted to cause large fluctuations in particle density in the collision zone [1, 37, 50, 51, 52]. Instead of a spherically symmetric stream of particles from the collision zone, fluctuations would result in more detected particles in some directions than others. This asymmetric *droplet formation* of the multiplicity distribution is what is referred to as multiplicity or density fluctuations and is believed to be observable in rapidity distributions as spikes and gaps event-by-event.

Fluctuations at a phase transition can be illustrated by considering the spatial distribution of *spin up* and *spin down* clusters, i.e. a system where there is a handedness (direction of the spins) or *Chiral asymmetry* and an interaction between the particles, shown in figure 2.20. The figure illustrates the competition between symmetry and entropy. The symmetry will try to align the spins locally to point in the same direction whereas the entropy will try to have as many spin up and downs locally to create the highest entropy. At temperatures below some critical value ($T \ll T_c$) the spatial distribution of the spins is governed by the symmetry, as shown in the top left figure 2.20.

As temperature increases, the entropy will force the ratio of *spin up* to *spin down* toward 1 but still at $T \simeq T_c$ (middle pictures) the symmetry of the system plays a role in making large clusters of spin up or down. It is only in the bottom pictures in figure 2.20 where $T \gg T_c$ that entropy completely dominates the spatial distribution. It is these large scale fluctuations shown in pictures 2 to 4 in figure 2.20 that we hope to see as Chiral symmetry is restored.

2.7.1 Event-by-Event Fluctuations

Event-by-event analysis of fluctuations in relativistic heavy ion collisions at $\sqrt{s_{NN}} = 130$ GeV may reveal interesting new physics [1, 37, 49, 84, 55]. The importance of event-by-event analysis can be illustrated by the following analogy, stated by Andrew D. Jackson, NBI:

> *Imagine holding a sheet of paper out of the window on a rainy day for a long time (many events), it would then become uniformly wet, and experimental physicists would be lead to conclude that rain is a uniform mist. Now instead by only holding the paper in the rain for a short time (event-by-event), the physicists would be able to study the striking droplet structure of rain.*

In central heavy ion collisions at $\sqrt{s_{NN}} = 130$ GeV charged particle production is about 4000 per event at RHIC and the BRAHMS experiment records about 10 to 100 events per second. It is therefore possible to do event-by-event analysis.

The expected size of fluctuation or *a droplet* is of the order of one rapidity unit [37]. Figure 2.21 illustrate this droplet formation as a function of rapidity and compares with corresponding rapidity distribution for continuous hadronic background with and without

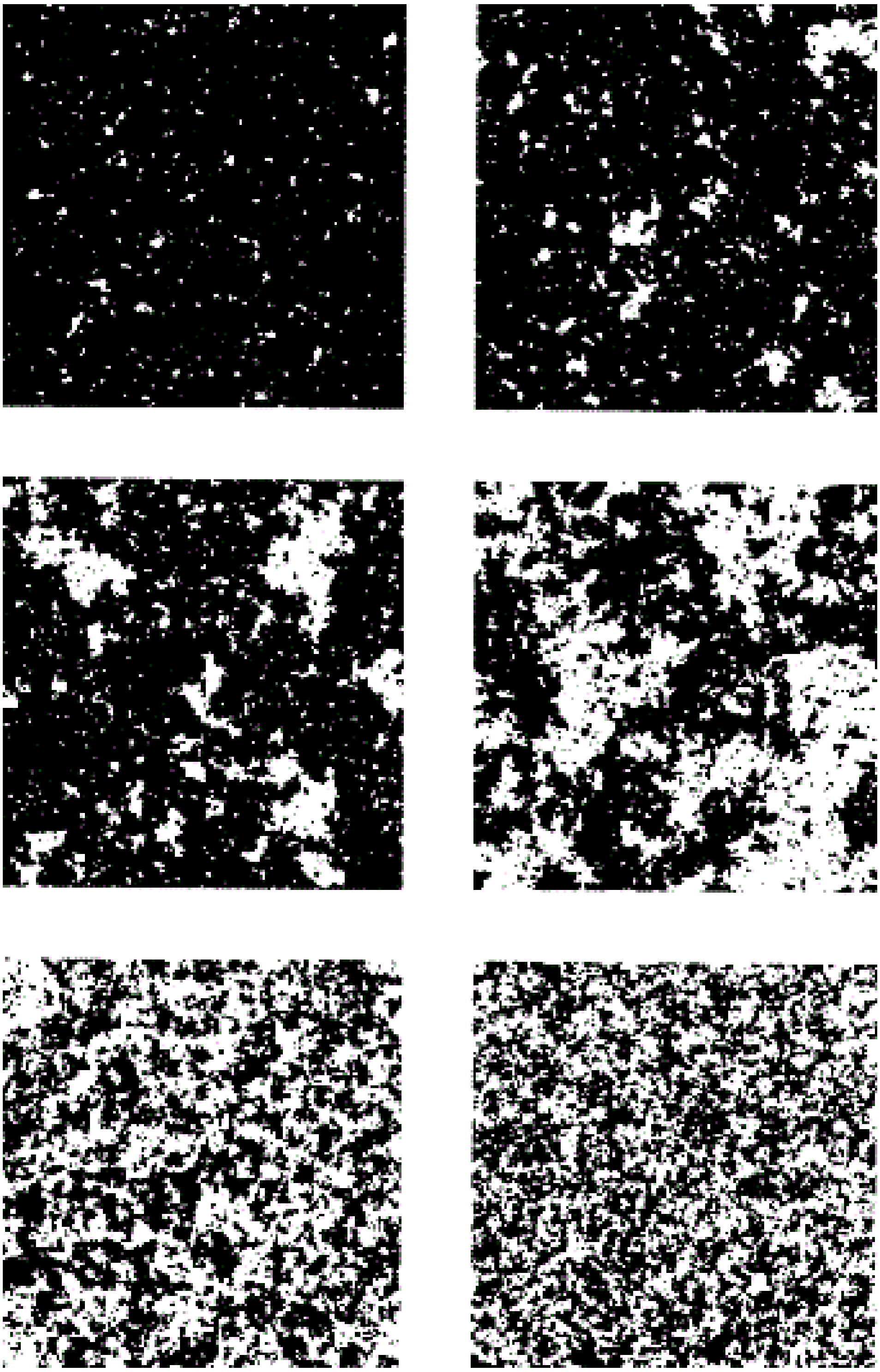

Figure 2.20: Clusters of spin-up and spin-down in the 2-dimensional Ising model. From top left to bottom right $T/T_c = 0.97$, 0.99, 1, 1.01, 1.06 and 1.15 [39].

droplets. One problem for heavy ion physics is that the typical time scale is 10^{-23} seconds and the dimension scale is 10^{-15} m. The time scale for droplet formation is unknown, but smaller than 10^{-23} second [43].

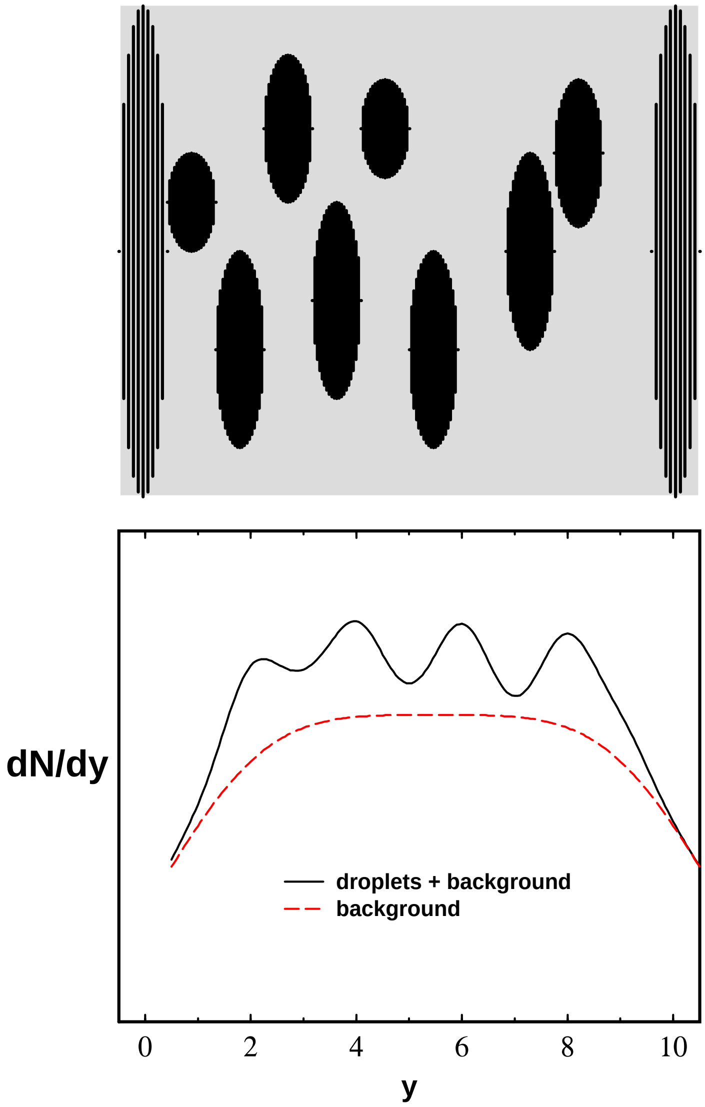

Figure 2.21: The top of the figure show the droplet formation as a function of y. The lower part show the corresponding rapidity distributions for continuous hadronic background with and without droplets [49].

The fluctuation in the number of events (N) is defined as

$$\omega_N \equiv \frac{\overline{N^2} - \overline{N}^2}{\overline{N}} \tag{2.2}$$

If droplets are formed, the measured fluctuation (equation 2.2) would exceed the statistical value of 1. This is illustrated in figure 2.22. The fluctuation of a given distribution is defined as the variance divided by the average. The two distributions has a significantly different width, but with a somewhat similar average. The predicted distribution of droplets can be approximated by an exponential function and thus causing large fluctuations. On the contrary a Poissonian distribution will result in fluctuation of 1.

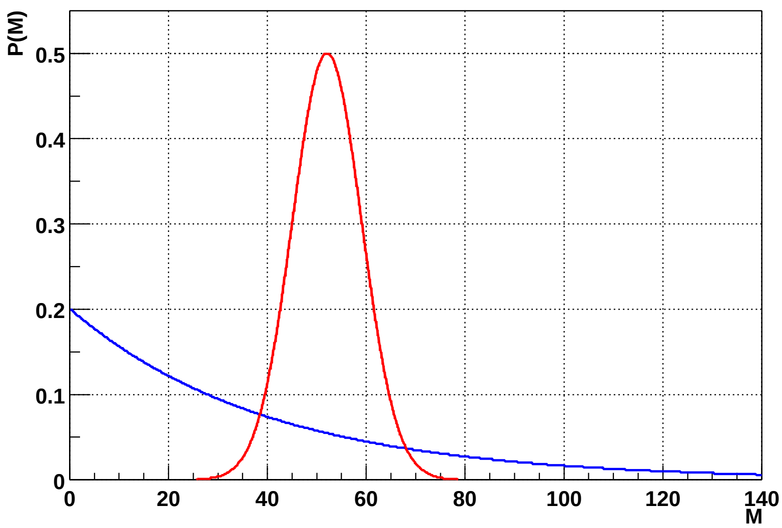

Figure 2.22: Distribution of droplet masses. A Poissonian distribution (red curve) will result in a fluctuation of 1, where as a predicted exponential droplet distribution (blue curve) will result in large fluctuations [48, 37].

The multiplicity fluctuations between any two multiplicity bins, N_i and N_j measured in a given event, can in general be defined [49, 78]

$$\omega_{N_{ij}} \equiv \frac{\overline{N_i N_j} - \overline{N_i}\ \overline{N_j}}{\sqrt{\overline{N_i}\ \overline{N_j}}} \tag{2.3}$$

where the averages are taken over the ensemble of events. The numerator is recognized as the covariance. By observing the multiplicity N in a single element, equation 2.3 simplifies to equation 2.2.

In the fluctuation analysis in chapter 6 the expected value of the measured fluctuations will be discussed. Fluctuations in multiplicity and mean transverse momentum are presently also being studied by the STAR collaboration [35]. At the CERN SPS accelerator fluctuations have also been analyzed, and in the following section I will review some results of this analysis.

2.7.2 Event-by-Event Fluctuations at SPS

At CERN SPS fluctuations in p_t, E_t, particle ratios and multiplicity have been studied in Pb+Pb collisions at 158·A GeV per nucleon [54, 55, 56]. The NA49 collaboration were the first to study event-by-event fluctuations at SPS and since then has fluctuations been studied by several experiments, for example the WA98 collaboration. In section 7.5 we shall return to the NA49 collaboration. Fluctuations as RHIC has only been studied at STAR [35] (and now BRAHMS).

The WA98 collaboration [55] has measured multiplicity fluctuations with the same definition as in equation 2.2. Assuming the *participant model*, described in section 7.5, the measured fluctuation in number of charged particles (ω_N) can be described, as in equation 7.3, by the sum of two contributions

$$\omega_N = \omega_n + \overline{n} \cdot \omega_{N_{part}} \tag{2.4}$$

where ω_n is the contribution from the number of particles produced per participant, $\overline{n}$ is the average number of particles produced per participant and $\omega_{N_{part}}$ is the fluctuation in the number of participants.

Figure 2.23 shows the SPS estimate of $\omega_{N_{part}}$ as a function of exclusive centrality cuts. The other plots in figure 2.23 show the average number of particles (top), σ of the number of participants and the associated χ^2/ndf values and finally, as mentioned, the fluctuation. All plotted as a function of exclusive centrality bins.

The experimental result of the WA98 Collaboration multiplicity fluctuation analysis is shown in figure 2.24. Because of the geometrical acceptance, the measured fluctuations are not directly comparable. Later in the thesis the fluctuations will be analyzed in a different way, since the fluctuation will be plotted as a function of average multiplicity and not number of participants.

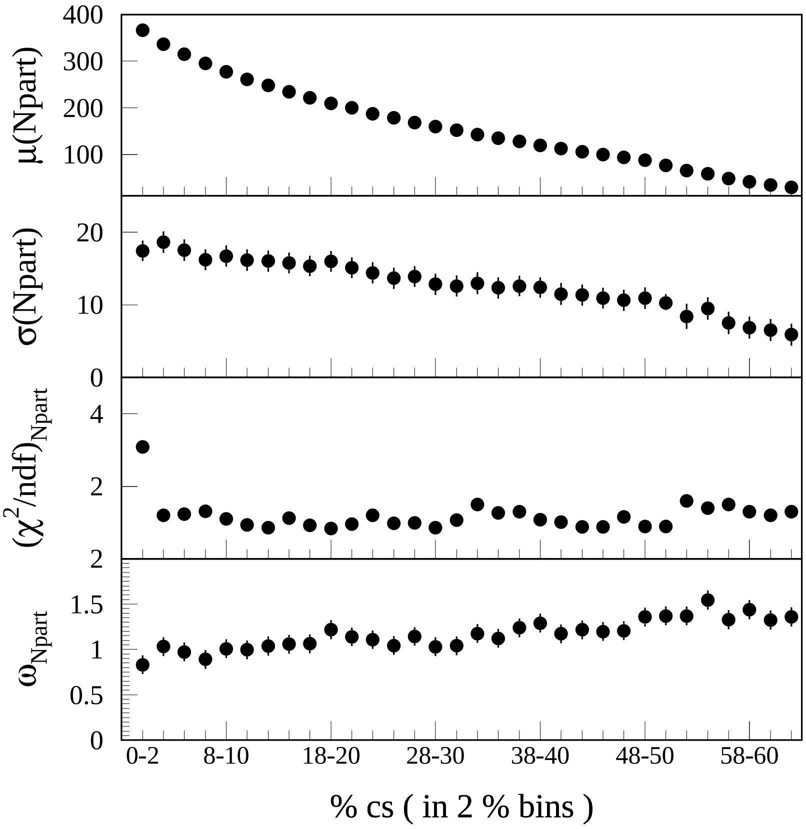

Figure 2.23: Variation of μ, σ, χ^2/ndf and ω_{Npart} of the distribution of participants vs. centrality [55].

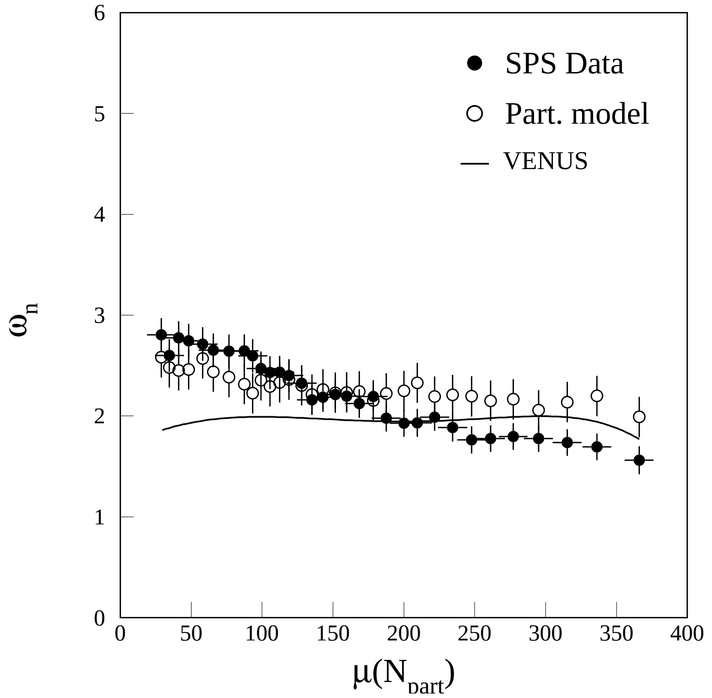

Figure 2.24: Relative fluctuations in charged particle multiplicity as a function of number of participants. The SPS data are compared with the participant and VENUS model [55].

Chapter 3

The BRAHMS Experiment

At Brookhaven National Laboratory (BNL) the first relativistic heavy ion collider (RHIC) has been constructed. RHIC has been designed to collide gold nuclei at $\sqrt{s_{NN}} = 200$ GeV, which is the highest energies seen so far in the laboratory. The machine is currently (November 2001) operating at this energy for the first time. The motivation for building RHIC is the search for and studies of the quark-gluon plasma. Presently there are four experiments at RHIC, namely STAR, PHENIX, PHOBOS and BRAHMS experiment. Before going further with describing the BRAHMS detector setup, a description of RHIC is given.

3.1 The Relativistic Heavy Ion Collider

In 1979 at BNL began a project called ISABELLE or Colliding Beam Accelerator, CBA. Due to the lack of funding, the project was stopped in 1983, even though most of the facilities had been built. On the remains of CBA, the construction of RHIC began in 1991. In July 2000 the first collisions took place.

The heavy ions are accelerated in several steps before they enter RHIC as illustrated in figure 3.1. The Tandem Van de Graff is the launch pad for the heavy gold ions. The negative ions leave the source in bunches of $4.5{\cdot}10^9$ ions. The Tandem Van de Graff accelerates the ions, using their charge of -1, from ground to $+1.5{\cdot}10^7$ V potential. The ions then passes through a stripping foil, which removes approximately 6 electrons. The now positive charged ions are then accelerated towards another stripping foil. In the distribution of charges, the ions with charge +14 are selected by a magnetic field. Exiting from the Tandem Van de Graff, the ions are further stripped and the charge is +32.

The ions are then transfered to the Booster by the Heavy Ion Transfer Line, HITL. The booster accelerates the beam, and hereby increasing the beam energy from about 1 MeV to 95 MeV per nucleon. In the transfer line from the Booster to the Alternating Gradient Synchrotron, AGS, the ions are stripped again so the charge is +77. It takes four such Tandem-Booster cycles to fill up the AGS.

In the AGS the 16 bunches are merged into 4, so that one bunch contains all particles

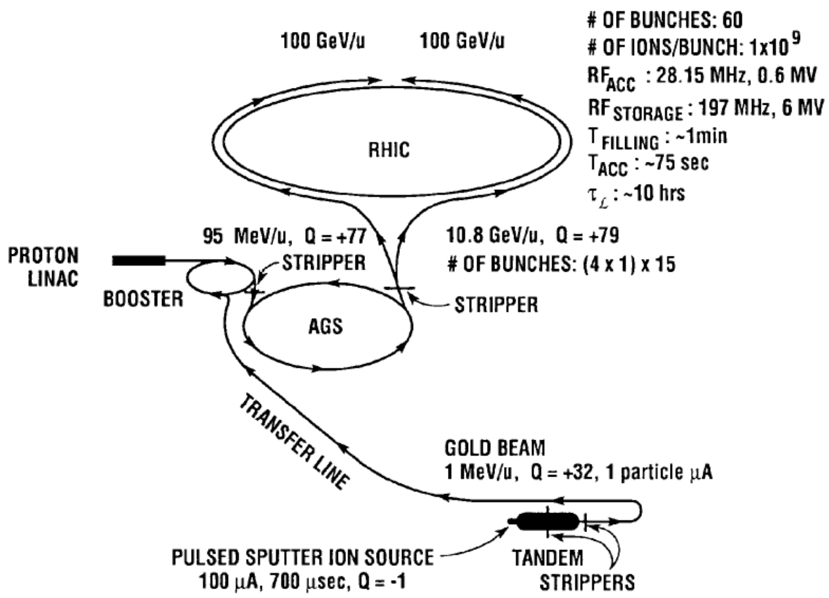

Figure 3.1: Schematic RHIC overview.

from a single Booster acceleration. The ions are accelerated up to energies of 10.8 GeV per nucleon.

From the AGS the ions are moved to the AGS-to-RHIC transfer line, ATR. A final stripping takes place here, resulting in ions with no electrons, i.e. a charge of +79. At the end of the ATR, the beam is split into two rings. One half is sent clockwise (blue ring) and the other half counterclockwise (yellow ring). The AGS allows the four bunches to be let in the two collider rings, and so the cycle is repeated until there are 60 bunches in each ring. The spacing between each bunch is 213 ns and the circumference of each of the RHIC rings is 3.8 km. The maximum energy for Au beams is 100 GeV per nucleon, resulting in $\sqrt{s_{NN}} = 200$ GeV.

The super conducting magnets in RHIC are cooled by helium to temperatures less than 4.6 K. Inside the beam pipe the pressure is less than 10^{-11} mbar. The vacuum is necessary in order to avoid beam loss from beam-gas collisions. The two beams intersect at 6 points, and the experiments are set up at 4 of these locations. On each side of an intersection region, magnets (DX) has been placed, in order to steer the beams so that the beams intersect at 0 degree angle. RHIC is also capable of running with other beam species, such as polarized protons, Be, Si, etc. [36, 53, 9]

3.2 Experimental Setup of BRAHMS

BRAHMS is designed to measure charged hadrons over a wide range of rapidity and transverse momentum for all available ion beams and energies at RHIC [57, 58].

The BRAHMS experimental setup consist of a global detector system and three separate

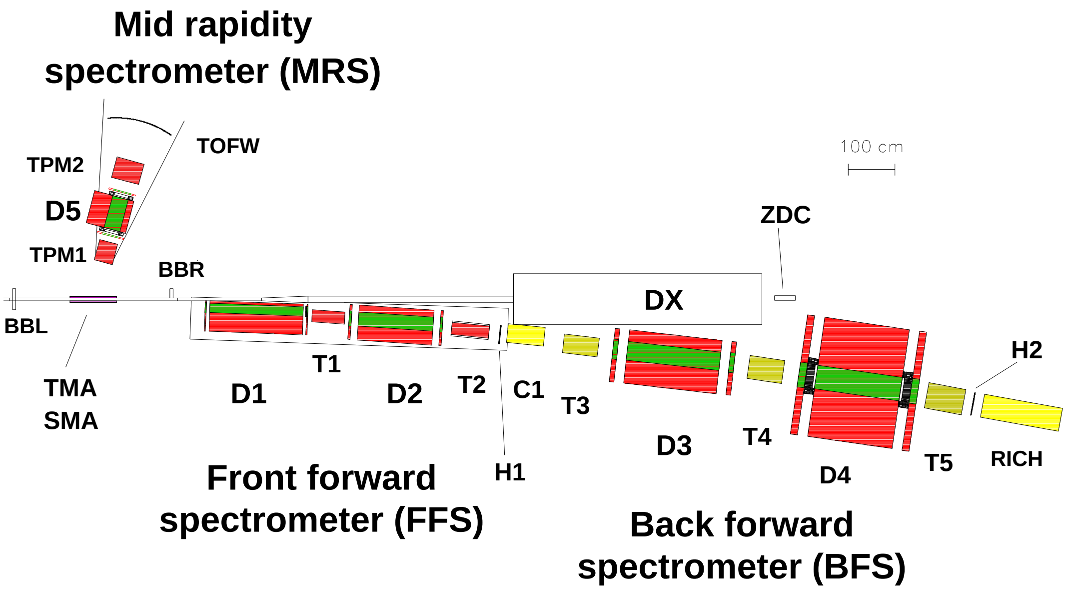

Figure 3.2: BRAHMS detector overview.

mobile magnetic spectrometers, as shown on figure 3.2. The global detectors are the beam-beam counters (BB), zero degree calorimeters (ZDC's), the scintillator tile multiplicity array (TMA) and the silicon multiplicity array (SiMA). The midrapidity spectrometer (MRS) covers angles from 30° to 95°. The forward spectrometer is divided into a front forward spectrometer (FFS) and a back forward spectrometer (BFS) covering angles from 2.3° to 30° and 2.3° to 15° respectively.

The MRS has a dipole magnet (D5) with one time projection chamber in front of and one behind it (TPM1 and TPM2). This setup makes it possible measure the bending angle of a charged particle in the magnet. Behind TPM2 is a time-of-flight wall (TOFW), which together with a start time from BB makes it possible to measure the flight time. From the bending angle the momentum can be extracted and with the flight time, the particle can be identified.

The FFS has a dipole magnet at the front (D1) used to bend particles away from DX magnet and into the spectrometer. After the magnet, another dipole magnet (D2) is placed, with time projection chambers in front and behind it (T1 and T2). After T2 a time-of-flight hodoscope (H1) is placed. This setup is in principle the same as the MRS, i. e. it makes it possible to identify particles. The Čerenkov tank (C1) located behind H1 extend the particle identification for high momentum particles.

The BFS has two large dipole magnets (D3 and D4). On each side of these, drift chambers are located (T3, T4 and T5). A time-of-flight wall (H2) is located behind T5. At the end of the arm, the RICH counter is mounted. The DX in figure 3.2 refers to the beam steering magnet mentioned in the previous section.

In the following sections, 3.2.1 to 3.2.9, the basic structure of the detector components will be described.

3.2.1 The Tile Multiplicity Array

The TMA is the detector used in the thesis analysis and is therefore described somewhat more thorough than the other detectors in the BRAHMS experiment. Before describing the array, principles of a scintillation detector, i.e. scintillator material and photo multiplier tubes are explained.

When a charged particle moving with relativistic energy passes through the plastic scintillating matter it will loose energy by primary ionization. The energy loss $-\frac{dE}{dx}$ is dominated due to Coulomb scattering from the atomic electrons. In the 1930s Bethe, Bloch and others managed to describe the energy loss as

$$-\frac{dE}{dx} = Kz^2\frac{Z}{A}\frac{1}{\beta^2}\left[\frac{1}{2}ln\frac{2m_ec^2\beta^2\gamma^2T_{max}}{I^2} - \beta^2 - \frac{\delta}{2}\right] \tag{3.1}$$

where x is the distance traveled in the medium, dx is measured in mass per unit area, K is $4\pi N_A r_e^2 m_e c^2$, z is the charge, Z is the atomic number of medium, A is the atomic mass of medium, T_{max} is the kinetic energy, N_A is Avogadro's number, r_e is the electron radius, m_e is the electron mass, I is the mean excitation energy and δ is the density effect correction to ionization energy loss. In figure 3.3 this energy loss is shown in different media [59].

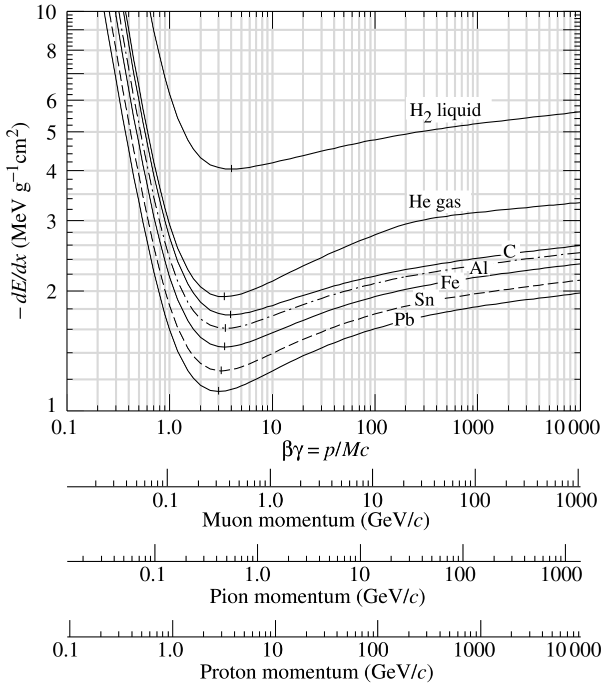

Figure 3.3: Energy loss rate in different media for μ, π and protons [59].

From figure 3.3 one can observe that $-\frac{dE}{dx}$ drops off rapidly as the velocity increases from zero. This is due to the $\frac{1}{\beta^2}$ factor in equation 3.1. There is a region of *minimum* *ionization* for all particles at $\beta\gamma \simeq 3$. After the minimum, β approaches 1 and the curve rises logarithmically. The rise is slowed down by the δ factor.

Figure 3.4 shows experimental minimum ionizing particle curves for muons, pions, kaons, protons and deuterons. Note that there is no characteristic minimum for electrons on the figure, which is because of the much smaller electron mass [5] [59].

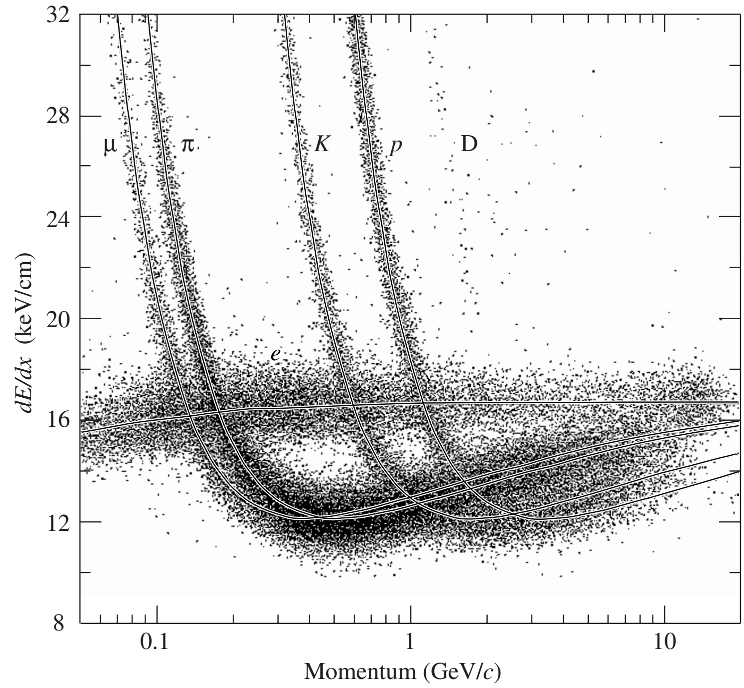

Figure 3.4: Experimental MIP curves for electrons, muons, pions, kaons, protons and deuterons. Medium used is a mixture of Argon and CH_4 (80-20%) at 5.5 atm [59].

The efficiency for a scintillator is determined by the ability to convert excitation energy into photons. In plastic the average energy loss required to create a photon is of the order 100 eV [67]. Some of the emitted photons either directly, or after some internal reflections, reach a photo cathode of the photo multiplier (PM) tube.

When the emitted photon reaches the photo cathode, an electron will be released, because of the photo electric effect. This electron will then be sent through a photo multiplier optic system, where it will be accelerated and focused, and a dynode will be hit. A dynode is a secondary emission electrode, which absorbs some of the energy of the incoming electron, and hereby releases more electrons. From the dynode the electrons move through the PM tube to a new dynode, which amplifies the signal. The number of dynodes and the high voltage applied on the tube determines the created number of electrons, i.e. the amplification. This is illustrated in figure 3.5. The signal from the PM tube is then, via a discriminator sent to an TDC (Time to Digital Converter) and to an ADC (Analogue to Digital Converter). The output is a well defined pulse, which is proportional to the energy of the incoming photon.

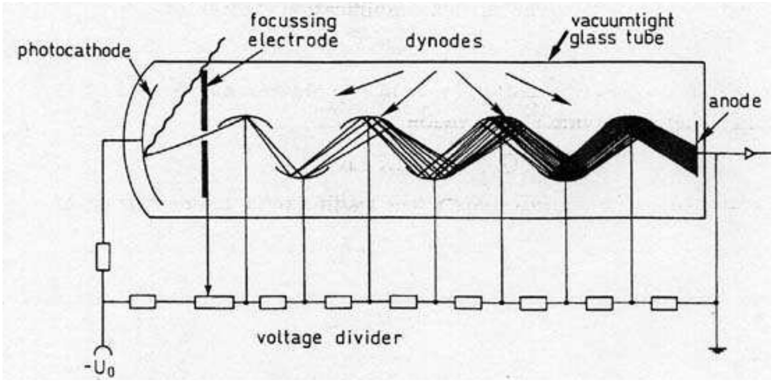

Figure 3.5: Photo multiplier tube. The initial photon is converted into a weak current of photo electrons. The photo multiplier system then amplifies this current [67].

In BRAHMS the tile multiplicity array consists of 38 plastic scintillating tiles. The tiles are arranged in an hexagonal aluminum frame next to the silicon detectors, as shown in figure 3.6. Each tile is wrapped with with bond paper and black Tedlar PVF tape [58] in order to prevent natural light from activating the tile. From the tile there is an optical fiber leading the light to the 3.8 cm diameter Hamamatsu PM tube.

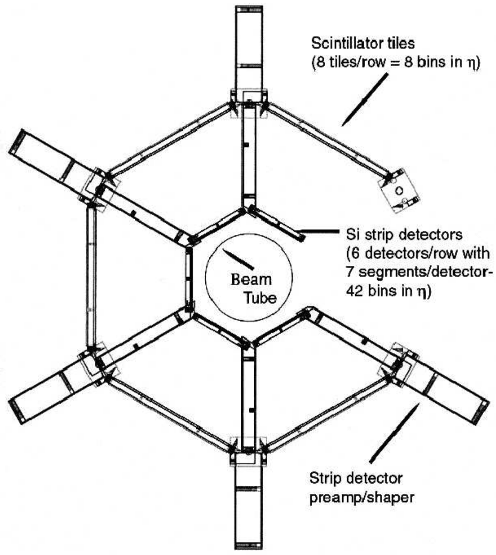

Figure 3.6: Multiplicity array viewed from the beam pipe. The inner hexagon close to the beam are occupied by silicon strip detectors. The outer hexagon are filled with tile scintillator detectors.

On each side of the hexagon there is a row with space reserved for 8 tiles. In order to prevent scattering in the regions of the forward or mid spectrometer, 6 tiles toward the mid spectrometer and 4 toward the forward were removed. The conventional numbering of the tiles are shown in figure3.7

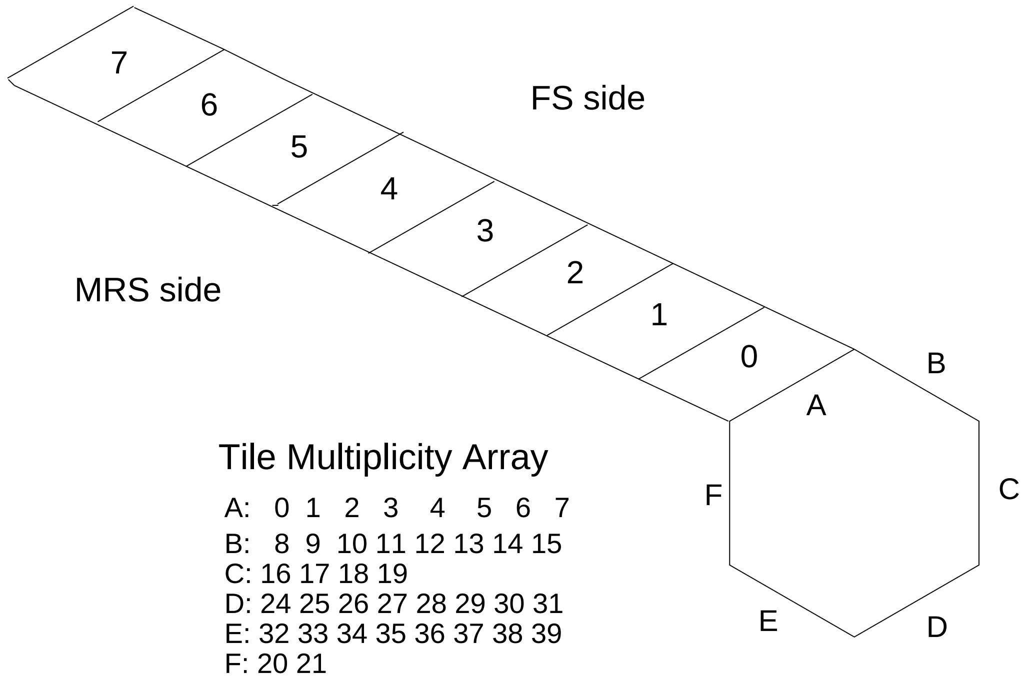

Figure 3.7: Conventional numbering in the multiplicity tile array. Row A is also referred to as row 0007 in the analysis, i.e. tiles 0 to 7. In the same way is row 0815 defined for row B (tiles 8 to 15), row 2431 (tiles 24 to 31) for row D and row 3239 (tiles 32 to 39) for row E. The azimuthal angle (ϕ) is defined to be zero at row F (mid spectrometer side). Positive orbital direction is defined clockwise when facing positive z-direction.

The dimensions of each tile is $12 \times 12 \times 0.5$ cm^3. The tiles are equally spaced with 0.46 cm, except at nominal vertex (Z = 0) where the space is 0.765 cm. The total length of the array is 99.53 cm and the distance from the center of the beam pipe is 13.86 cm [57], which corresponds to $\eta = \pm 1.99$ at the edge for the particles created at Z=0. Table 3.1 list the z and η coverage of each ring with respect to the nominal interaction point.

	Z-coordinates [cm]	η coverage	Center η
Ring 0	[-49.76;-37.76]	[-1.99;-1.73]	-1.87
Ring 1	[-37.30;-25.30]	[-1.72;-1.36]	-1.55
Ring 2	[-24.84;-12.84]	[-1.35;-0.83]	-1.11
Ring 3	[-12.38;-0.38]	[-0.80;-0.03]	-0.47
Ring 4	[0.38;12.38]	[0.03;0.80]	0.47
Ring 5	[12.84;24.84]	[0.83;1.35]	1.11
Ring 6	[25.30;37.30]	[1.36;1.72]	1.55
Ring 7	[37.76;49.76]	[1.73;1.99]	1.87

Table 3.1: Acceptance for the tile rings. Center η is the pseudorapidity calculated from the nominal interaction point to the center of each tile ring.

In this thesis the TMA is used to measure the charged particle multiplicity on an event-by-event basis. In principle, the multiplicity is derived by assuming that all particles are minimum ionizing particles. The multiplicity can therefore be calculated, by dividing the total energy deposit by the energy on one minimum ionizing particle. The energy corresponding to one MIP is calibrated with cosmic muons which enters the tile at 90°. When the particles created in a collision reaches the detector it is not necessarily at 90°, and so an angle correction is applied. Slower particles will deposit more energy than a minimum ionizing particle which is also be corrected for. This will be discussed in section 5.4.

In the following section the other half of the multiplicity array (MA) will be described, namely the silicon multiplicity array (SiMA).

3.2.2 The Silicon Multiplicity Array

A silicon detector is analogous to a gas ionization detector, but instead of using gas, it uses a solid semi conducting material. Instead of creating electron-ion pairs, it creates electron-hole pairs. The charge is then collected by an electric field. The energy resolution of a silicon detector is an order of magnitude better than that of a gas ionization detector because of the energy required to create a hole is about 10 times smaller.

The efficiency of a silicon detector is the percentage of the incoming charged particles, which in the end results in a electric pulse, i.e. a measurement. For a silicon detector the efficiency depends on how many electron hole pairs that were created, and thereby the absorption, which is proportional to Z^4 [57, 67].

The silicon multiplicity array (SiMA) is located only 5.3 cm from the center of the beam pipe. It is as the tile array arranged in a hexagon, as seen in figure 3.6. There are 25 silicon detectors each with dimensions $4.0cm \times 0.85cm \times 300\mu m$. Each silicon row has space for 6 detectors. Each detector has 7 strips. In order to accommodate a clear line-of-sight for the two spectrometer arms, only three rows were populated with 6 wafers. One row have five wafers and the last two rows has only one wafer each. A row with 6 wafers gives a resolution in η of 42 bins. The length of the silicon array is 43.16 cm and the distance from the center of the beam pipe is 5.3 cm. This corresponds to a range of -2.2 $\leq \eta \leq$ 2.2 seen from the nominal interaction point. Some silicon detectors are not placed in order not to interfere with the two spectrometer arms.

3.2.3 The Beam-Beam Counters

The primary objective for the beam-beam counters is to provide a vertex position, start time and a first level trigger. They are also able to give a charged particle multiplicity distribution for high η [63].

BRAHMS has two beam-beam Čerenkov counter arrays. Each detector consists of Čerenkov radiators, glued on to photo multiplier tubes. The arrays are located 2.20 m from nominal intersection point. The diameter of the photo tubes are 19 mm or 51 mm with 4 cm long or 3 cm long radiators respectively for *large* and *small* tubes. The detectors are positioned in the array, so that they cover pseudorapidities 3.1, 3.4 and 3.6 relative to nominal collision vertex. The right array has reduced azimuthal coverage because of the magnet D1, as seen in figure 3.8. There is partially compensated for this by a higher density of modules in the array.

The intrinsic time resolution is 65 ps giving an interaction vertex with precision of $\simeq$2.0 cm [31]. The coverage in pseudorapidity for the detector is $3.0 < \eta < 3.8$ [57] relative to the nominal interaction point.

3.2.4 The Zero Degree Calorimeters

The purpose of the zero degree calorimeter is to detect the energy deposit by neutrons, emitted in a cone ($|\theta| <$ 2 mrad) along beam axis. The detected neutrons are spectator neutrons and the number is therefore closely related to the impact parameter. By detecting the neutrons the ZDC's are also able to determine interaction vertex position.

The two ZDC's are positioned symmetrically behind the DX magnets at a distance of 18 m from nominal interaction point. Each ZDC consist of alternating layers of fiber-ribbon plastic scintillator and tungsten. Čerenkov radiating material is attached to photo multiplier tubes. Each module has 29 layers of tungsten plates with dimensions $187.5 \times 100 \times 5$ mm^3. The plates are tilted 45° with respect to the beam axis.

By coincidence with the ZDC's on both side of nominal vertex, it is possible to get a minimum bias selection. Thus the detector is also used as an event trigger, as described in section 3.4. By using the time difference of the two ZDC signals, the collision vertex can be determined with an accuracy of $\approx$ 3.5 cm [64, 65, 66].

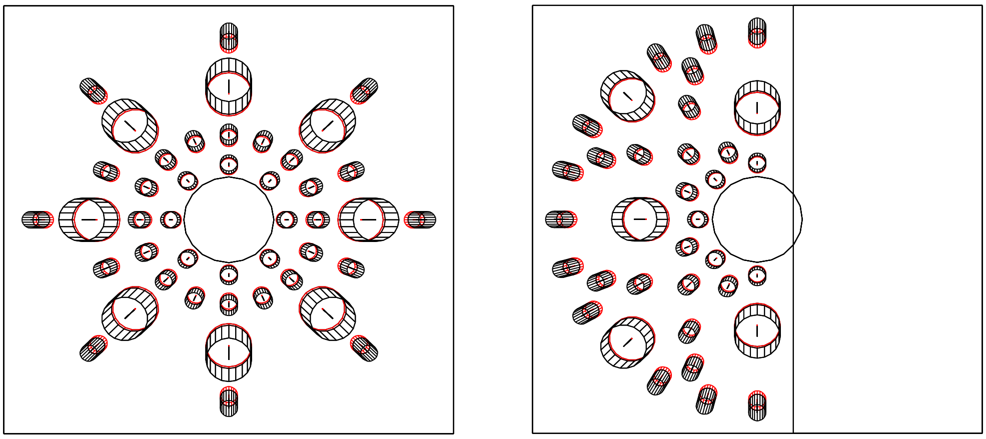

Figure 3.8: The two beam-beam counter arrays. The left figure show the left array and *visa versa*. The asymmetric distribution in the right array is due to the line of sight of the forward spectrometer.

3.2.5 The Magnets

The five dipole magnets (D1 to D5) in BRAHMS are made of iron with copper conducting coils and epoxy/glass insulation. They are used to bend the path of charged particles in order to determine the ratio p/q. The momentum resolution is dependent on $B \cdot dl$ integrated over the length (l) of the dipole, where B is the magnet field. More information on the magnets can be found in table 3.2.

	Length [cm]	**Width** [cm]	**Max Field**[T]	$B \cdot dl$ [Tm]	**Current** [A]
D1	225	49	1.26	2.6	3450
D2	200	98	1.68	2.8	3000
D3	260	142	1.22	2.58	3000
D4	244	239	1.19	2.34	2750
D5	99	101.6	1.45	1.21	2500

Table 3.2: Magnet dimensions and field specifications [58].

3.2.6 The Time Projection Chambers

The time projection chamber is a three dimensional ionization detector. It provides information on particle position and energy loss (dE/dx) at several points on the particles path through the detector. The detector is therefore also often referred to a three dimensional electronic bubble chamber. It was proposed by D. R. Nygren in 1978 [67] and was based on concepts from the multi-wire proportional chambers and drift chambers.

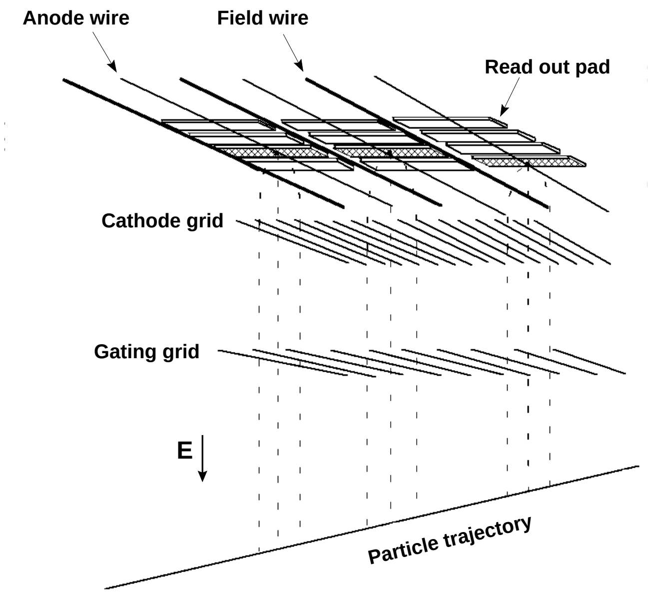

Figure 3.9: The basic principles of the pad-readout TPC.

When a charged particle enters the drift region of the TPC, it will ionize the gas along the track. Due to a homogeneous $\vec{E}$ field, indicated in figure 3.9, the liberated electrons ($\backsim$90 electrons/cm) will drift towards the top at constant velocity. The gating grid is a wire plane which is open at no applied voltage. Here the TPC receives the trigger signal from the trigger system. After the electrons have passed the cathode plane they are accelerated towards the anode wires and the field gradient is here so high, that an avalanche of electrons are created, as seen in figure 3.10. The charge of the avalanche is proportional to the number of electrons, that were liberated by the particle transversing the detector. The z-coordinate of the primary ionization can be extracted from the anode wires (row number) and the x-coordinate from the pads. The y-coordinate is obtained by measuring the time difference between the primary ionization and the time where the charge was deposited on the anode wire, i.e. the *drift time*. This is possible because of the low drifting velocity, compared to the velocity of the particles that traverses the TPC.

The gas used in the TPC's is a mixture or Ar and CO_2 (90% - 10%) provides a slow drift velocity ($\sim$ 1.6 cm/nsec) and low longitudinal and transverse diffusion constants. Detector dimensions and pad/row configuration for the TPC's can be found below in table 3.3.

3.2.7 The Drift Chambers

The drift chambers are, like the time projection chambers, tracking devices. The main reason for implementing drift chambers instead of TPC's are financial. Drift chambers are

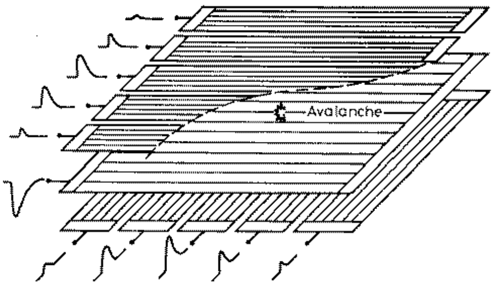

Figure 3.10: TPC avalanche [67].

	Width	**Height**	**Length**	**Padrows**	**Pad/row**	**Dist to vertex**
T1	33.60	19.80	56.00	14	96	500
T2	39.60	19.80	75.50	16	112	810
TPM1	38.40	20.00	36.60	12	96	95
TPM2	67.68	19.80	50.00	20	144	285

Table 3.3: TPC inner dimensions [cm], number of rows, pad/row configuration and distance to vertex. All lengths in cm [57, 58].

only efficient for low track densities and are therefore placed in the BFS where a lower track density is expected.

When a particle travels through the detector, electrons are liberated in the gas. The electrons then drift towards a the anode wire (sense wire). Near the anode an avalanche of electron/ion pairs is created in the same way as in the TPC and shown in figure 3.10.

The track reconstruction shown in figure 3.11 is based on matching hits on the different planes in the drift chamber. The position of a track can be determined with a precision of $\sigma \simeq 100\ \mu$m [61].

In BRAHMS there are three drift chambers, denoted T3, T4 and T5 on figure 3.2. They are positioned before and after the magnet D3 and after D4. The drift chamber covers a relatively large surface area with its wires. The gas used in the drift chambers is a mixture of 68% Ar, 29.2% C_4H_{10} (Isobutane) and 2.8% alcohol.

3.2.8 The Time-of-Flight Hodoscopes

The three hodoscopes in BRAHMS provide time-of-flight measurements - from the time of the collision to a charged particle moves through the detector.

A hodoscope consists of a set of scintillating staves on which two PM tubes are connected at either end. A particle passing through the scintillating material, excites electrons and thereby creates light which is transported through the transparent scintillating material and measured by the photo multipliers.

The flight time is obtained by subtracting the readout time with the start time. Know-

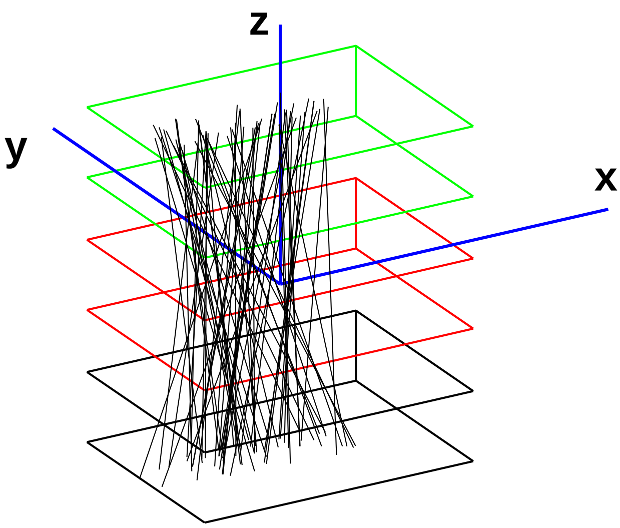

Figure 3.11: Reconstructed tracks in T3 [62].

ing the flight time and the momentum, the particle can be identified by

$$m^2 = p^2(\frac{1}{\beta^2} - 1) \tag{3.2}$$

The hodoscopes in BRAHMS are named H1, H2 and TOFW. H1 and H2 in the forward spectrometer are responsible of the low momentum particle identification. H1 provides a 4σ π/K separation up to 3.3 GeV and K/p separation up to 5.7 GeV. For H2 the 4σ π/K is up to 5.8 GeV and for a K/p up to 8.5 GeV. The TOFW at the back of midrapidity spectrometer will when fully instrumented cover 160 cm. It is capable of a 4σ separation of particles up to 2.5 GeV for π/K and 4.3 GeV for K/p. The time resolution for the hodoscopes achieved during the first year run was 100 ps. More information on the hodoscopes can be found below in table 3.4.

	Width	**Height**	**Depth**	**No. slats**	**Dist. to vertex**
H1	1.0	20	1.0	40	8.60
H2	1.0	40	1.5	32	18.90
TOFW	1.25	22	1.27	83	4.30

Table 3.4: Dimensions [cm] of the slats, number of slats and distances to the vertex [58].

3.2.9 The Čerenkov Detectors

The purpose of the Čerenkov detectors (C1 and RICH) is to provide high momentum particle identification.

A particle moving in a gas with refractive index n will emit photons in cone with an angle θ_c relative to momentum given by $cos\,(\theta_c) = \frac{1}{n\beta}$ when exceeding a certain threshold velocity given by $v = \beta c = \frac{c}{n}$. Thus the name *threshold detector*, since lower momentum particles will not emit Čerenkov light. The emitted light is collected by photo multiplier tubes. The RICH detector focuses the light with a mirror system onto a detector plane, as illustrated on figure 3.12.

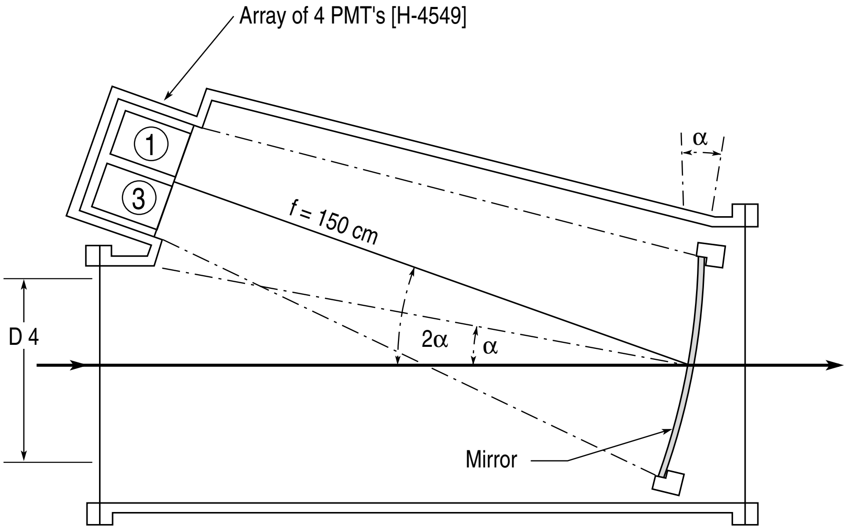

Figure 3.12: Side view of the RICH detector [10].

The radius of the ring is shown in figure 3.13 is then used to identify the particle species.

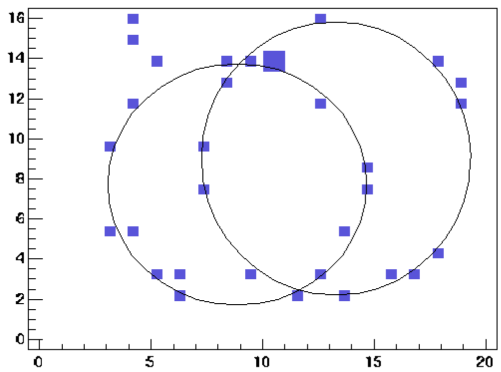

Figure 3.13: RICH detector. The radius of the emitted Čerenkov light can be converted to particle momentum [58].

The C1 Čerenkov detector is a threshold detector in the sense that the pion threshold is at 2.6 GeV/c. Discriminating between kaons and pions is possible up to the kaon threshold at 9.3 GeV/c. The thresholds are determined by the refractive index of the radiator gas used (C_4F_{10}) as mentioned above. Measurements with particles ranging from 3 to 7 GeV has shown that $n - 1 = 1380 \cdot 10^{-6}$ [58].

The RICH detector is a ring imaging Čerenkov detector. Figure 3.14 shows an event where a ring was detected in C1.

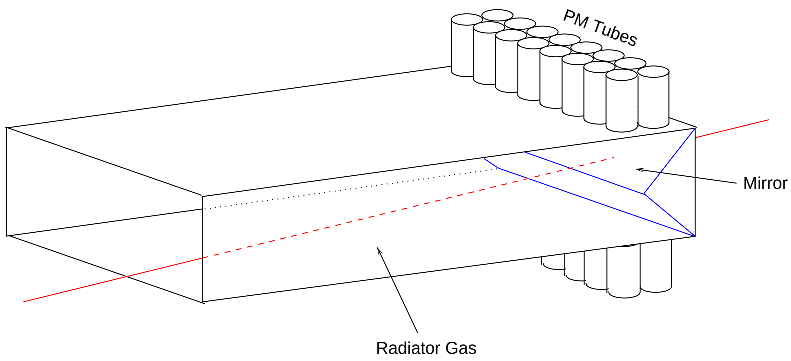

Figure 3.14: Principle of the C1 detector.

The RICH detects pions with momenta as low as 2.5 GeV/c and up to 26 GeV/c. Above this momenta they can not be separated from the kaons. Protons can be detected above 30 GeV/c [58]. The gas used is a mixture of C_4F_{10} and C_5F_{12} resulting in an index of refraction of $n - 1 = 1850 \cdot 10^{-6}$.

3.3 BRAHMS Acceptance

The large coverage in rapidity-p_t of BRAHMS is shown in figure 3.15. The top left plot shows π/K separation (4σ) in MRS. The two bottom plots show the same as above plots, but for K/p separation. In the first run period (~2 weeks) in August 2000, only a very small fraction of the acceptance was covered.

Even though BRAHMS can only measure a fraction of the particles in an event, the wide coverage of p_t and rapidity makes it possible to measure quantities such as π/K ratios, which is an indicator for the proposed strangeness enhancement if a quark-gluon plasma is created in the collision, as described in section 2.5.2. In the midrapidity spectrometer it is possible to measure Λ production. HBT measurements over a broad rapidity and p_t range can be performed utilizing the forward and the midrapidity spectrometer.

3.4 BRAHMS Triggers

A trigger is used to select a certain event class reject *pseudo events*, such as beam-gas and very peripheral collisions. The trigger selects an event, if it fulfills a certain trigger criteria. If the criteria is obtained, events will be accepted and the data acquisition (DAQ)

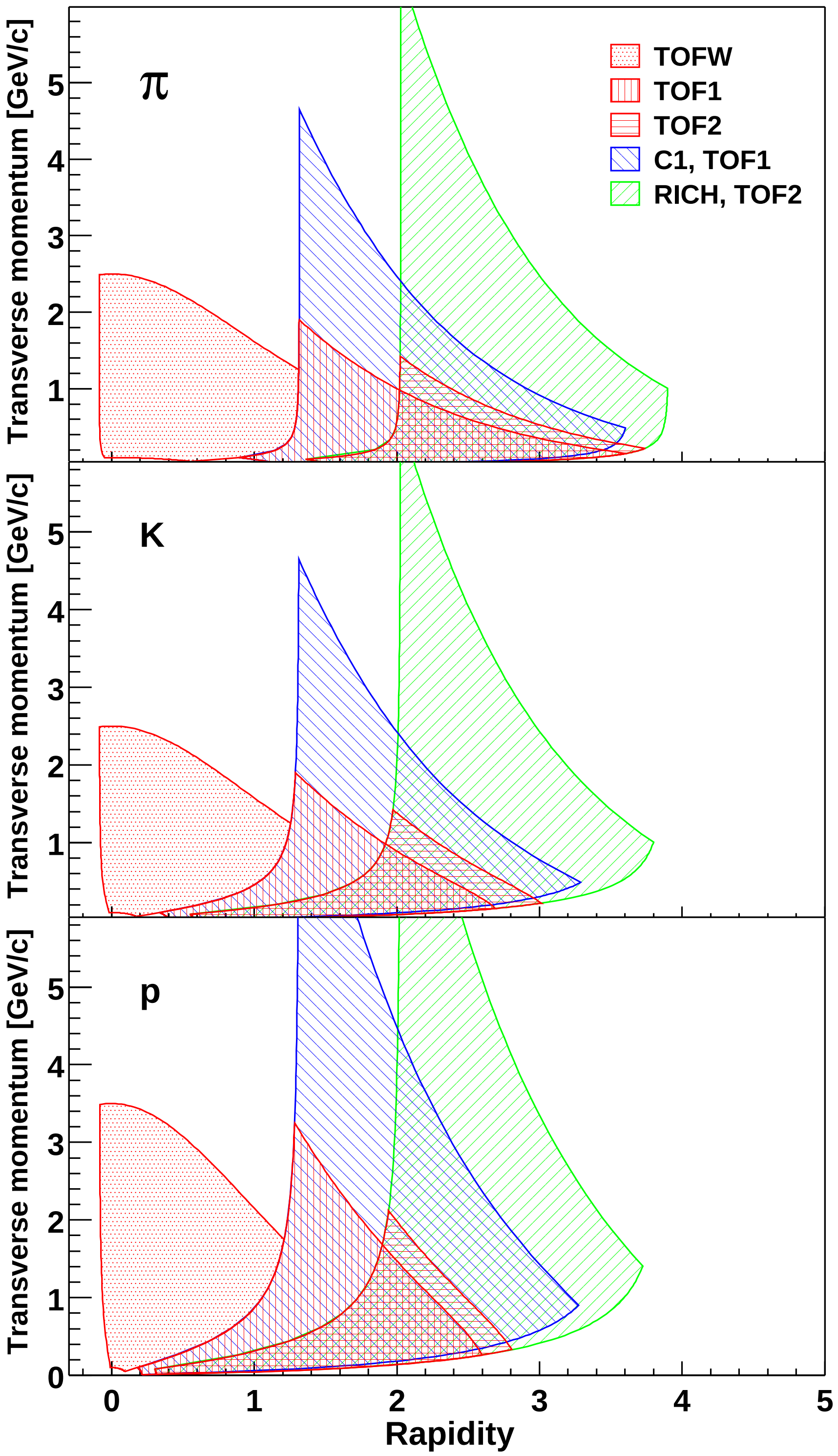

Figure 3.15: BRAHMS acceptance for π, K and p. The various coverage from TOFW, TOF1, TOF2, C1, TOF1, RICH and TOF2 are shown in different colors.

will begin. The DAQ stores the data on a permanent storage media which can be accessed later on for analysis.

An example of a such a trigger criteria could be the deposit of a certain energy, as it is with the BRAHMS ZDC trigger - denoted trigger 4. The ZDC trigger is a minimum bias trigger and requires an energy deposit in each of the two ZDC's above 25 GeV to fulfill the trigger criteria. A complete list of the BRAHMS triggers for the year 2000 runs is shown in table 3.5.

Since it takes a certain time to receive a signal, the duration of the signal becomes important. So in order to avoid this *dead time* in the DAQ, one can choose to scale down the triggers. This method is essential if the collision rate is high.

Trigger	**Description**
1	At least two big tubes in each beam-beam array firing within 5 ns time gate.
2 & 3	Triggers reserved for TPC testing.
4	Both ZDC's firing within 18 ns time gate. A single neutron is enough to make the ZDC fire.
5	Three big tubes in each beam-beam array firing within 14 ns time gate.
6	The signal from two of the central big tubes in each beam-beam array signaling within 15 ns time gate.
7	Trigger reserved for pulser tests.
8	Synchronization trigger.

Table 3.5: The BRAHMS triggers.

3.5 Vertex Determination

In BRAHMS three detectors are used to determine the collision vertex. They are the beam-beam counters, the ZDC's and TPM1. In principle the vertex determination from the beam-beam counters and the ZDC's is done in the same way.

Figure 3.16 shows the collision event geometry. From the collision zone particles flow out in all directions. The two beam-beam counter arrays (BBL and BBR) are positioned symmetrically on either side of the nominal vertex. Some particles will hit the left beam-beam counter array and some the right. This creates TDC signals in both arrays. Calibrating these signals and taking the mean of these times provides two time signals which are still dependent on the difference in cable length. In practise the software takes care of all calibrations and the difference in cable length. But since it is not known what channel the trigger signal comes from, another unknown contribution (T_{trig}) has to be added [10]. Assuming that the particles triggering the arrays are moving with the speed of light, the two times measured in each array becomes

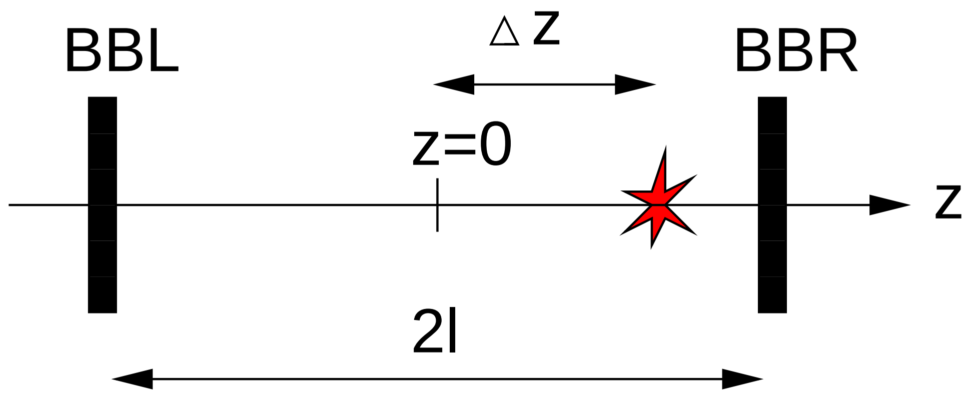

Figure 3.16: Vertex determination by the beam-beam counters. BBL and BBR denote the two arrays, also shown in figure 3.8.

$$T_L = \frac{l + \Delta z}{c} + T_{trig} \tag{3.3}$$

and

$$T_L = \frac{l - \Delta z}{c} + T_{trig} \tag{3.4}$$

where l is the distance from nominal vertex to the counters and Δz is the offset from nominal vertex to the collision vertex. By subtracting equation 3.4 from 3.3 the vertex can be derived as

$$\Delta z = c \cdot \frac{T_L - T_R}{2} \tag{3.5}$$

The width of the beam-beam vertex depends on the time resolution. With a time resolution of 70 ns, the vertex can be determined with an ≈2.1 cm accuracy [6].

The two other methods of determining the vertex were not used in this analysis, so they will not be described in details, but in principle is the ZDC vertex determined in the same way, i.e. by coincidence of two time signals. The *cluster vertex* determined by the time projecting chamber, TPM1. The vertex is determined by reconstructing all possible lines through the hits in TPM1, pointing them back to the beam line and evaluating the most probable vertex. A detailed description of this vertex determination can be found in [6], but essentially a histogram is filled for each track pointing back to the beam. The peak in this histogram is then identified as the vertex. Comparison of the different types of vertices is shown in figure 3.17.

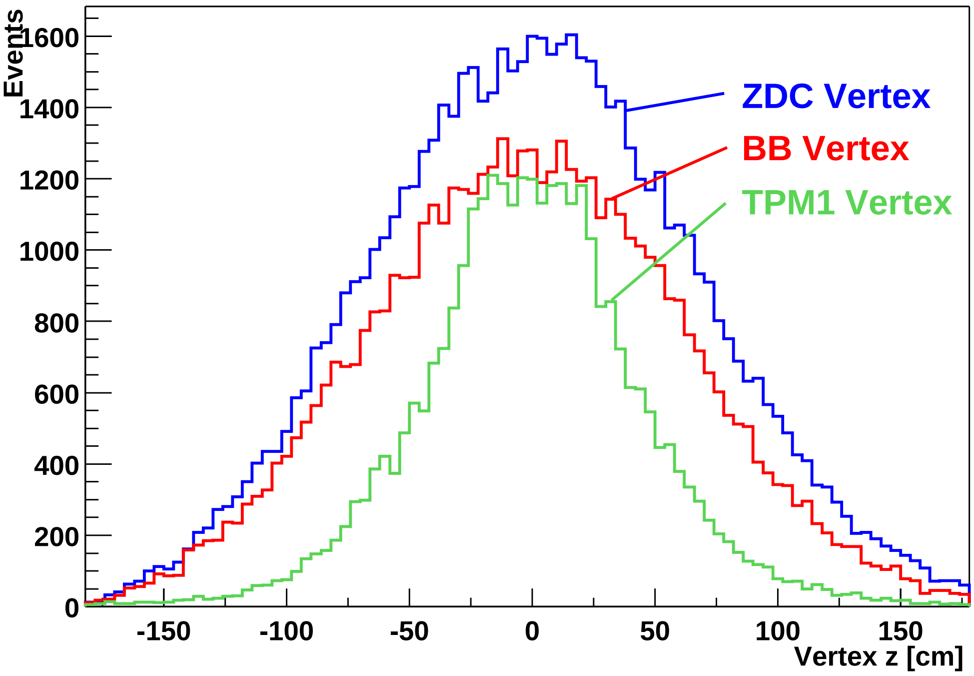

Figure 3.17: The three different vertices in BRAHMS.

Chapter 4

BRAG Simulations

GEANT [69] is the combination of a detector description and simulation tool. The first version was developed in 1974, and has been modified and extended ever since because of the growing complexity in the experiments. GEANT is used to optimize detectors, develop and test tracking and analysis programs, and to interpret the experimental data.

GEANT keeps track of every single particle from the collision vertex where the particles were created, until they decay or interact with matter, which could be in other parts of the detector. All decay modes of all known particles are incorporated in the simulation program, and the modes are weighted by the probability of a decay. After a decay or an interaction, the new particles that were created will be tracked, and their path of flight, decay modes or probabilities of interaction with matter will be calculated by GEANT.

The input for GEANT simulations can either be simulated *data* from an event generator read in from a file, or an interactive session where the user specifies for every particle the energy, direction, identity etc. Examples of models used in event generators are FRITIOF 7.02 and HIJING 1.36.

BRAG is the GEANT simulation package for BRAHMS which contains the specific detector geometry for the detector setup. When running BRAG the user is able to *switch off* parts of the detector, called volumes, that are irrelevant for the particular simulation. The largest volume is called the cave and contains everything, i.e. all sub-volumes. The tile multiplicity array is an example of such a sub-volume. Figure 4.1 show what the BRAHMS detector setup looks like when viewed in an interactive BRAG session.

One can obtain BRAG by down loading it from the CVS at RHIC. An example of how to run a simulation with an event generator is given in appendix B.4. In the script used to run BRAG the BRAHMS geometrical setup is defined by loading files as `geoini, geodef` and `geofin`. These files initialize the geomtry used in the simulation. Magnet field settings are also defined here.

By choosing a BRAG session with a *HIGZ window*, one can view the paths of the particles as they fly through the detector system. This feature is illustrated in figure 4.2 where one FRITIOF 7.02 event is being processed.

The output of a simulation consists of four files containing settings for the magnet, geometry and the field used, as shown on figure 4.3. The fourth file with the suffix `.cdat`

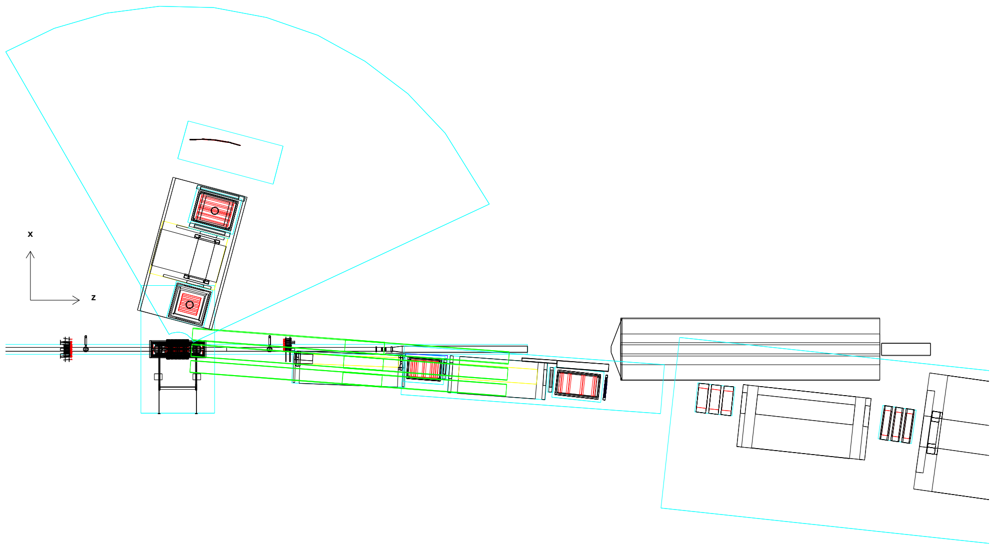

Figure 4.1: Top view of the BRAG detector setup, showing the midrapidity spectrometer at 75 degrees (top left) and parts of the forward spectrometer at 4 degrees (lower right). Note the defined coordinate system to the left.

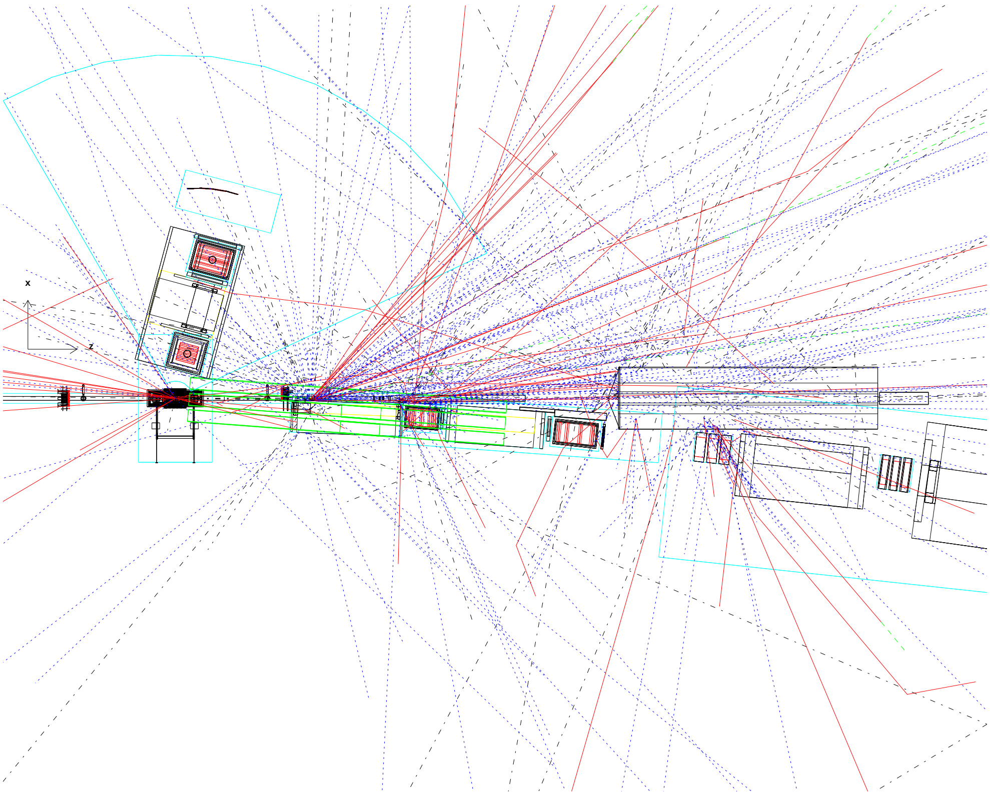

Figure 4.2: Screen shot from BRAG while running one central FRITIOF 7.02 event. The different line styles and colors symbolizes different particles. In this particular event no particle tracks go through the entire spectrometer, but many secondary particles are produced in the surrounding material.

contains information on all particles. This information includes coordinates of where the particle were created, particle identification, mass, momentum, energy deposit in a particular sub-detector unit, time-of-flight and coordinates describing where the particle has entered and exits a detector sub element [69].

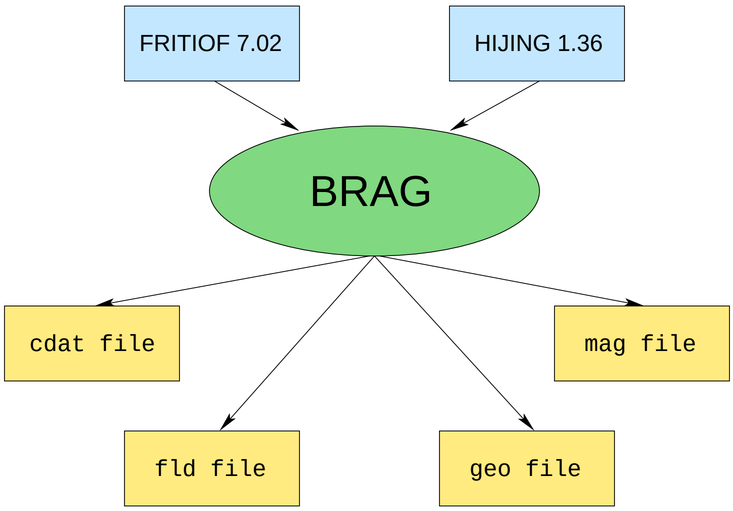

Figure 4.3: Event generators using models such as FRITIOF 7.02 and HIJING 1.36 are used as input for the BRAG simulation. In BRAG, the specific geometry, magnet and field settings are defined for the particular simulation. There are 4 outputs; a `cdat file` which contains the data in a binary format, a `fld file` with field settings information, a `geo file` with geometry settings and a `mag file` with information on the magnetic fields.

4.1 Simulation Models

Various models have been developed to attempt to describe the evolution in high energy collisions. Experimentalists compare these models with data in order to understand the physics of a collision. In this thesis two event generators were used: FRITIOF 7.02 and HIJING 1.36. In the following sections short descriptions of these models are presented and compared.

4.1.1 The FRITIOF 7.02 Model

The FRITIOF model was developed at Lund University. It has been modified over time and the version used in this analysis is 7.02. The model is named after FRITIOF, a god in old Nordic mythology. He used to call his wife, Ingeborg, to do all his dirty work [1]. Instead of Ingeborg, the FRITIOF model calls a number of subroutines from Pythia [73] to describe the collision.

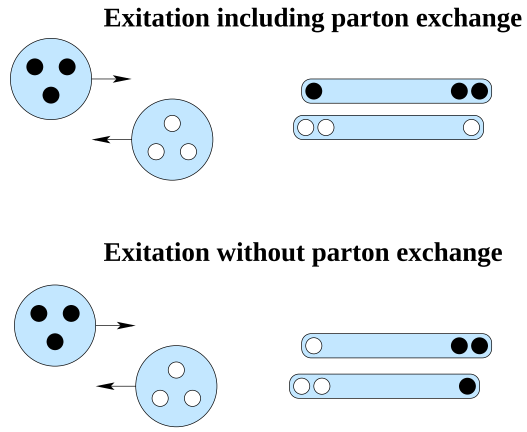

Figure 4.4: Longitudinal excitations of the two nucleons with and without parton exchange.

The FRITIOF model [70, 71] implements the Lund string model where a color string between the participants is fragmented into mainly $q\bar{q}$ pairs. In a collision the strings get exited and parton exchange may occur, as shown on figure 4.4.

The model assumes the geometry from a participant-spectator scenario for a given impact parameter and calculates the number of nucleon-nucleon collisions from a parameterization of the nuclear density distribution of the Wood-Saxon type:

$$\rho(\vec{r}) = \frac{\rho_0}{1 + e^{\frac{r - r_0 A^{1/3}}{C}}} \quad , \tag{4.1}$$

where ρ_0 is a normalization constant measured in Fermi, $A \geq 16$, r_0 is the radius parameter and C is the diffuseness parameter. C and r_0 depends on A. C varies from 0.47 to 0.55 and r_0 as $r_0 = 1.16(1 - 1.16A^{-2/3})$ [71].

The nucleons are not allowed to fragment between the nucleon-nucleon (NN) collisions, but may get further excited. Therefore fragmentation and meson production happens outside the nucleus. Interactions between the produced particles are also prohibited in the model. First when all nuclear interactions has been calculated, will the participant nucleons are treated according to the Lund string model [1].

FRITIOF 7.02 does not work for low energies, i.e. below 10 GeV per nucleon, because one can not assume that quark strings will be created or decay. At high energies, i.e. when $\sqrt{s_{NN}}$ is of the order TeV, the model needs to be modified, because of the large number of particles, that are produced. This is clearly seen in section 4.2.

The input file for FRITIOF 7.02 contains information on $\sqrt{s_{NN}}$ (in units of GeV), the colliding nuclei (for example Au), number of collisions to generate, the impact parameter range (in units of fermi) and an output file name. In appendix B.1 an example of such input file and usage is given.

4.1.2 The HIJING Model

The Heavy Ion Jet INteraction Generator (HIJING) Monte Carlo model was developed by M. Gyulassy and X. N. Wang with special emphasis on the role of mini jets in pp, pA and AA reactions at RHIC and LHC energies. The HIJING model used in this thesis is version 1.36.

The model implements hard and soft scatterings of the quarks and gluons (partons). The difference between hard and soft scatterings is defined by a transverse momentum of 2 GeV/c. Above this limit the scatter is defined as hard and is described by perturbative QCD that leads to a jet of particles.

HIJING subdivides the AA collision into collisions between the nucleons. The number is determined by the Glauber model, which calculates the geometry for multiple interactions using the impact parameter. The interacting partons are treated as strings accordingly to the Lund string model. In FRITOF the strings are not allowed to re-excite; they are in HIJING [6].

Jet quenching described in section 2.5.3 is also implemented in the default HIJING. An average energy loss (induced gluon radiation) is assumed for partons moving transversely through the medium. HIJING calculates the interaction points by assuming a free mean path of the form

$$dP = \frac{dl}{\lambda_s} \cdot e^{-\frac{l}{\lambda_s}} \tag{4.2}$$

where l is the length traveled in the medium and λ_s is the free mean path [6].

For relativistic heavy ion collisions the program limits it to the energy range of approximately 10 GeV $\leq \sqrt{s_{NN}} \leq$ 10 TeV per nucleon [72]. Information on how to get the HIJING model running can be found in B.2.

4.2 Comparison of Models

Comparing data with different models may provide information for the experimentalist on the collision physics. Model assumptions may also be incorrect which may lead to reject certain models, as we shall see in the following.

The prediction for the $N(\bar{p})/N(p)$ ratio varies for the models. As seen in figure 4.5 HIJING over-predicts the ratio by roughly 0.2 at midrapidity compared to BRAHMS measurements [13]. The FRITIOF 7.02 model predicts the ratio. A third model, the Ultra Relativistic Quantum Molecular Dynamics model (UrQMD) [74] under predicts the ratio roughly by 0.3.

FRITIOF and HIJING are both partonic models and therefore takes into account that the two colliding nuclei consist of quarks and gluons which may interact during or after the collision. The UrQMD model is a hadronic model in the sense that it does not implement the quark structure. The model implements quantum field theory by assigning a state equation for each nucleon and thereafter relating these equations by a Lagrangian [74].

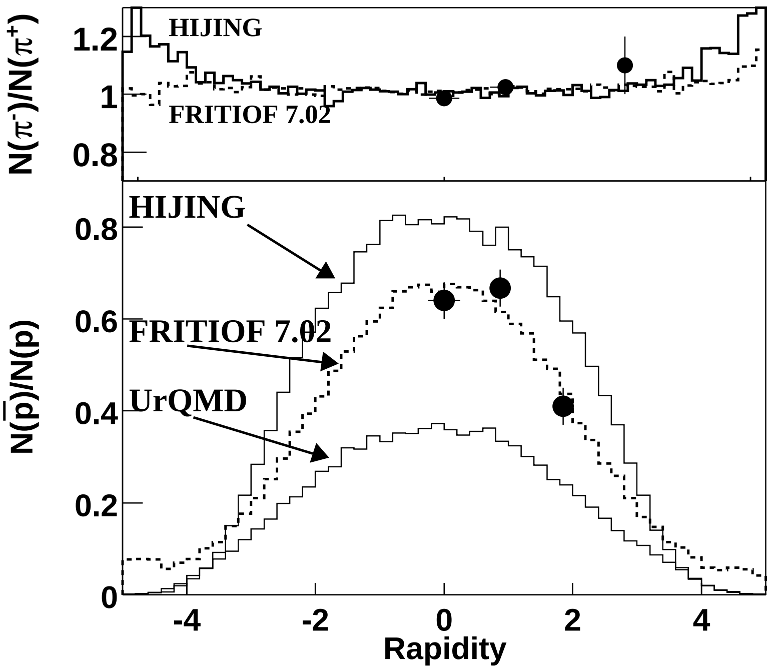

Figure 4.5: Comparison of the BRAHMS $N(\bar{p})/N(p)$ measurements with various models [13].

The ratio $N(\pi^-)/N(\pi^+)$ also shown in figure 4.5 provides information on the charge distribution of the collision zone. In transparent collisions it is expected that the rate is constant, because the energy of the initial nucleons will be at higher rapidities [13].

Examining multiplicity predictions of the different models as shown in figure 4.6 show that HIJING predicts the measured multiplicity, UrQMD slightly over predicts and FRITIOF way over the experimental measured values at midrapidity.

So far no model can reproduce all aspects of Au+Au collisions at $\sqrt{s_{NN}} = 130$, but since the HIJING model seems to be most consistent with measured multiplicities, this model will be most frequently used in the analysis.

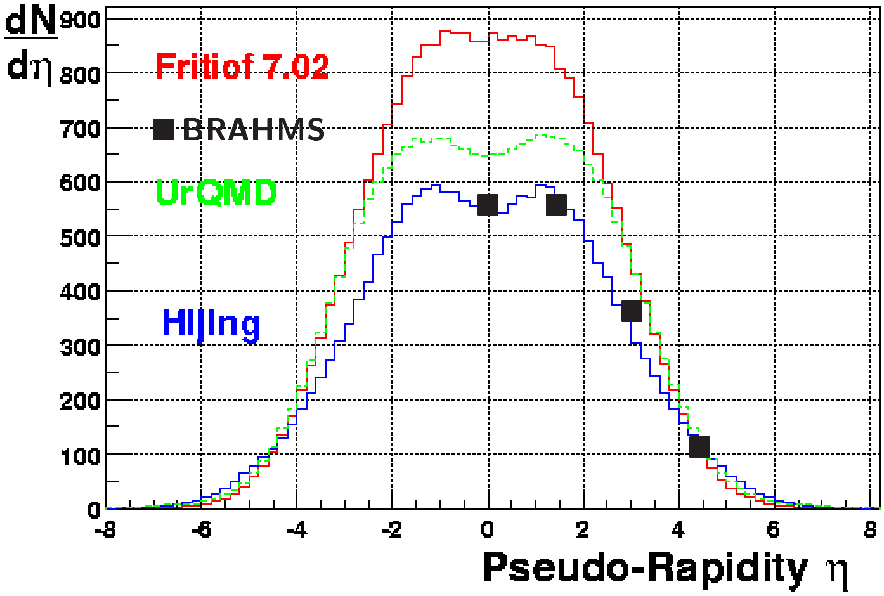

Figure 4.6: BRAHMS measured $dN_{ch}/d\eta$ at $\sqrt{s_{NN}}$ = 130 GeV for 0 to 5% central events [31]. The measurements are compared with model calculations from FRITIOF, UrQMD and HIJING. It is noticed that the FRITOF model over predicts the multiplicity and at midrapidity the model does not reproduce the *dip*, which is also seen on the data in figure 2.18. The UrQMD model has the right shape, but is still over predicting the multiplicity. The HIJING model, on the contrary, reproduces the multiplicity and this model is therefore used in the later fluctuation analysis. For large pseudorapidities, i.e. $|\eta| \geq 4$, all models seem to agree.

Chapter 5

Analysis of Charged Particle Multiplicity

This chapter focuses on the charged particle multiplicity detected by the tiles in the multiplicity array. After a short description of the software and methods used in the analysis, concepts such as vertex selection, calculating the multiplicity and determining the centrality will be described. Comparison of measured data multiplicity to simulated HIJING multiplicities are also made in this chapter. A charged particle multiplicity distribution ($\frac{dN}{d\eta}$) is presented for the data and the simulated HIJING events. These distributions are compared to the published BRAHMS results in [31]. An estimate of the ratio of detected secondary particles to the total number of detected particles is made using FRITIOF events and the simulation program BRAG. The ratio will be compared to earlier independent estimates.

5.1 BRAHMS Analysis Toolkit

C++ is the *object oriented* programming language on which the ROOT [1] framework is build upon. This framework supplies different services, such as histograms and data storage. For the BRAHMS experiment, more specialized tools are needed than the ones provided by ROOT, and so the BRAHMS Reconstruction and Analysis Toolkit (BRAT) [75] has been and is continuously being developed.

The strong advantage in using *object oriented* programming instead of procedural oriented languages such as Fortran or Pascal, are concepts such as inheritance and polymorphism. Inheritance is a way to reuse existing classes by absorbing their attributes and behavior. This saves time in the programming process. Polymorphism makes it possible to write code in a generalizable way so that they can handle existing classes and classes that have not yet been specified.

[1] ROOT is an acronym for **R**OOT's **O**bject **O**riented **T**echnologies.

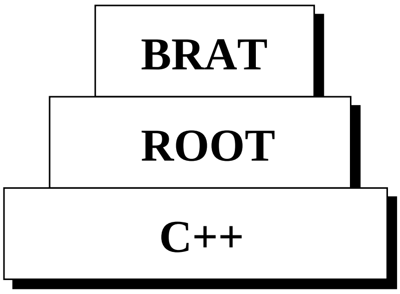

Figure 5.1: BRAT is the specific toolkit for the BRAHMS experiment. It is based on the framework of ROOT, which is written in C++.

The development of BRAT is an ongoing process and so different versions have been used in the analysis described in the following sections. BRAT 2 has been used throughout the present analysis, except in section 5.6, where version 1 was used.

5.2 Analysis Overview

The different reduction stages applied to measured data and simulated HIJING events are shown in figure 5.2. The comparatively many separate sequential steps in the analysis makes it easier to check and debug. In chapter 6 a slightly different method to analyze simulated HIJING events will be introduced, but for the multiplicity and in some of the fluctuation analysis the following method is used.

The first step is to create an event generator input file (`EG file`), in this case a HIJING file. The procedure of making such a file is described in appendix B.2. The output of a HIJING simulation, the `EG file`, is then used as input for the BRAG simulation. This input could just as well be replaced with a FRITIOF event, if such simulation is wanted. BRAG then uses the event generated file to calculate a simulated event for the detector, as described in chapter 4.

The data from the tiles and the beam-beam counters in BRAG simulated output file (`cdat` file) are then digitized by the routines `BrDigitizeBB` and `BrTileDigModule`. This is done by running the script `DigConfig.C` with the BRAT program `bratmain`.

The script `RecoConfig.C` is used for real as well as simulated data, but with a flag set, since it is necessary to differentiate between the two types of input data. The modules applied are `BrGeantInput` and `BrRawDataInput` for simulated data or raw data, respectively. The script reduce the simulated data or data files, so that only data regarding the tiles and beam-beam counters is analyzed. The script also applies a vertex cut at ± 50 cm, in order to eliminate events outside the multiplicity array.

The reconstructed output is then added on to a data tree with the script `TreeConfig.C` which uses the module `GlbTreeModule`. This module reads the reduced data objects `BrMultRdo` and `BrBbRdo` in the `reco` file created by `RecoConfig.C`. The final data is added onto a ROOT `TTree` which contains branches for tile and beam-beam data. A `TTree` consists of a list of independent branches which again has its own definition and list of buffers. The output TTree file is then ready for analysis by the program data2cov.cxx.

In the analysis program various cuts on centrality and vertex location may be applied. In the essence the program chains many generated TTree files by the ROOT module TChain is a loop over a number of events. During this loop the average, mean and spread of the multiplicities are calculated. Using the BRAT statistics utility class (BrStatistics) the covariance is calculated in this program here as described in section 6.

5.3 Vertex Selection

The vertex used in the analysis is the *beam-beam vertex*, which was earlier described in section 3.5. By only selecting events close to the nominal vertex the change in geometrical acceptance of the tiles will be minimized. The resolution of the beam-beam vertex is ≈2 cm and the selected vertex cut has therefore been chosen to ± 2.5 cm.

Applying the vertex cut close to nominal vertex implies that every tile will correspond to a certain pseudorapidity range, covering a total in pseudorapidity of -1.99 $\leq \eta \leq$ 1.99. The exact coverage is listed in table 3.1.

Figure 5.3 shows vertices fitted with a 0 degree polynomial. The reason for fitting the vertex distribution is that the BRAG simulated HIJING events will be made with a equivalent flat vertex distribution. By selecting only events in a narrow interval around nominal vertex, the vertex distribution looks as follows in figure 5.4.

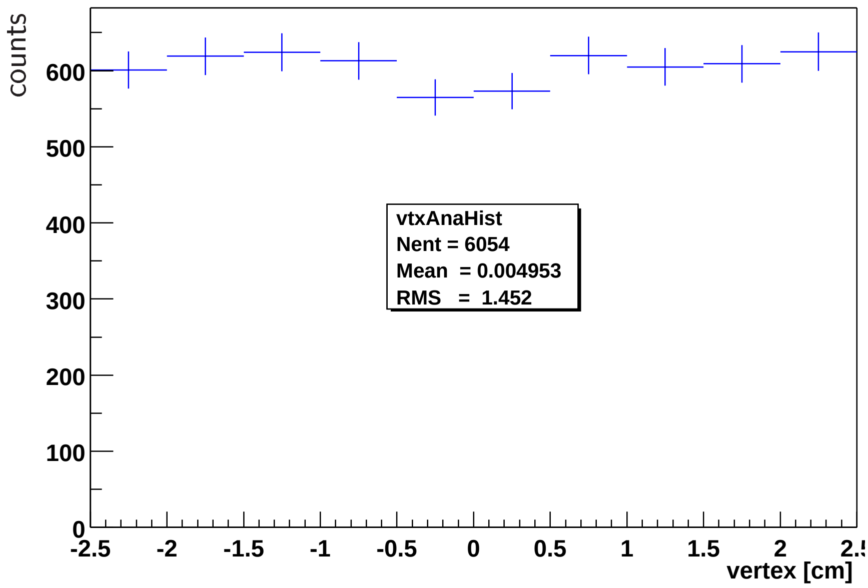

Figure 5.4: Vertex distribution for $|z| \leq 2.5$ cm (6.054 events) using timing from the beam-beam counters.

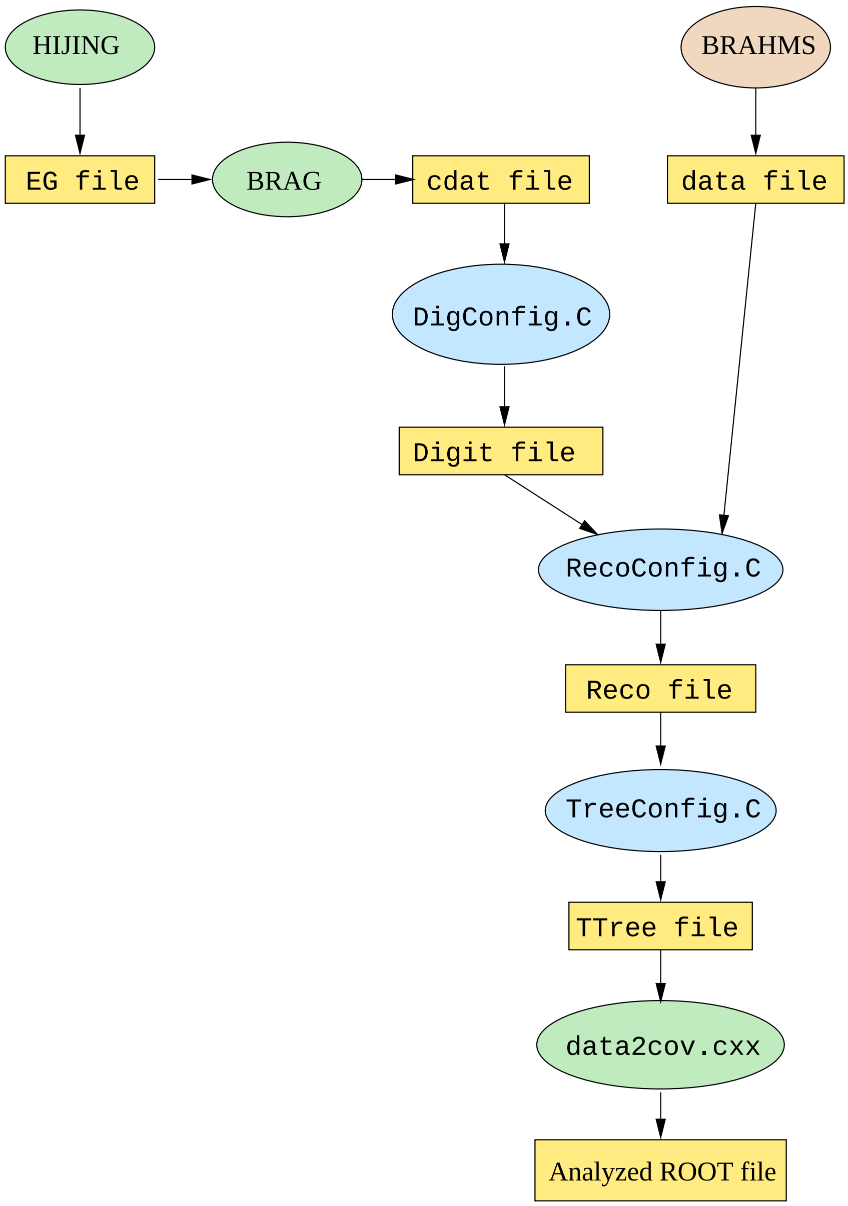

Figure 5.2: Data analysis flow diagram showing step-by-step the different elements of the data analysis. See explanation in text.

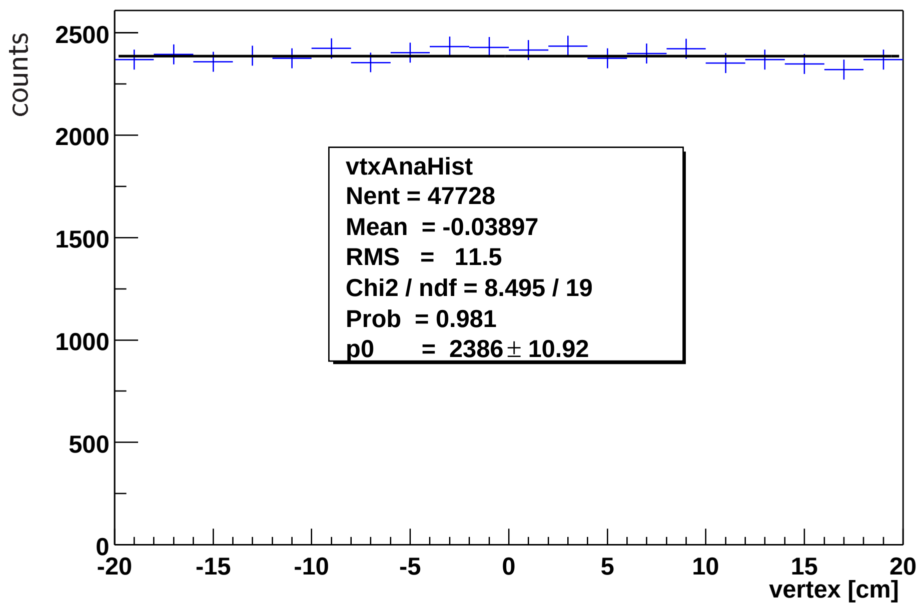

Figure 5.3: Vertex distribution for $\mid z \mid \leq 20$ cm (47.728 events) using timing from beam-beam counters.

5.4 Measuring the Multiplicity

In the following the charged particle multiplicity is referred to as the multiplicity. The multiplicity is calculated from the energy signals (ADC signals) of the tiles. The conversion from ADC signal to multiplicity includes several corrections and calibrations that are described in the following.

For every event there are 38 ADC signals, i.e. one for each tile. Each signal first has to be corrected for a dual dynamic range (0.05 pC/channel and 0.4 pC/channel). The dual range correction is done by subtracting the gap between the low and the high channels from the i^{th} tile's ADC value. The gap is typically around 4000 channels.

$$ADC_i' = \begin{cases} ADC_i & \text{for } ADC_i \leq Gap_{i,low} \\ ADC_i - (Gap_{i,high} - Gap_{i,low}) & \text{for } ADC_i > Gap_{i,low} \end{cases},$$

A typical spectrum before and after *gap correction* is shown in figures 5.5 and 5.6 respectively. The advantage of the dual range is that it has very large dynamic range.

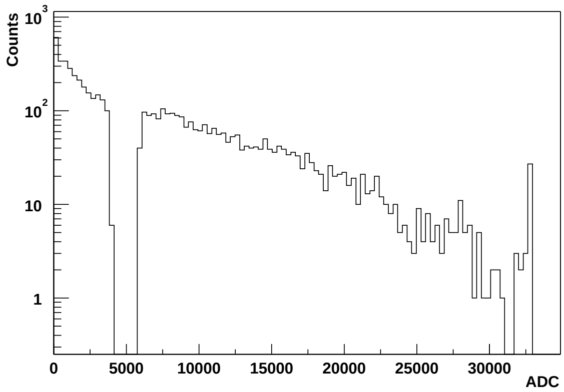

Figure 5.5: Typical ADC distribution for a tile (tile 4) before gap correction.

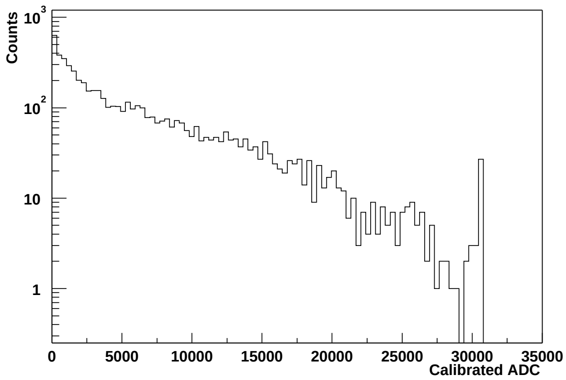

Figure 5.6: Typical multiplicity distribution a tile (tile 4) after gap calibration has been performed.

All ADC values that are below threshold are now subtracted. In order not to pollute the signal, 4 times the pedestal width is set as threshold for the individual hits. Calibrations with cosmic muons is used to translate the ADC values to an energy deposit in the tile.

When calculating the multiplicity one has to consider how far the particle has traveled in the tile. Depending on the incoming angle (θ) the particle travels a distance and deposits energy proportional to the distance traveled, i.e. the further the average particle travels, the more energy will be deposited and hence a larger measured multiplicity, if not corrected. The multiplicity therefore has to be calculated with respect to a given collision vertex, as shown in figure 5.7. When calculating the multiplicity in this way, it is assumed that the particle on average hits the tile in its center. From geometrical considerations it can be seen that a particle with an incoming angle θ deposits a factor $1/sin(\theta)$ more energy than the cosmic muons, that were used to calibrate the tiles in the lab [85]. The cosmic muons are assumed to penetrate the tile perpendicular ($\theta = 90$ degrees).

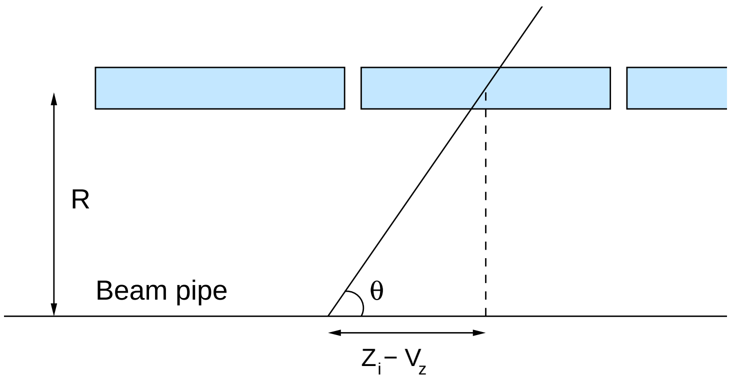

Figure 5.7: The vertex correction for the tiles.

In general, the correction factor $f_i(V_z)$ for the i^{th} tile's position is given by

$$f_i(V_z) = \sin\left(\theta_i(V_z)\right) = \frac{R}{\sqrt{(Z_i^2 - V_z^2) + R^2}} \quad ,$$

where R is the radial distance from beam axis to the tile, Z_i the i^{th} tile's position along the beam axis, and V_z the primary vertex position along the beam axis.

In practice the multiplicity is derived by using a transformation function which is derived from BRAG simulations [41] using HIJING as input. The function includes the rescattering of average energy losses, the geometrical correction mentioned above, and a correction for secondary particles.

The measured minimum bias multiplicities agree well with predictions from the HIJING model with and without jet quenching, as shown in figure 5.8. FRITIOF over predicts the multiplicity when compared to data and simulated HIJING events, which is also seen in figure 4.6. The measurements are based on runs 2336 and 2355-2357 taken in August of year 2000 at the first RHIC running at $\sqrt{s_{NN}} = 130$ GeV.

In the following the multiplicity will be examined as a function of η. In this analysis the 4 tile rows that are completely filled will be analyzed. The rows are defined in the following way. The row containing tiles with numbers 0 to 7 (see conventional numbering in figure 3.7) is denoted row 0007. Row 0815 will denote the row that contains tiles from number 8 to 15 and so forth with row 2431 (tiles 24 to 31) and row 3239 (tiles 32 to 39).

Figure 5.9 shows the average multiplicities for these rows with a centrality cut from 0% to 50%. The upper figure show measured data and the lower part show simulated HIJING events.

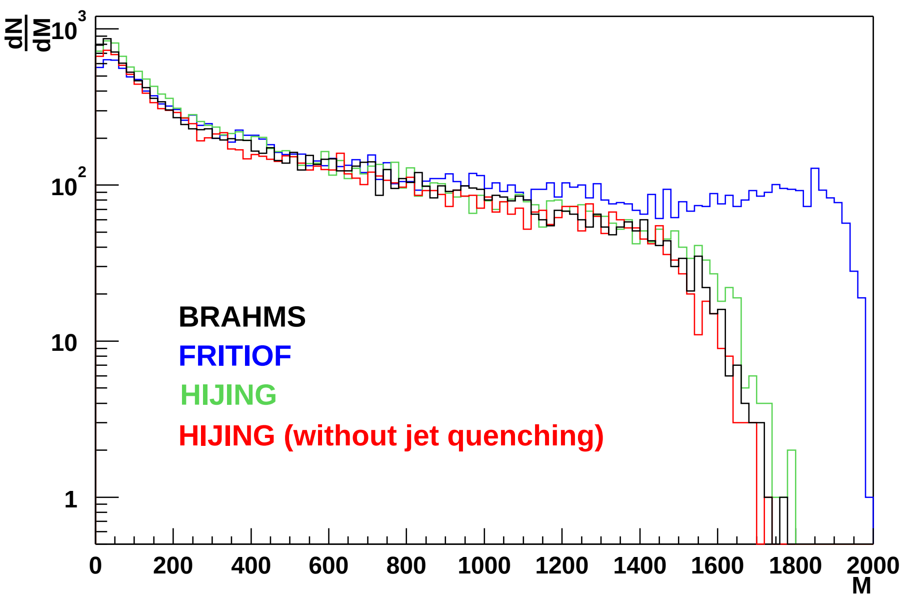

Figure 5.8: Multiplicity distributions for ∼12.000 minimum bias events. The green distribution is simulated HIJING events with jet quenching, the red is for HIJING events without jet quenching, the blue curve denotes FRITIOF events, and finally does the black curve denote data from the BRAHMS experiment, used in the fluctuation analysis. The over prediction in multiplicity from FRITIOF is also evident, when looking at the $\frac{dN}{d\eta}$ distributions in figure 4.6.

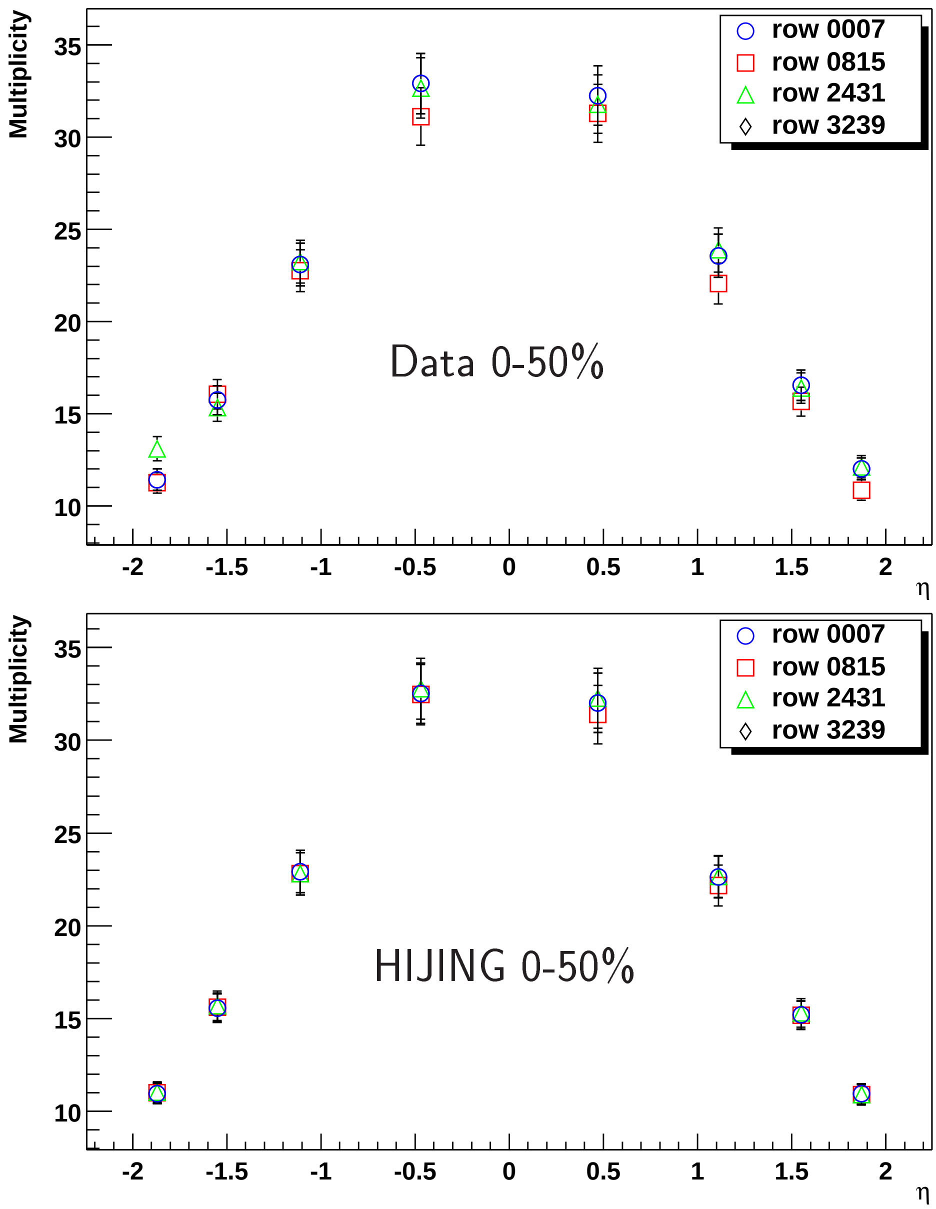

Figure 5.9: Average multiplicities vs. η for data (top) and BRAG simulated HIJING events (bottom) for 4 different tile rows. The centrality cut on the events is from 0 to 50%, which corresponds to about 6.000 analyzed events. Row 0007 correspond to tiles number 0 to 7 in row A, shown in figure 3.7. Rows 0815 (tiles 8 to 15), 2431 (tiles 24 to 31) and 3239 (tiles 32 to 39) correspond to rows B, D and E, respectively. Within the 5% systematic error bars shown the points seem to agree, for a given η bin and when comparing simulation with measurements. The width of each η bin corresponds to the η range covered by each ring (see table 3.1 for the bin size).

The statistical error on the average multiplicity is very small. The error plotted in figures 5.9 and 5.10 is the systematical error, which has been set accordingly to 5% [31]. The systematic error estimate is based on GEANT background simulations and from the scaling between GEANT and data. Comparing the experimental data in figure 5.9 with the HIJING simulation it is concluded that the average multiplicities in the 4 rows agree well for the 0 to 50% central events.

For a given η the multiplicity is expected to be constant as one observes different angles (ϕ). The average multiplicity as a function of ϕ for all tiles has been plotted in figure 5.10 for data (top) and for BRAG simulated HIJING events (bottom). The rings with same pseudorapidity coverage have practically the same average multiplicity, i. e. rings 0 and 7, rings 1 and 6 etc. (see figure caption). The average BRAG simulated HIJING events have a slightly more consistent average multiplicity, but a good overall consistency is observed.

5.5 Centrality

Experimentalists can not directly measure the impact parameter described in section 2.4.1, instead, the centrality of *one* event is defined relative to a whole ensemble of events corresponding to all impact parameters (minimum bias events). A minimum bias (MB) event is in this context defined as a trigger 4 (described in section 3.4) event with at least one hit in one of the tiles. The argument is that a given fraction of the MB distribution corresponds to the same fraction of the nuclear interaction cross section. This can in turn geometrically be related to a range of impact parameters, as shown in figure 2.7. Examining the total multiplicity of a given minimum bias ensemble ($\frac{dN}{dM}$) as shown in figure 5.8, one can from this distribution define, say, the 5% most central events in the following way: Starting at the bin with highest multiplicity in the histogram shown in figure 5.8 one can integrate the area from that bin to the neighbor bin with lower multiplicity. By dividing this area with the total area, one can determine the fraction of centrality. By iteratively integrating and evaluating the area fraction, the centrality can be determined. This should of course be done in a histogram with one bin per multiplicity in order to minimize errors.

The analysis is done by making two loop over the events. The first loop creates the minimum bias multiplicity distribution ($\frac{dN}{dM}$) for the events within the vertex cut.

The distribution is then integrated until the x% to y% most central events are determined. Multiplicities corresponding to the chosen centrality cut are then used in the second event loop. Only events within the cut are accepted, and are used in the final fluctuation analysis.

In figures 5.12 and 5.13 centrality cuts of respectively 0 to 10% and 30 to 40% are shown for given minimum bias multiplicity distributions. The reason for the fine histogram binning is to minimize error when integrating the multiplicity curve, when calculating the centrality.

The multiplicity distribution in figure 5.9 where made for 0 to 50% central events with the described cut. Now for more central events there should be produced more particles in the collision, which can also be observed when comparing figure 5.9 (0-50%) to fig-

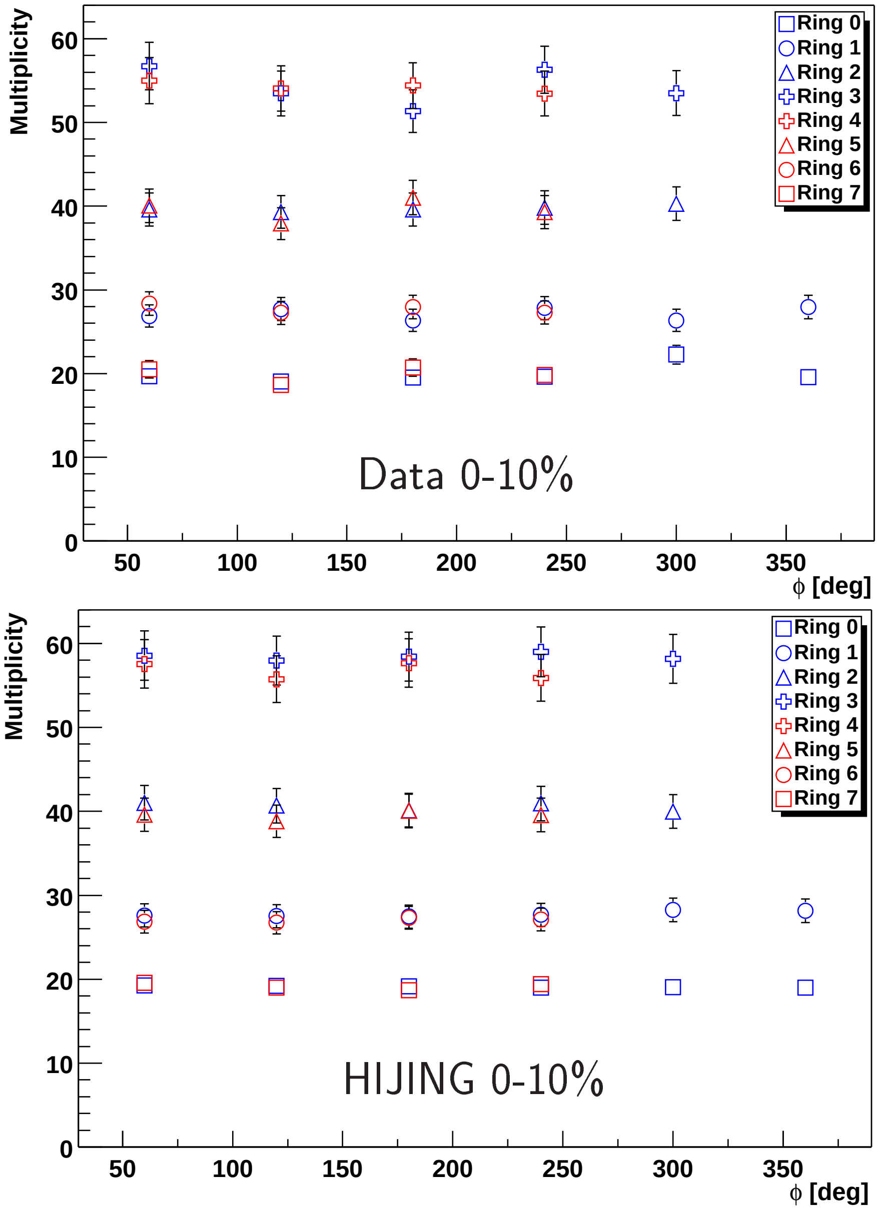

Figure 5.10: Average tile multiplicity vs. azimuthal angle (ϕ) for data (top) and BRAG simulated HIJING events (bottom) for rings at different η (see table 3.1), i.e. ring 0 and 7 corresponds to $|\eta| \in [1.73; 1.99]$, rings 1 and 6 to $|\eta| \in [1.36; 1.72]$, rings 2 and 5 to $|\eta| \in [0.83; 1.35]$ and rings 3 and 4 to $|\eta| \in [0.03; 0.80]$. A centrality cut from 0 to 10% has been applied. It is noted that the average multiplicities are pairwise constant as a function of ϕ, as expected. It is also seen that rings located at $\pm\eta$ are consistent. The error bars show the 5% systematic error on the multiplicity. The statistical error is smaller than the points, as shown in figure 5.11.

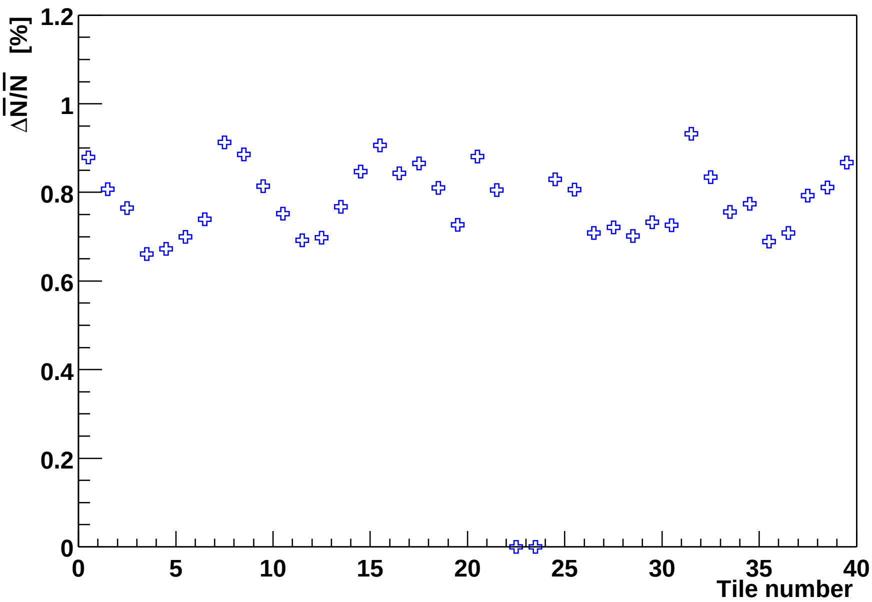

Figure 5.11: Statistical uncertainty ($\Delta\overline{N}/\overline{N}$) for the average multiplicity measured in %. The periodic peaks correspond to tiles located at the end of the array, i.e. rings 0 and 7. The smallest error correspond to tiles with high multiplicity, i.e. at midrapidity. Note that the tiles here are numbered from 1 to 40 and that tiles 22 and 23 were removed. See figure 3.7 for the conventional tile numbering.

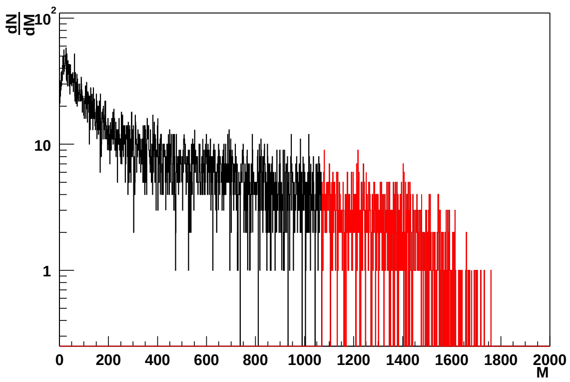

Figure 5.12: Illustration of the centrality cut in multiplicity distribution of the 0 to 10% most central events

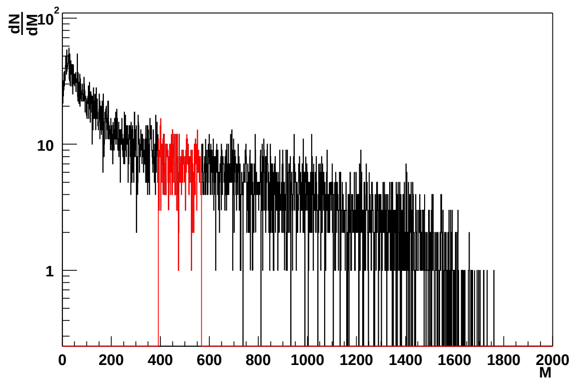

Figure 5.13: Illustration of centrality cut from 30 to 40%.

ure 5.14 (0-10%).

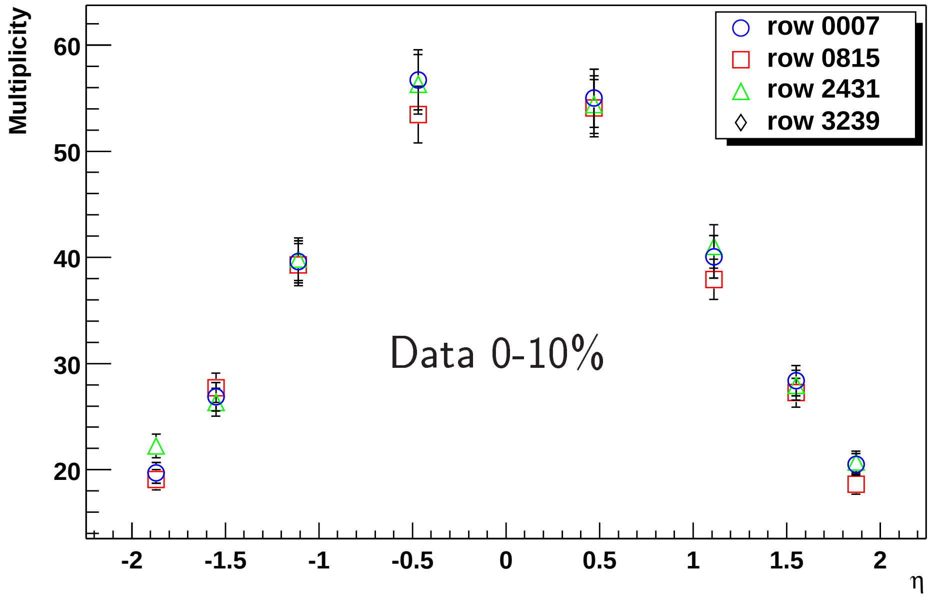

Figure 5.14: Average multiplicities from 4 different tile rows. The centrality cut on the events is now from 0 to 10%, where as it in figure 5.9 was from 0 to 50%. The difference in average multiplicity for the two centralities is also noticed.

For various centrality cuts, the average multiplicity vs. η are now plotted in several $dN/d\eta$ distributions, shown in figure 5.15 for data (top figure) and BRAG simulated HIJING events (bottom figure). When comparing the values of $dN/d\eta$ to figure 2.18 the multiplicities are consistent. The shape of the distribution is also the same within the acceptance of the tiles ($-2 \leq \eta \leq 2$).

5.6 Estimate of Secondary Particles to Measured Multiplicity

The multiplicity measured in the acceptance of the tile array is different than the actual multiplicity. The reason for this is that particles may decay or interact with matter on the path from the collision to the detector. A detector may also itself contribute to the production of secondary particles via scattering or capture. This is seen clearly from the tracks in the simulation picture (figure 4.2) in the previous chapter. Major scattering from other detector elements and their support structure, the beam pipe and the tiles themselves

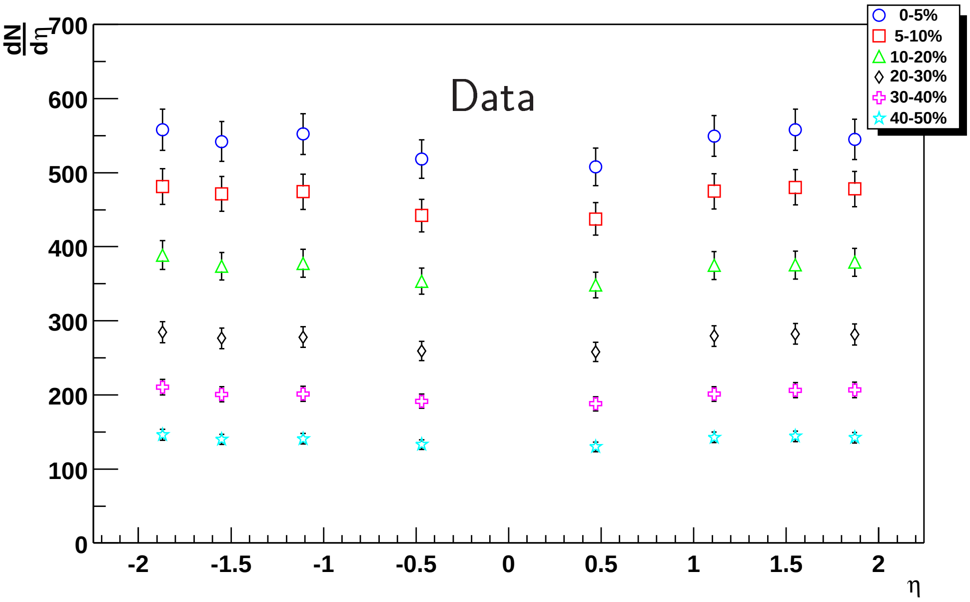

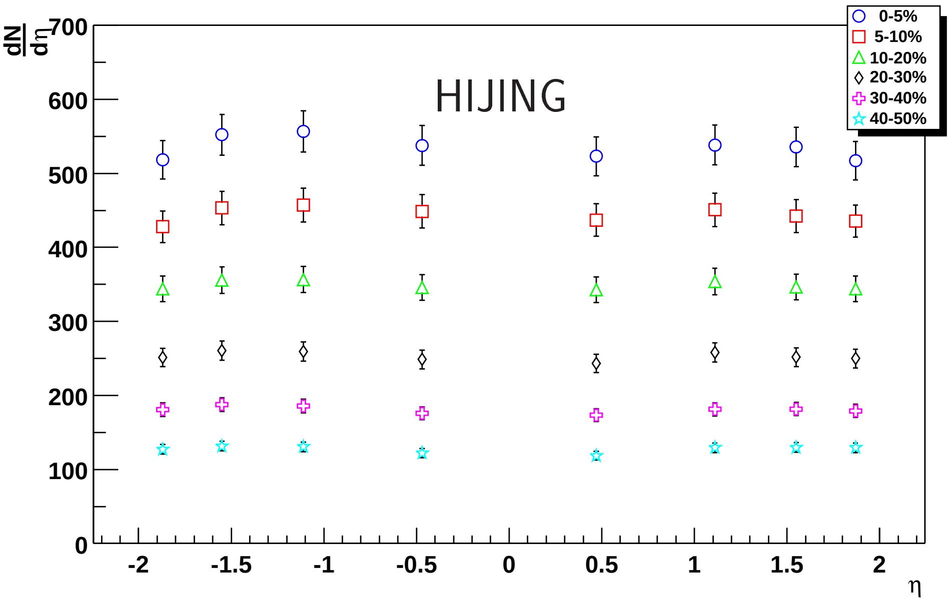

Figure 5.15: Charged particle $dN/d\eta$ for data (top) and BRAG simulated HIJING events (bottom) for various centrality cuts. The data has been corrected for a 95% trigger efficiency. By comparing with previous published results for the BRAHMS collaboration (figure 2.18) it is concluded that the measured multiplicities and BRAG simulated HIJING multiplicities are consistent. The error bars are 5% systematic.

are sources of secondary particle production. Experimental multiplicity distribution must therefore be corrected for the contribution from secondaries. Since there is in general no way of identifying secondary particles in the absence of very precise individual tracking, the number of secondaries must be evaluated from simulations.

5.6.1 Defining Secondaries Ratio

The detected particles are a mixture of primary and secondary particles. The total number of particles in a given event, is the sum of primary and secondary particles, i.e.

$$N_{tot} = N_{sec} + N_{pri} \tag{5.1}$$

The definition of a primary particle chosen here, is a particle that would have hit the detector if there were nothing between the collision zone and the tiles. This definition removes eliminates all secondary particles that would have been created by hadronic interactions.

An alternative definition could be to define a primary particle as a particle that was created in some well defined volume containing the collision vertex. This includes all fast decaying particles, but not the slow decaying particles. This definition has been used in previous simulations made at Brookhaven National Laboratory. Another definition could be to say that a primary particle is one, that has the direction towards the detector at nominal vertex. The problem with the last definition is that the detector is not 100% efficient, and so not all particles are detected.

Having defined secondary particles, the secondary ratio can be defined as the number of secondary particles divided with the total number of particles, i.e.

$$R_s = \frac{N_{sec}}{N_{tot}}$$

5.6.2 Simulation Strategy

All simulations for estimating the secondary ratio were made using the FRITIOF 7.02 model as the input event generator. The file contained 1000 events with b ranging from 0 to 2 fm calculated at an energy of $\sqrt{s_{NN}} = 130$ GeV. It was assumed that the correction factor is symmetric around the vertex and so only 4 of the 8 bins in pseudorapidity were evaluated, corresponding to the η intervals [-1.99;-1.73], [-1.72;-1.36], [-1.35;-0.83] and $[-0.80; -0.03]$, as mentioned earlier in table 3.1. The intervals corresponds to rings 0 through 3 respectively.

The strategy behind the different simulations were, that by switching off different detector elements off, estimates can be made of the contribution of the individual detector components to the production of secondaries. The way to do this in BRAG is described in appendix B.3. By switching off hadronic interactions it is assumed that the production of secondaries due to interactions with matter, are inactive. The detector volumes were made inactive by editing the file: `brag/src/user/zigeom.F` as described in appendix B.3 and thereafter recompiling BRAG. The six simulations (A to F) were:

Detector element	A	B	C	D	E	F
Beam pipe	+	+				
Silicon detectors	+	+	+	+		
Tile support	+	+	+			
Hadronic interactions	+		+	+	+	
Described in section	5.6.3	5.6.4	5.6.5	5.6.6	5.6.7	5.6.8

Table 5.1: Secondaries simulation overview. The (+) indicates which elements were active during simulations A to F.

5.6.3 Reference Simulation

The reference simulation (A) is defined as a simulation with every component of the detector active and by including hadronic interactions. Figures 5.16 and 5.17, show the reference simulation for two selected rings, numbered 0 and 3, corresponding to a range in η of $[-1.99; -1.73]$ and [-0.80;-0.03], respectively. The histograms show the energy deposit in all tiles. A cut on 100 MeV energy deposit has been applied. The energy deposit has a characteristic maximum at the minimum ionizing particle peak, as it can be seen in figures 5.16 and 5.17. By assuming that the energy deposit is made by minimum ionizing particles, the multiplicity can be calculated by dividing the total energy deposit by the energy deposit from a single minimum ionizing particle or by rescaling the MIP energy by the average energy deposit, i.e. $\overline{dE} = \alpha E_{MIP}$. Since it is only the ratio that is being calculated, the error (α) in assuming that all particles are minimum ionizing will be divided out. Notice on figure 5.17 a strange bump to the left of the MIP peak. The reason for this is still not known, but seems to be consistent on the rest of the plots covering this η (ring 3).

Later in this thesis, fluctuation of the multiplicity will be analyzed. In this context the fluctuation of the deposited energy around the mean is of interest. This is fluctuation calculation is entirely given by the RMS of the spectrum of deposited energy.

Simulation A shows what the *expected measurement* would look like and will in the following sections be compared to simulations B to F, shown in figures 5.18, 5.19, 5.20, 5.21, 5.22, 5.23, 5.26 and 5.27 in order to estimate the ratio of secondaries.

5.6.4 Simulation without Hadronic Secondaries

In order to compare figure 5.16 and 5.17 with the simulation without hadronic interactions (B), i.e. figures 5.18 and 5.19, the following equation is used to estimate number of primaries [76]:

$$N_{pri} = \frac{E_{pri}}{\overline{dE}_{pri}} = \frac{E_{tot} - E_{sec}}{\overline{dE}_{pri}} = \frac{E_{tot} - N_{sec} \cdot \overline{dE}_{sec}}{\overline{dE}_{pri}} \tag{5.2}$$

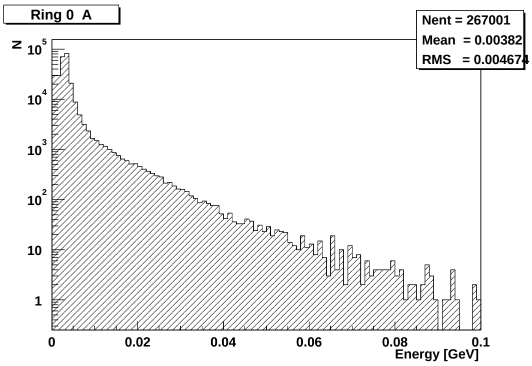

Figure 5.16: Energy deposit in tiles for ring 0 with $\eta \in$ [-1.99;-1.73].

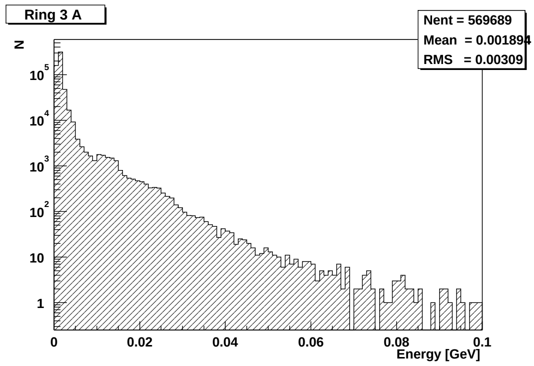

Figure 5.17: Energy deposit in tiles for ring 3 with $\eta \in$ [-0.80;-0.03].

where E_{pri} is the energy deposited by primaries in tiles per event, E_{sec} is the energy deposited by secondaries per event, E_{tot} is the total energy deposited in a tile per event and N_{sec} is the number of secondary particles from the simulation. $\overline{dE}_{sec}$ is the average of energy loss spectrum of the secondaries, which is formulated in equation 5.3. $\overline{dE}_{pri}$ is the average energy of the energy loss spectrum of the primaries, which is calculated from simulations without secondary sources.

$$\overline{dE}_{sec} = \frac{\overline{dE}_{tot} \cdot N_{tot} - \overline{dE}_{pri} \cdot N_{pri}}{N_{sec}} \tag{5.3}$$

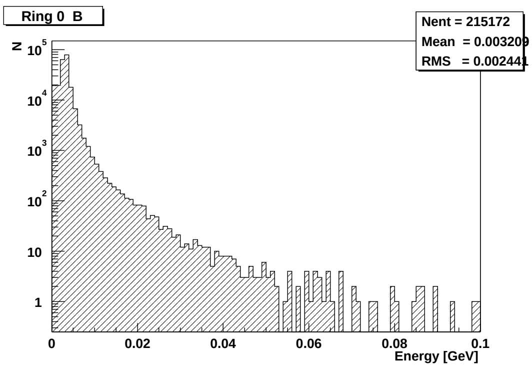

Figure 5.18: Energy deposit in tiles for ring 0 with $\eta \in$ [-1.99;-1.73]. No hadronic interactions included.

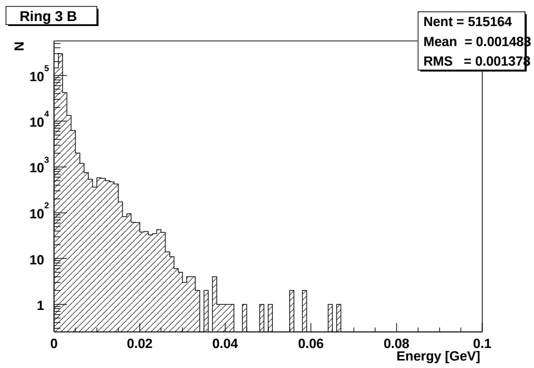

Figure 5.19: Energy deposit in tiles for ring 3 with $\eta \in$ [-0.80,-0.03]. No hadronic interactions included.

Simulations for $\eta \in$ [-1.72;-1.36] and $\eta \in$ [-1.35;-0.83] (rings 1 and 2) are shown in appendix B.5. Details for calculating the ratio R_s are included here for simulation B with $\eta \in$[-0.80;-0.03]. Equations 5.2 and 5.3 are used to calculate N_{pri} and $\overline{dE}_{sec}$.

$$E_{tot} = \frac{569689 \cdot 0.001894}{1000\, events} = 1.079\ GeV/event$$

$$N_{sec} = \frac{569689 - 515164}{1000\, events} = 54.5\, secondaries/event$$

$$\overline{dE}_{sec} = \frac{0.001894 \cdot 569689 - 0.001488 \cdot 515164}{569689 - 515164} = 0.005710\ GeV/\text{particle}$$

where the above values has been taken from figures 5.17 and 5.19. By inserting these values in 5.2, the number of primaries particles are 516 particles. This should be compared to:

$$\frac{E_{tot}}{\overline{E}_{pri}} = \frac{1.079\ GeV/event}{0.001488\ GeV/\text{particle}} = 725 \text{ particles} \tag{5.4}$$

When comparing simulations A and B for ring 3, the ratio R_s is: $\frac{725-516}{725} \cdot 100\% = 29\%$. For ring 0 similar calculations gives a difference of 32%. Equivalent calculations has been made to calculate the ratio for the simulations C to F. In the following only energy deposit histograms and the ratio will be mentioned.

5.6.5 Simulation without Beam Pipe

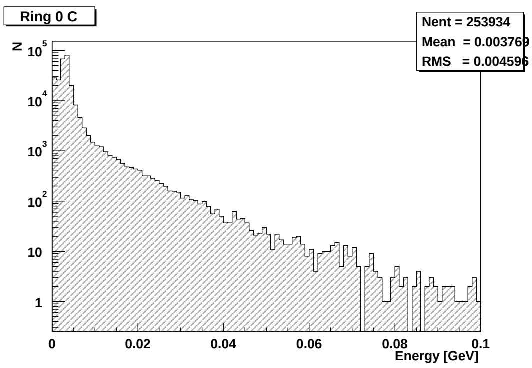

Figure 5.20: Energy deposit in tiles for ring 0 with $\eta \in$ [-1.99;-1.73]. No beam pipe.

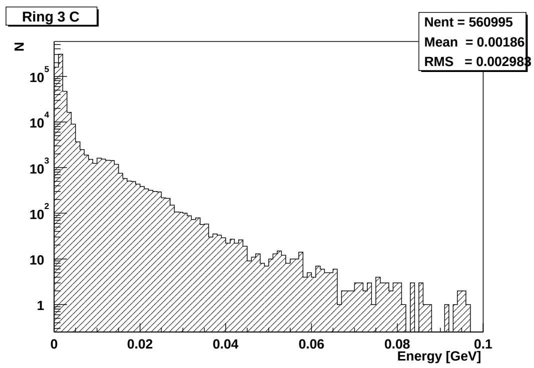

Figure 5.21: Energy deposit in tiles for ring 3 with $\eta \in$ [-0.80;-0.03]. No beam pipe.

The difference in multiplicity of simulation A and C, can now be calculated using formula 5.2 and data from figures 5.20 and 5.21. The results from 1A and 1C is 6.3% and for simulations 4A and 4C it is 3.3%. This shows that the beam pipe does not contribute significantly to the production of secondaries.

5.6.6 Simulation without Tile Support and Beam Pipe

Now taking a look at the situation where both beam pipe and tile support is inactive (graphs 5.22 and 5.23), the percentage deviation is 15% for 1D and 13% for 4D. The simulations show that the support for the tiles roughly contributes of about 10% secondaries.

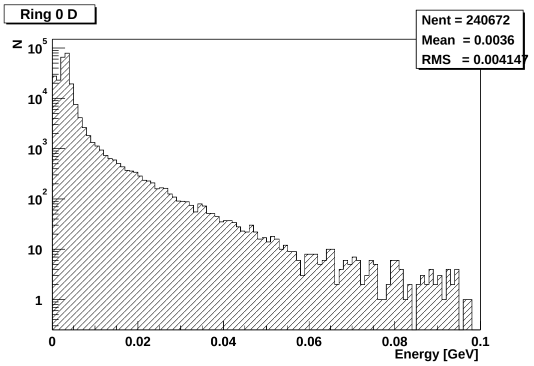

Figure 5.22: Energy deposit in tiles for ring 0 with $\eta \in$ [-1.99;-1.73]. No beam pipe or support.

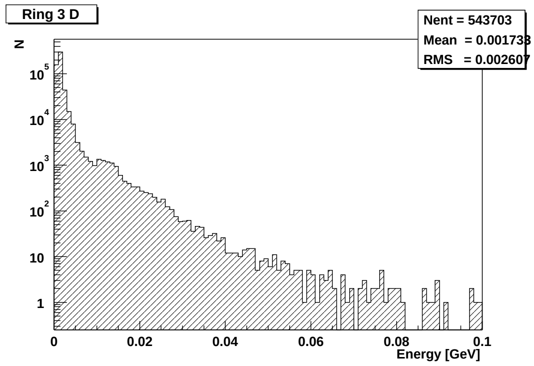

Figure 5.23: Energy deposit in tiles for ring 3 with $\eta \in$ [-0.80;-0.03]. No beam pipe or support.

5.6.7 Simulation without Silicon Detectors, Tile Support or Beam Pipe

To obtain an estimate of the contribution from the silicon detectors, situation E is considered in graphs 5.24 and 5.25.

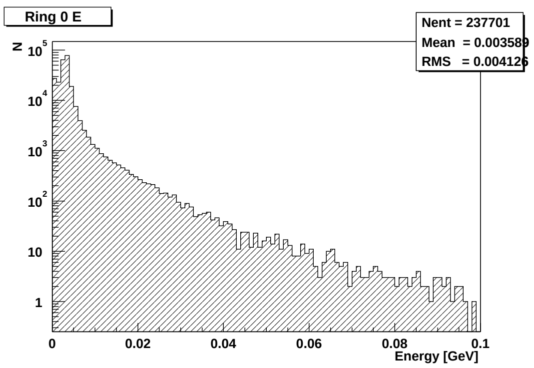

Figure 5.24: Energy deposit in tiles for ring 0 with $\eta \in$ [-1.99;-1.73]. No beam pipe, support or silicon.

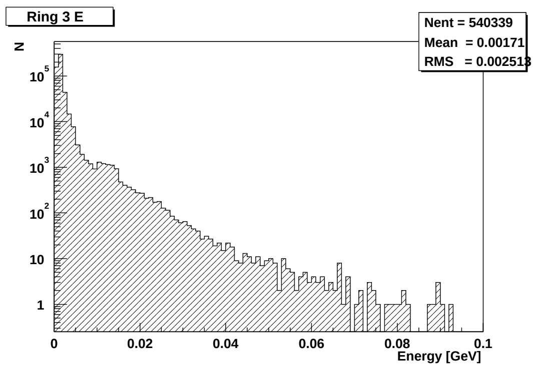

Figure 5.25: Energy deposit in tiles for ring 3 with $\eta \in$ [-0.80;-0.03]. No beam pipe, support or silicon.

The ratio R_s is for situation E ring 0 is 16% and for ring 1, 12%. This is hardly any different than situation D. So the 0.03 cm thick silicon detectors does not contribute significantly to the secondaries.

5.6.8 Simulation without Hadronic Interactions, Tile Support, Silicon Detectors or Beam Pipe

On graph 5.26 and 5.27 all material between collision zone and the tiles have been removed (simulation F) and without hadronic interactions. Again the deviation is calculated and the ratio is 35% for 1F and 30% for 4F. The ratio is similar to simulation B and this show that the largest contributor to the production of secondaries is caused by the hadronic interactions.

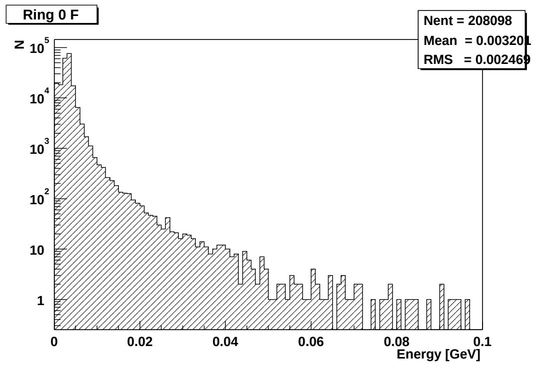

Figure 5.26: Energy deposit in tiles for ring 0 with $\eta \in$ [-1.99;-1.73]. No beam pipe, support, silicon or hadronic interactions.

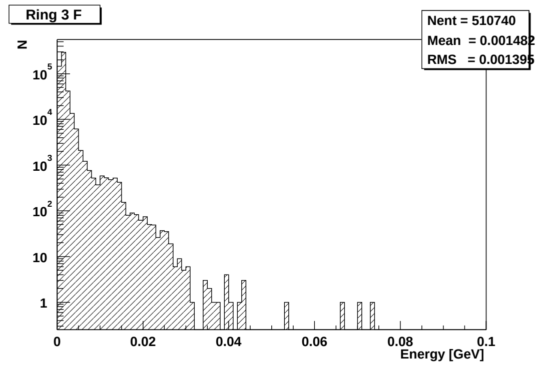

Figure 5.27: Energy deposit in tiles for ring 3 with $\eta \in$ [-0.80;-0.03]. No beam pipe, support, silicon or hadronic interactions.

In the following section the results of all simulations will be discussed and compared with previous obtained measurements.

5.6.9 The Secondaries Ratio

The calculated correction ratios $\frac{N_{sec}}{N_{tot}}$ from BRAG simulations are shown in figure 5.28 and the values are listed in table 5.2. The difference between simulation B and F only differs by the detector elements, which are turned off in the F simulation. These simulations show that the secondaries ratio is $\approx$ 30% at midrapidity and this contribution grows to 35% at η = 2. Similar independent estimates on the secondaries ratio have been made at BNL [81], where the results were fitted with a parabola with the equation

$$f(x) = 0.004\ x^2 + 30 \tag{5.5}$$

where x is the distance from nominal vertex in units of cm. In [81] the primary particles are defined as the ones originating inside the beam pipe and weak decaying particles, while the definition used in this analysis is to virtually remove detector elements and hadronic interactions. Even though the two estimates on secondary particle production ratio is based on different assumptions, they agree well as seen on figure 5.28.

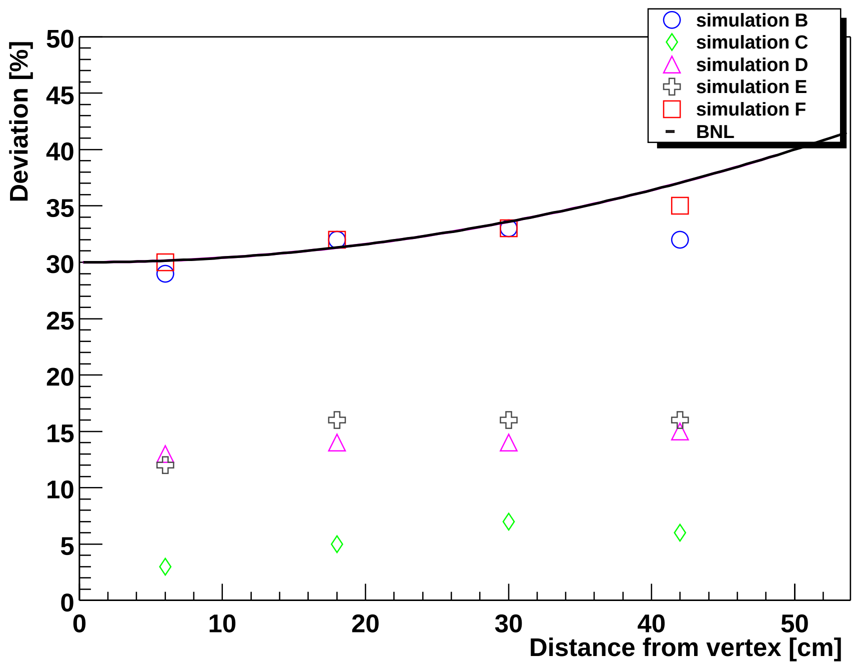

Figure 5.28: Secondaries ratio $\frac{N_{sec}}{N_{tot}}$ for simulations B to F. It is concluded that the simulations B and F agree well with the previous estimates made at Brookhaven National Laboratory [81]. Simulation B included beam pipe, silicon detectors and tile support, but not hadronic interactions. This simulation should be compared with simulation F where the everything was turned off, i.e. beam pipe, silicon detectors, tile support and hadronic interactions were inactive. Simulation C include beam pipe, silicon detectors, and tile support. This simulation show that the beam pipe does not contribute significantly to the production of secondaries. Simulation D includes silicon detectors and hadronic interactions and simulation E just includes hadronic interactions, i.e. beam pipe, silicon detectors and support for the tiles are inactive. The only difference between E and F is the hadronic interactions, which must account for about half of the produced secondaries. Plotted values are listed in table 5.2.

The systematic errors from the simulations are very small ($\ll$1%). The total number of events simulated in this part of the analysis varies from $2{\cdot}10^5$ to $5{\cdot}10^5$ which gives a statistical error of less than 1%.

Having examined the ratio of secondaries based on GEANT simulations, a better understanding of where the secondary particles are generated has been obtained. From the

Ring	η	B	C	D	E	F
0	[-1.99;-1.73]	32	6	15	16	35
1	[-1.72;-1.36]	33	7	14	16	33
2	[-1.35;-0.83]	32	5	14	16	32
3	[-0.80;-0.03]	29	3	13	12	30

Table 5.2: Summary of ratios $\frac{N_{sec}}{N_{tot}}$ in %.

energy deposit distributions throughout section 5.6 the mean and RMS values are noted and will be used in the forthcoming fluctuation analysis. Multiplicities from measured data and BRAG simulated HIJING events have shown to be consistent as a function of η and azimuthal angle (ϕ). The multiplicity generated from BRAG simulated FRITIOF has been shown to be too high, when compared with data and BRAG simulated HIJING events. In the following chapter the analysis will focus on multiplicity fluctuations from measured data and simulations with and without the use of the BRAG simulation program.

Chapter 6

Analysis of Multiplicity Fluctuations

In this chapter the correlation and fluctuation as a function of pseudorapidity is examined. In the previous chapter the centrality cut, the measured and BRAG simulated multiplicities were shown to be consistent. These multiplicities will now be used as basis for the correlation and fluctuation calculations. The correlation and fluctuation is calculated using a statistical module called `BrStatistics`, as mentioned in section 5.2. How this is done is described in the following section.

6.1 Covariance Matrix

The covariance for elements i and j is, for N_{ev} events, is defined as

$$C(x)_{i,j} = \sum_{k=1}^{N_{ev}} (x_{i_k} - \overline{x}_i)(x_{j_k} - \overline{x}_j) \tag{6.1}$$

where

$$\overline{x} = \frac{\sum_{k=1}^{N_{ev}} x_i}{N_{ev}} \tag{6.2}$$

The elements in the sample covariance matrix for the charged particle multiplicities N is then defined as

$$C(N)_{ij} = \sum_{k}^{N_{ev}} \left(N_{ik} - \overline{N}_i\right)\left(N_{jk} - \overline{N}_j\right) \tag{6.3}$$

Using a statistical C++ module as described in [79], the covariance is calculated in the following way. For the first event, the average and covariance is defined as

$$\overline{x_i}^{(1)} = x_{i1} \tag{6.4}$$

and

$$C_{ij}^{(1)} = 0 \tag{6.5}$$

For the following events the average value and covariance are calculated in the following way in order to minimize round off errors.

$$\overline{x_i}^{(n)} = \overline{x_i}^{(n-1)} + \frac{1}{n}\left(x_{in} - \overline{x_i}^{(n-1)}\right) \tag{6.6}$$

and

$$C_{ij}^{(n)} = C_{ij}^{(n-1)} + \frac{1}{n-1}\left[\left(x_{in} - \overline{x_i}^{(n)}\right)\left(x_{jn} - \overline{x_j}^{(n)}\right)\right] - \frac{1}{n}C_{ij}^{(n-1)} \tag{6.7}$$

Having defined the covariance matrix, the correlation matrix can be defined as shown in the next section (6.2).

6.2 Correlation Matrix

Defining the correlation matrix as:

$$corr_{i,j} = \frac{C(N)_{ij}}{\sigma_i \sigma_j} \tag{6.8}$$

where

$$\sigma_i^2 = C_{ii} \tag{6.9}$$

If two stochastic variables satisfy that $corr_{i,j} = 0$, the two variables i and j are said to be uncorrelated. If $corr_{i,j} = 0 \Leftrightarrow C_{i,j} = 0$. Also it can be proven [80] that

$$-1 \leq corr_{i,j} \leq 1 \tag{6.10}$$

Calculating the average multiplicity in each ring of tiles, an 8x8 correlation matrix can be constructed, thus showing the correlations between various rapidity bins.

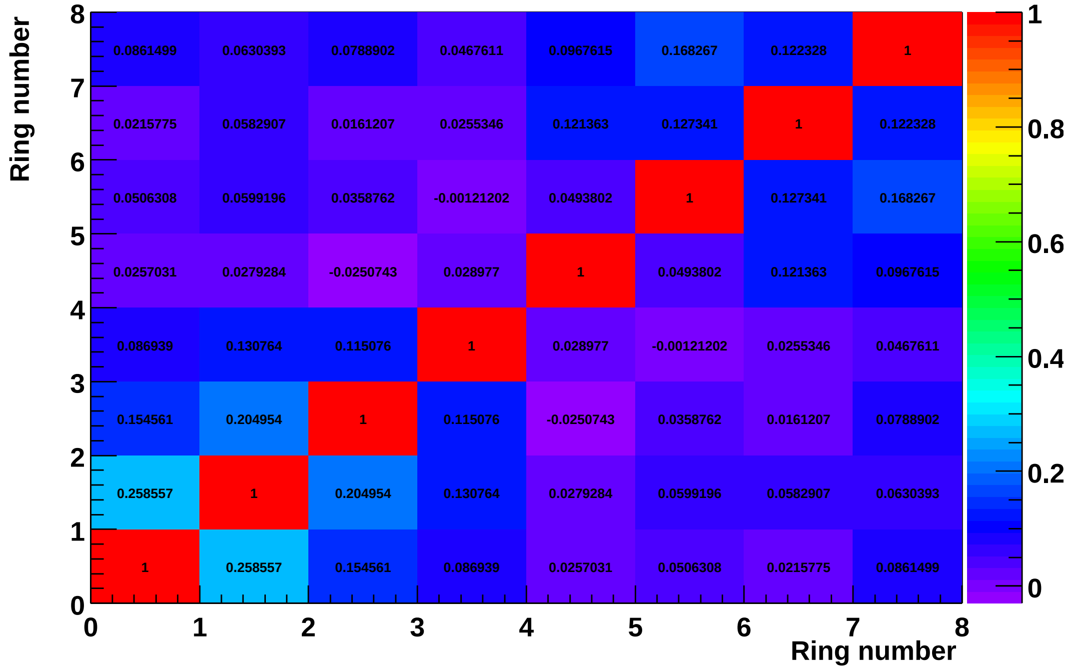

Figure 6.1: Correlation matrix calculated for **data (40-50%)** for the 8 rings (see table 3.1 for corresponding pseudorapidities for the ring numbers). The diagonal elements are 1 as expected and small correlations for the off-diagonal elements are noticed. These correlations seem to decrease, the further the tiles are apart. The anti correlations emerging at midrapidity are within the error interpreted as no correlation.

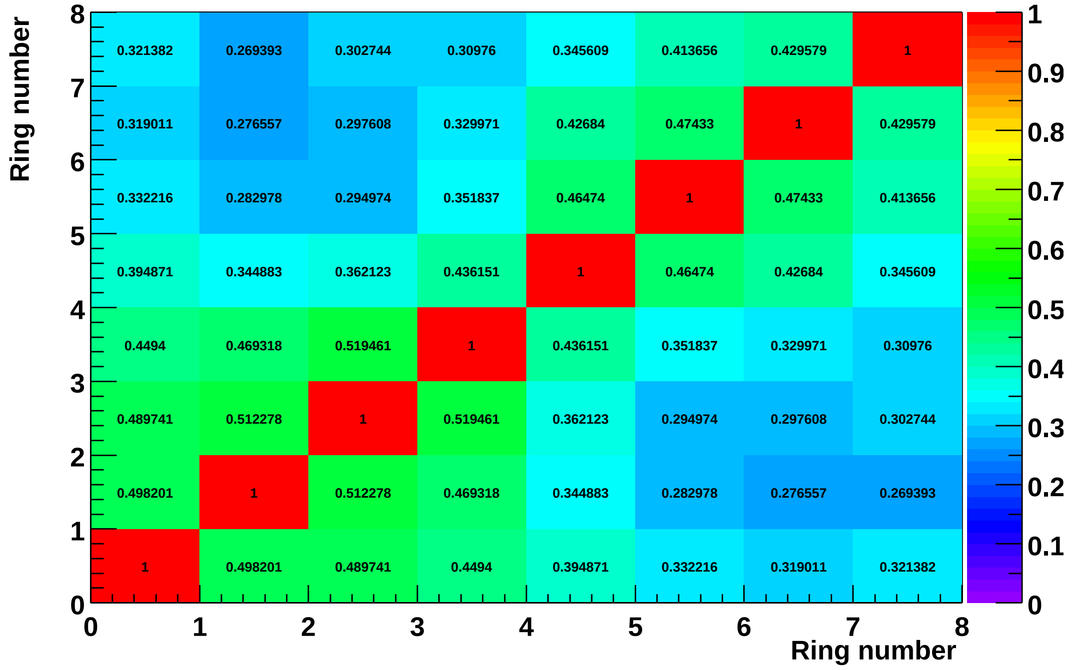

Figure 6.2: Correlation matrix calculated for **data (0-10%)** for the 8 rings, as in figure 6.1. The entire level of correlations has now been elevated due to the larger particle production in central events. The decrease of correlations between tile elements, as they move apart is now more evident.

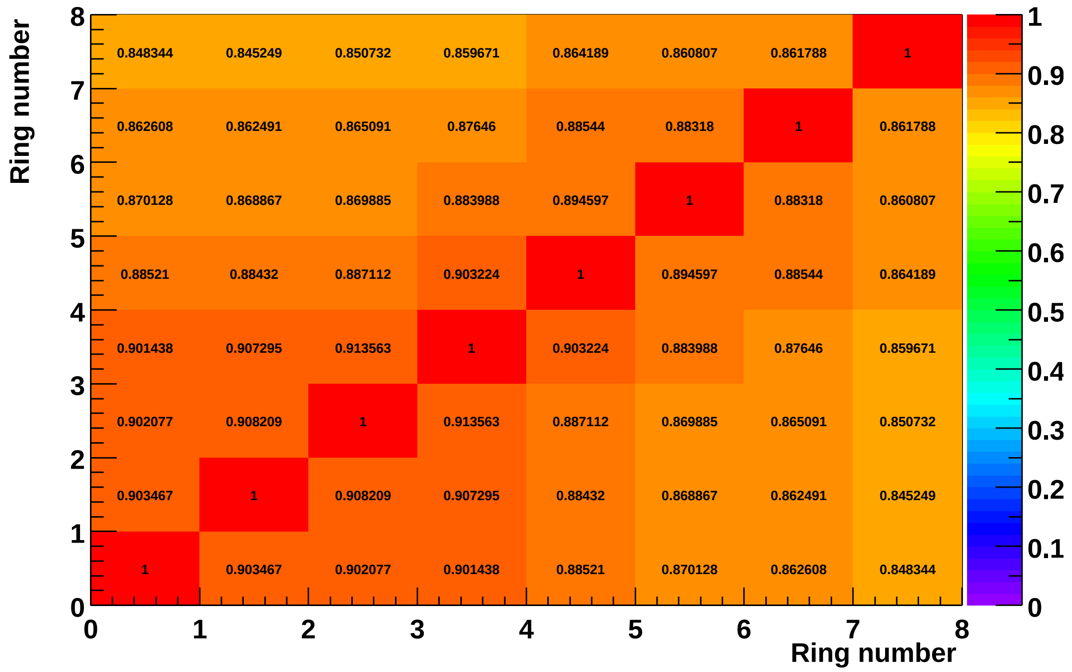

Figure 6.3: Correlation matrix calculated for multiplicities for the 8 rings (see table 3.1 for corresponding pseudorapidities for the ring numbers). The centrality cut is from 0 to 50% most central events.

Figures 6.1, 6.2 and 6.3 obviously show that the diagonal elements are 1 for the correlation matrix, i.e. the rings are totally correlated with themselves, which is expected. Next, it can be concluded that two tiles in general are correlated and that the correlation decreases, the further the tiles are apart. In a peripheral (see figure 6.4) collision (40-50% centrality) only relatively few particles are produced, and therefore only small correlations are detected for the off-diagonal elements, as in figure 6.1. More particles are produced per collision in central events (0-10%) and therefore the correlation matrix (figure 6.2), show a higher level of correlations between the rings. This could be caused by collective effects such as *flow*, which STAR has detected in [83]. Figure 6.3 contains correlation information from different sources, which results in the large correlations in the off-diagonal elements, when compared to 6.1 and 6.2. In general it can be concluded that the impact parameter plays a large role for at fluctuations and one has to correct for that. Also it is concluded that there some correlation between η bins and therefore the fluctuation analysis should be done as a function of pseudorapidity.

6.3 The ω Matrix

In the previous section, the correlation matrix was normalized to 1. In a fluctuation analysis, the magnitude of the fluctuation is of interest and will be calculated in this

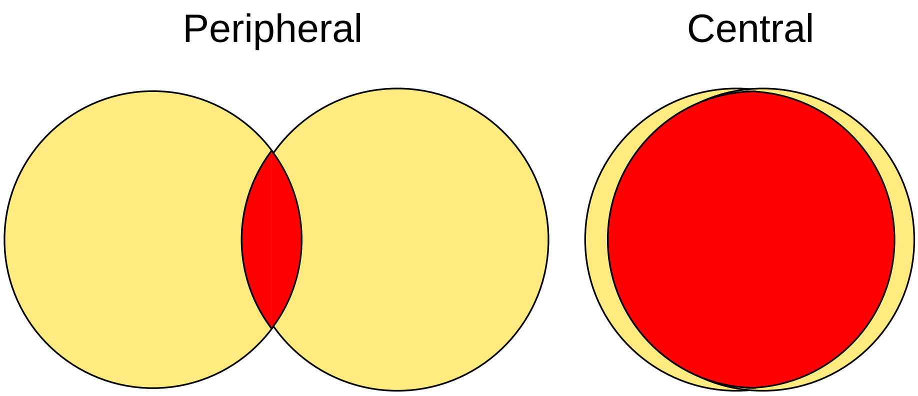

Figure 6.4: Peripheral and central collisions viewed along beam axis. The red area indicates the participant zone.

section. The fluctuation is calculated using the definition from section 2.7.1 where the fluctuations between the (i,j)th element be defined as

$$\omega_{N_{ij}} \equiv \frac{\overline{N_i N_j} - \overline{N_i}\ \overline{N_j}}{\sqrt{\overline{N_i}\ \overline{N_j}}} \tag{6.11}$$

Choosing a row of tiles, the fluctuation is now calculated for that row and shown in figures 6.6 and 6.7 for respectively 0 to 10% and 0 to 50% centrality cuts. In figure 6.6 the fluctuation for the diagonal elements ($i = j$) are relatively larger, than compared to off-diagonal elements ($i \neq j$). The largest fluctuation is seen for the diagonal elements corresponding to tiles located close to maximum multiplicity, i.e. at midrapidity. By comparing the two figures, corresponding to different cuts in centrality, the fluctuation dependence on centrality is clearly seen. The large fluctuations is caused by the nominator in equation 6.11 which is just an expression of the width of the distribution. The centrality cut determines the shape of the distribution.

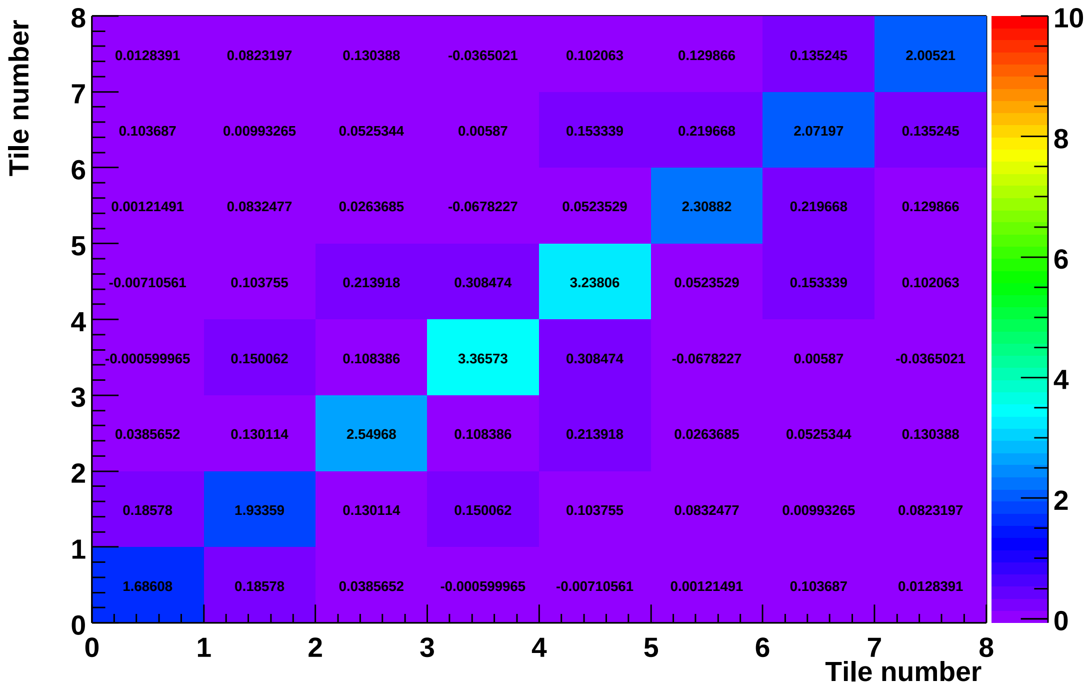

Figure 6.5: Fluctuation matrix for data (40-50%) for a tile row (tile number 0 to 7 - see table 3.1 for corresponding pseudorapidities, since the tile number for first row equals the ring number.). The diagonal elements clearly show larger fluctuations, than the off-diagonal elements, which is also expected when comparing to figure 6.1 (see table 3.1 for corresponding pseudorapidities).

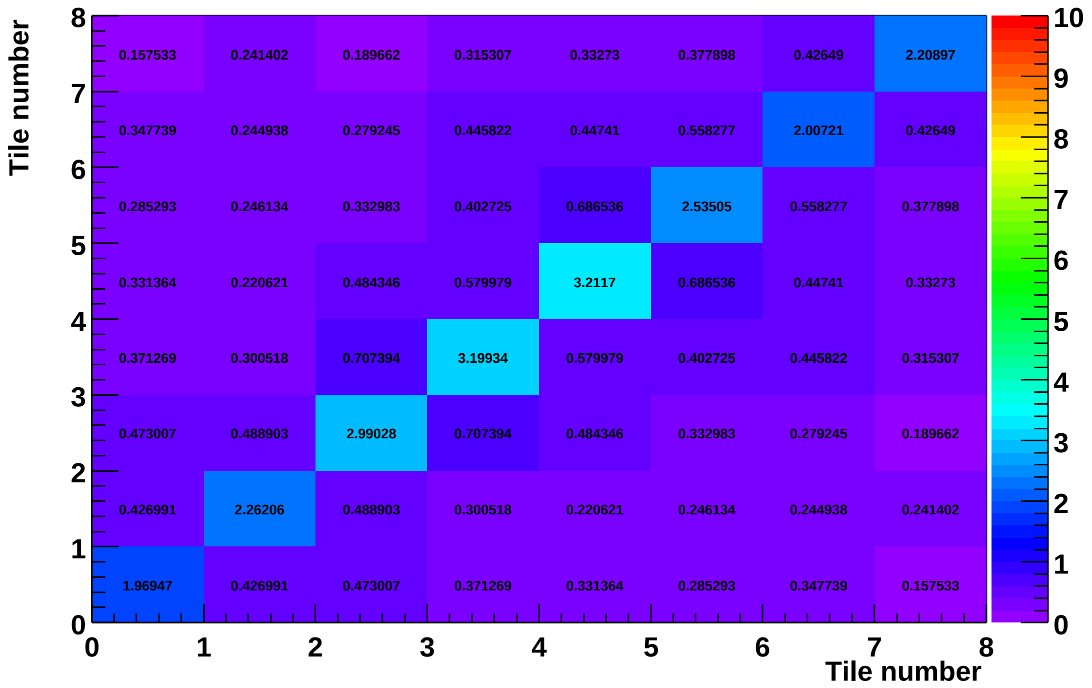

Figure 6.6: Fluctuation matrix for 0 to 10% central events plotted in the same way as figure 6.5. Again larger fluctuations for the diagonal elements. The level of the off diagonal elements is lifted, for the same reasons as in figure 6.2.

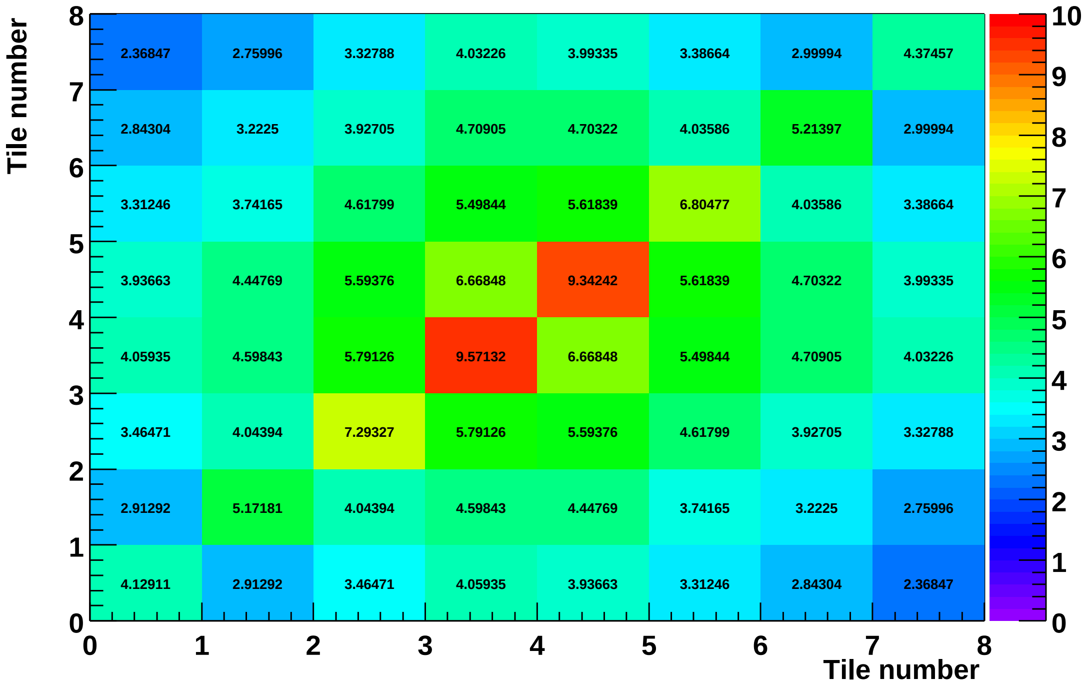

Figure 6.7: Fluctuation matrix for 0 to 50% central events plotted in the same way as figure 6.5. The total level of the ω values are higher for this wide centrality cut due to impact parameter fluctuations. Also the correlation between elements is relatively larger for the broad mix of centralities as compared to the narrow centrality cut in figure 6.6.

The increase in fluctuations observed towards midrapidity and for more central collisions is due to several *trivial* effects in addition to possible increased fluctuations due to the physics of the source. The *trivial* effects are: Impact parameter fluctuations, fluctuations from energy loss distributions of particle, due to varying momentum (ω_{slow}), fluctuations due to the production of secondaries (ω_{sec}). In chapter 7 these fluctuation contributions will be examined.

Before calculating the fluctuations as a function of η, the statistical and systematic error on ω are defined.

6.4 Statistical Error

The statistical error on the average multiplicity (N) over N_{ev} events is evaluated as

$$\sigma_N^2 = \frac{\overline{N^2} - \overline{N}^2}{N_{ev}} \tag{6.12}$$

The statistical error on the fluctuations is derived in appendix C and is given in equation 6.13, where N_{ev} denotes the number of events.

$$\sigma_\omega^2 = \frac{4\omega^2}{N_{ev}} \tag{6.13}$$

6.5 Systematic Error

A systematic error is caused by any factors that systematically affect the measurement of the variable across the sample. The systematic error on the multiplicity from the employed data analysis procedures is estimated to be $\approx 5\%$ [31]. This is mainly due to the scatter of single particle response measurements of a tile and uncertainty from GEANT simulations.

The systematic error on ω is assumed to be the same as for the multiplicity, from the following simple consideration. Let α be the systematic error on the multiplicity, the error on ω is then

$$\omega_N = \frac{\overline{(\alpha N)^2} - \overline{\alpha N}^2}{\overline{\alpha N}} = \frac{\alpha^2\overline{N^2} - \alpha^2\overline{N}^2}{\alpha\overline{N}} = \alpha\,\frac{\overline{N^2} - \overline{N}^2}{\overline{N}} \tag{6.14}$$

6.6 Fluctuations as a function of η

Fluctuation calculations as a function of η are shown in figure 6.8 for data and BRAG simulated HIJING events for peripheral (0 to 50%) and central events (0 to 10%). The upper panels show fluctuations for data and lower for simulated HIJING events. The left show fluctuations for central events and the right panels for peripheral events. The graphs show an overall good consistency for the rows as a function of pseudorapidity. The points align better for the central events because of the better statistics.

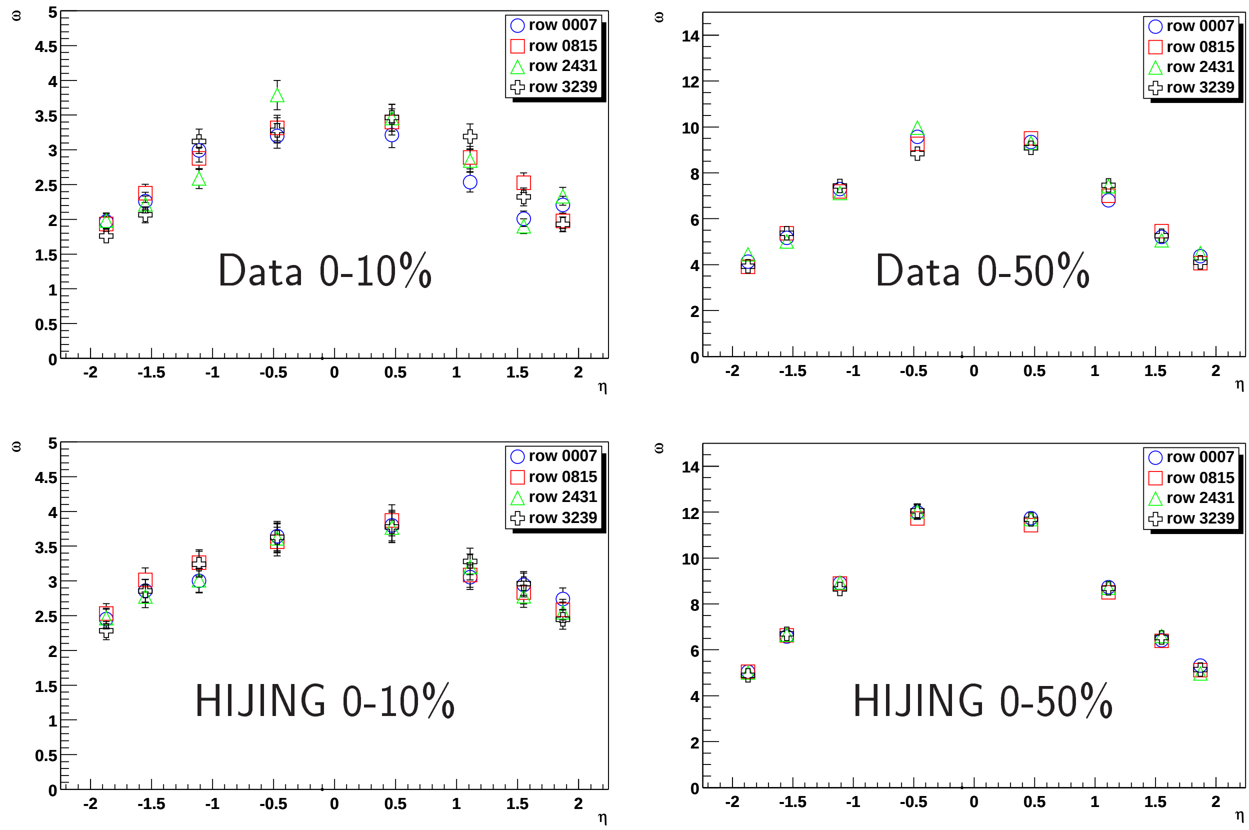

Figure 6.8: Fluctuations as a function of η for data and BRAG simulated HIJING events. The upper left plot show fluctuations for data with a centrality cut from 0 to 10%. The upper right the same for data with a centrality cut from 0 to 50%. The lower left and right plot show simulated HIJING events with a centrality cuts from 0 to 10% and 0 to 50%, respectively. The 0-10% points are based on about 1.200 events and the 0-50% on approximately 6.000 events. Statistical error (defined in section 6.4) is showed where larger than symbol size.

6.7 Fluctuations as a function of ϕ

The multiplicity has been shown to be constant as a function of azimuthal angle (ϕ) in figure 5.10. For many events one would expect the same behavior for $\overline{N^2} - \overline{N}^2$, and also for ω. In the following fluctuations are analyzed with a centrality cut from 0 to 10% for data (figure 6.9) and BRAG simulated HIJING events (figure 6.10). In order to compare, these two, similar plots for 0 to 50% central events are plotted in figure 6.11 for data and in figure 6.12 for BRAG simulated HIJING events. From the plots it is concluded that the fluctuations vs. ϕ are constant, as expected. It is also noted that the figures showing centrality ranges from 0 to 50% are closer aligned, because of a factor of 5 more statistics, that the 0 to 10% central events.

On the following 4 figures, zero degree polynomials have been fitted to all rings, but are not shown in figure. The fit parameters and χ^2/ndf are instead listed in the tables below figures.

In this chapter it has now been shown that the fluctuations are constant as a function of η and ϕ. Fluctuations in measured BRAHMS data have been shown to be consistent with BRAG simulated HIJING events. The measured fluctuations in this section are influenced by fluctuation contributions from impact parameter, secondary particle production and from slow particles. The remaining work in analysis is to estimate these contributions, in order to determine the *intrinsic* fluctuations, i.e. the fluctuations that are not influenced by our measurement.

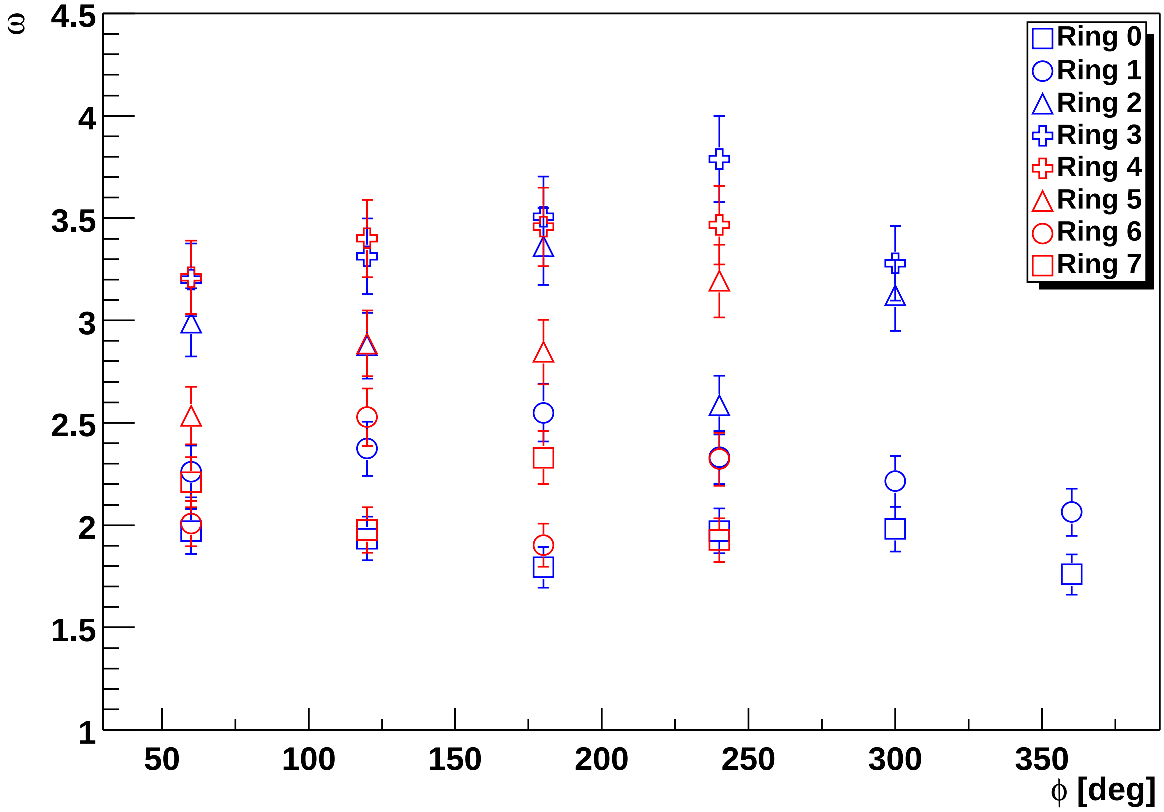

Ring	p0	χ^2/ndf
0	1.90±0.04	4.9/5
1	2.31±0.05	8.0/5
2	2.98±0.04	10.7/4
3	3.45±0.09	4.9/5
4	3.41±0.10	0.89/3
5	2.85±0.08	11.0/3
6	2.16±0.06	15.9/3
7	2.14±0.06	9.3/3

Figure 6.9: Fluctuations for data for all rings vs. azimuthal angle for 0 to 10% central events. The error bars are statistical and are described in section 6.4. Zero degree polynomial has been fitted to all rings. Fits are not shown on figure, but fit parameter and χ^2/ndf are listed in table below the figure.

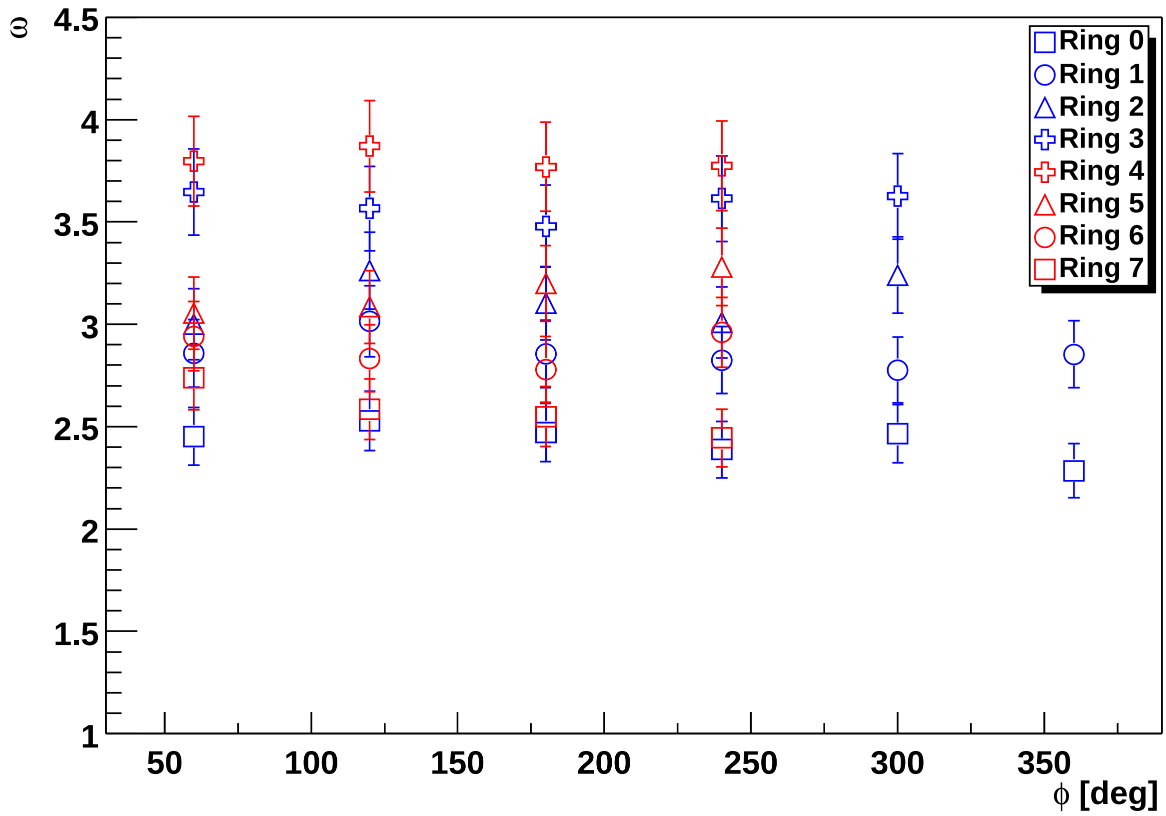

Ring	p0	χ^2/ndf
0	2.43±0.06	1.9/5
1	2.86±0.07	1.1/5
2	3.12±0.08	1.9/4
3	3.58±0.09	0.4/4
4	3.80±0.11	0.1/3
5	3.15±0.09	1.0/3
6	2.88±0.08	0.8/3
7	2.57±0.07	2.0/3

Figure 6.10: Fluctuations shown for simulated HIJING events for all rings as a function of azimuthal angle for 0 to 10% central events. The error bars are statistical and are described in section 6.4. Again a zero degree polynomial has been fitted to all rings. Fits are not shown on figure, but fit parameters are listed in table below figure.

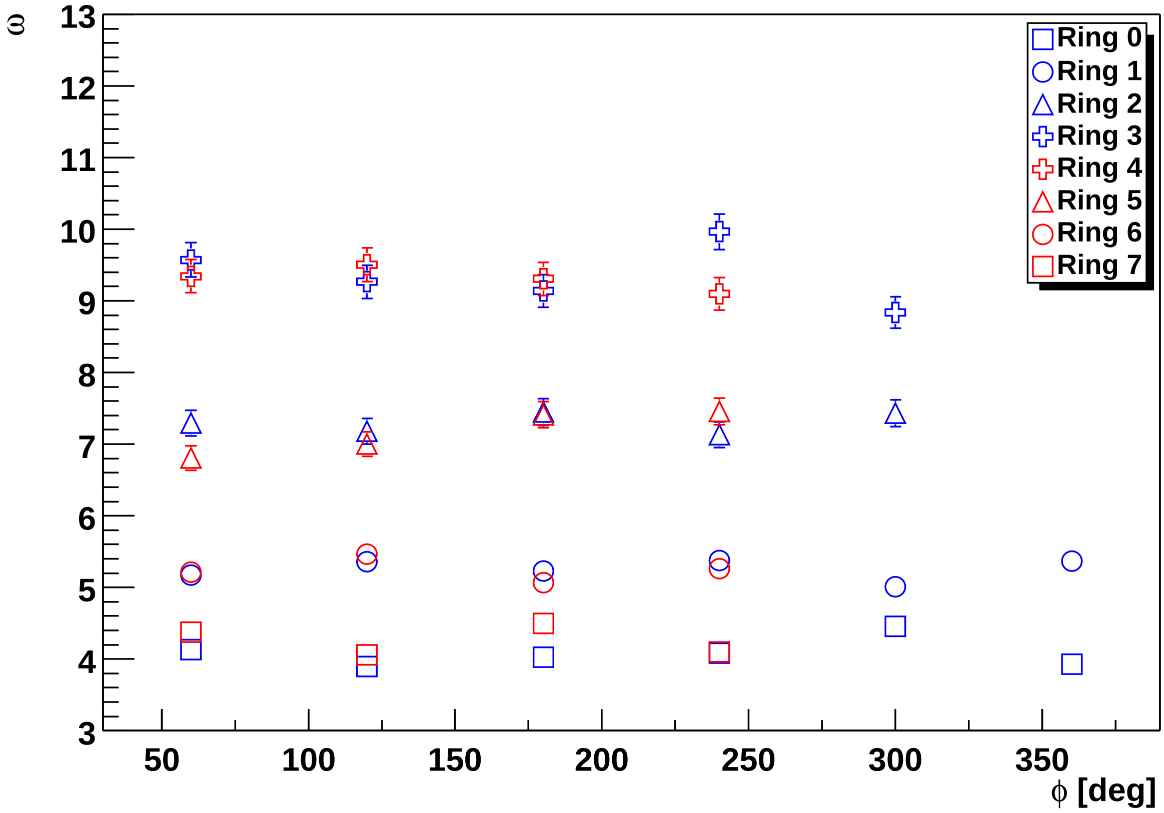

Ring	p0	χ^2/ndf
0	4.06±0.04	15/5
1	5.25±0.06	7.1/5
2	7.30±0.08	2.4/4
3	9.32±0.11	13.7/4
4	9.29±0.12	1.6/3
5	7.18±0.09	12.4/3
6	5.25±0.07	5.7/3
7	4.26±0.05	14.5/3

Figure 6.11: Fluctuations shown for data for all rings as a function of azimuthal angle for 0 to 50% central events. The error bars are statistical and are described in section 6.4. Again a zero degree polynomial has been fitted to all rings. Fits are not shown on figure, but fit parameters are listed in the table below figure.

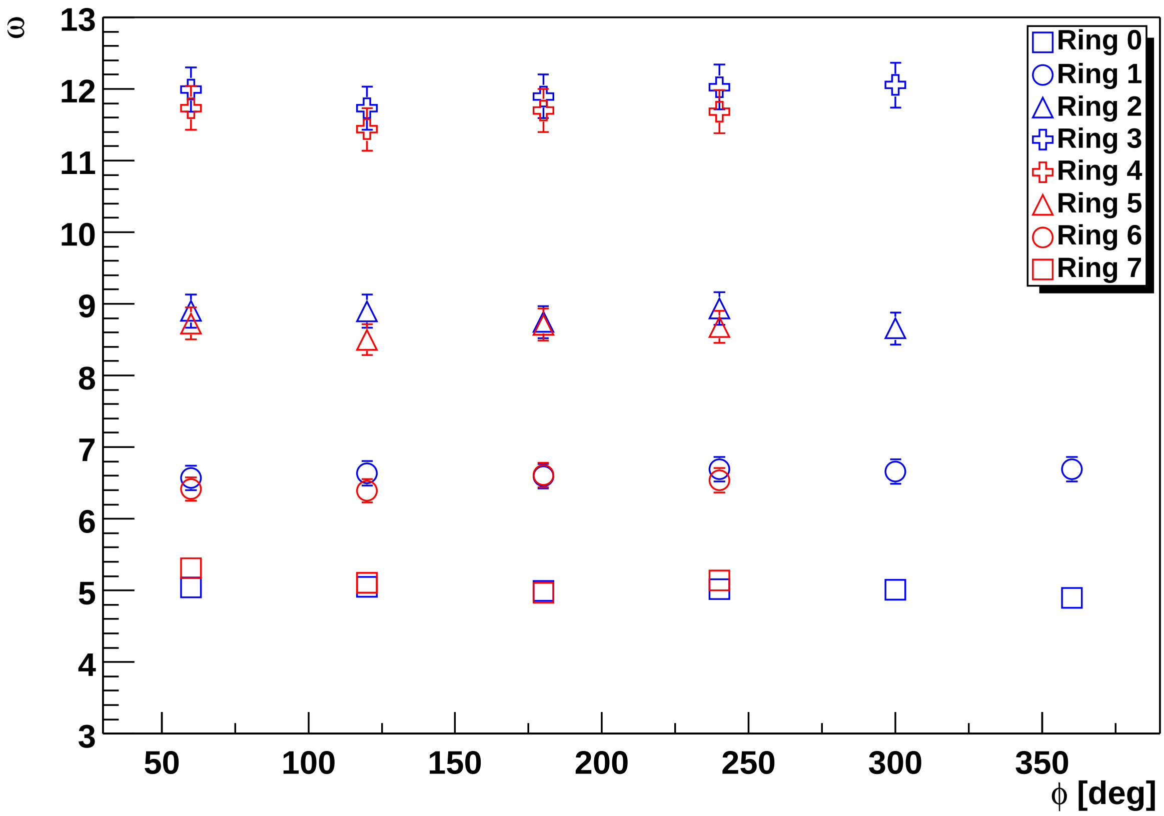

Ring	p0	χ^2/ndf
0	5.00±0.05	1.0/5
1	6.64±0.07	0.4/5
2	8.82±0.10	1.1/4
3	11.94±0.14	0.7/4
4	11.64±0.15	0.6/3
5	8.65±0.11	0.7/3
6	6.49±0.08	1.1/3
7	5.12±0.07	3.4/3

Figure 6.12: Fluctuations shown for simulated HIJING events for all rings as a function of azimuthal angle for 0 to 50% central events. The error bars are statistical and are described in section 6.4. Again a zero degree polynomial has been fitted to all rings. Fits are not shown on figure, but fit parameters are listed in the table below figure.

Chapter 7

Estimating Intrinsic Fluctuations

The aim of the analysis presented in this chapter is to estimate the intrinsic fluctuations, i.e. the fluctuations in the number of produced particles. This is done by estimating the contributions from impact parameter fluctuations, secondary particle production and slow particles to the overall fluctuations. In evaluating the impact parameter fluctuations, the approach is to assume the participant model, which will be described in the following. Fluctuations from secondary particle production and slow particles are estimated using two separate methods. The first is to use the results obtained by feeding event generator data into the BRAG detector simulation and turning the production of secondaries *off*, as described in section 5.6. The other method is to use HIJING events as input to BRAG. These events are not influenced by secondary particle production or by slower particles which may deposit more energy in a tile than a minimum ionizing particle.

7.1 Evaluating Impact Parameter Fluctuations

Evaluating the fluctuations in the participant model should apply well for peripheral collisions because of the relatively low number of produced particles and the low probability of rescattering. In central collisions the number of nucleon-nucleon scatterings and scattering between produced particles increases. Other effects such as resonances can also influence particle production [84]. Assuming the participant model will tend to underestimate the multiplicity. It is not *a priori* obvious that the *participant model* is applicable for central collisions at RHIC. This will be examined in present chapter.

In the *participant model* it is assumed that the multiplicity N arises from N_p independent sources, as shown in figure 7.1.

In this model, the total multiplicity for a given event is

$$N = \sum_{i=1}^{N_p} n_i \tag{7.1}$$

Assuming that there are no correlations between N_p and n, the average multiplicity is therefore

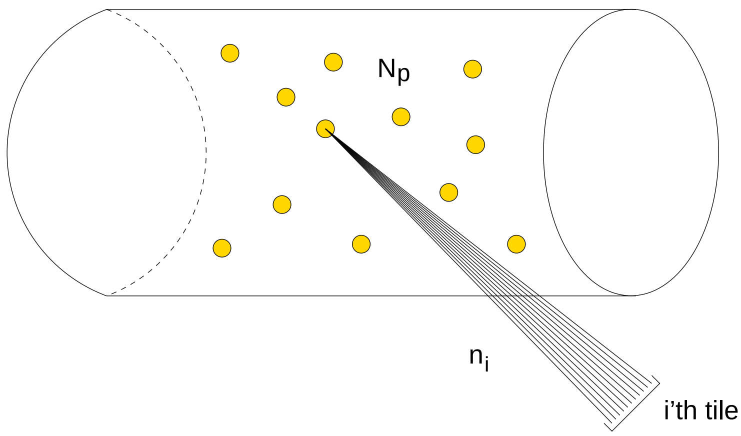

Figure 7.1: Particles are created from N_p independent sources. From each participant n_i particles are emitted, when defining a participant as any source emitting particles.

$$\overline{N} = \overline{N_p} \cdot \overline{n} \tag{7.2}$$

Assuming that particles are emitted independently, i. e. $\overline{n_i n_j} = \overline{n_i} \cdot \overline{n_j}$ for $i \neq j$, we have

$$\omega_N = \frac{\overline{N^2} - \overline{N}^2}{\overline{N}} = \omega_n + \overline{n} \cdot \omega_{N_p} \tag{7.3}$$

where ω_n is the intrinsic fluctuation in the number of particles and ω_{N_p} the fluctuation in the number of sources. The latter is in principle a trivial geometrical quantity. The intrinsic fluctuations may be expected to provide evidence of new physics. For purely statistical (Poissonian) fluctuations in the number of particles, $\omega_n = 1$.

Equation 7.3, which is derived in appendix D, indicates that if the participant model is valid, the observed fluctuation should increase linearly as a function of multiplicity. The intercept of ω_N for the different centrality bins is expected to represent a measure of the intrinsic multiplicity fluctuation. The slope is a measure of the fluctuation in the number of sources and is purely dependent on centrality, since the second term in equation 7.3 is

$$\overline{n} \cdot \omega_{N_p} = \overline{N} \cdot \frac{\omega_{N_p}}{\overline{N}_p} \tag{7.4}$$

Having shown in chapter 5 that the multiplicities and fluctuations are consistent as a function of η and ϕ for the various tiles, the multiplicities from the 4 fully implemented tile rows with same η are now added on an event-by-event basis and the corresponding fluctuations are calculated.

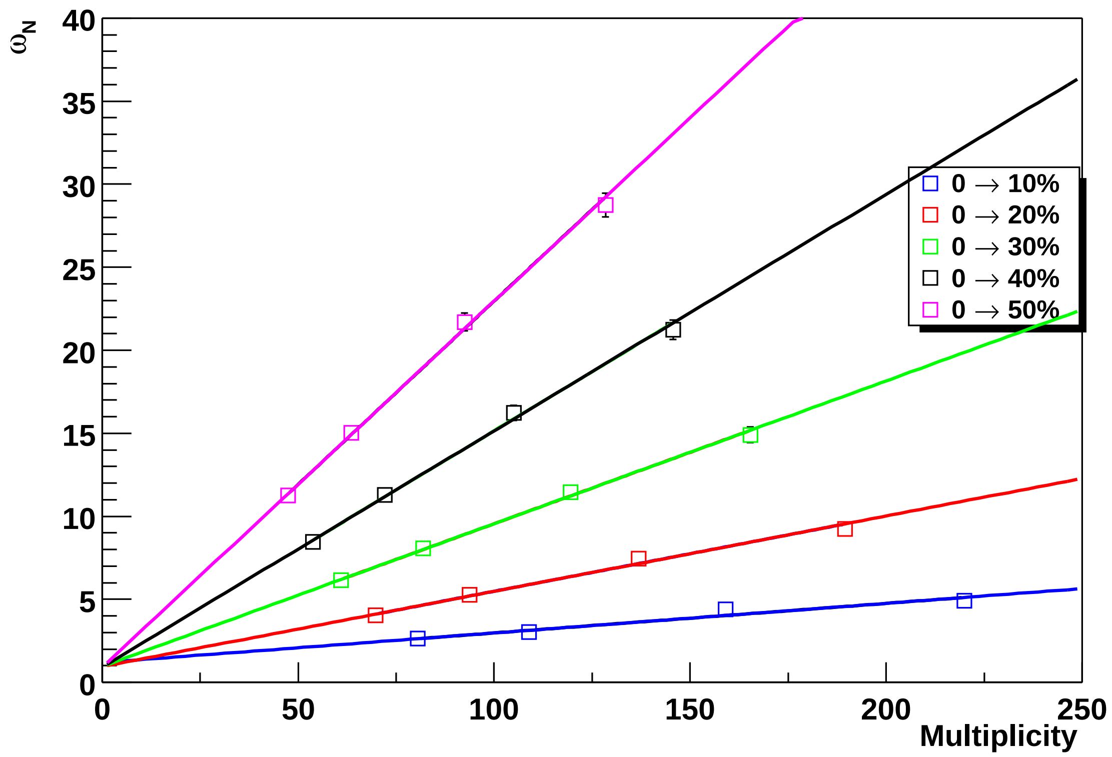

	ω_n	$\omega_{N_p}/\overline{N}_p$	χ^2/ndf
0→10%	1.19 ±0.27	0.018 ± 0.002	3.1/2
0→20%	0.95 ±0.31	0.045 ± 0.003	2.1/2
0→30%	0.95 ±0.39	0.086 ± 0.004	0.8/2
0→40%	0.91 ±0.48	0.142 ± 0.006	1.4/2
0→50%	0.90 ±0.57	0.221 ± 0.008	1.3/2
Average	0.98 ±0.42		

Figure 7.2: Fluctuations vs. multiplicity for **data** with **inclusive** centrality bins, i.e. 0-10%, 0-20%, 0-30%, 0-40% and 0-50%. The multiplicity is the sum of 4 average multiplicities from same η bin (ring). Error bars (shown where larger than symbol size) are statistical and the fit parameters are listed in the table below figure. The estimates on ω_n is about 1 even though the uncertainty of the fit increases with centrality. There is an overall systematic uncertainty on all ω_n values, which is equal to the systematic uncertainty on the multiplicity (see equation 6.5).

Figure 7.2 shows distribution of total fluctuations (ω_N) as a function of the sum of multiplicities in the first 4 rings. Thus, the point with the lowest multiplicity (for each centrality selection) is the sum of multiplicities in tiles 0, 8, 24 and 32 corresponding $\eta \in [-1.99; -1.87]$. The next point is the average multiplicity sum from tiles 1, 9, 25, 33 corresponding to $\eta \in [-1.72; -1.36]$. The third and fourth points are similarly the multiplicity sum from tiles 2, 10, 26, 34 ($\eta \in [-1.35; -0.83]$) and 3, 11, 27, 35 ($\eta \in [-0.80; -0.03]$), respectively. The fluctuations in figure 7.2 are plotted for five different inclusive centrality bins, namely from 0 to 10%, 20%, 30% 40% and 50%, respectively. The points are fitted with straight lines and the fit parameters are listed in the table below the figure. It is noted that all fits intercept the ω_N axis at the value $\omega_n = 1$. The slope of the fit ($\omega_{N_p}/\overline{N}_p$) increases with centrality, indicating larger impact parameter fluctuations. The corresponding figure simulated HIJING events processed by the BRAG detector simulation is shown in figure 7.3. The estimates of ω_n decrease with centrality from 2.11 for the most central events to 0.39 for the most peripheral. Within errors the points are consistent with a fluctuation value of $\omega_n \simeq 1$.

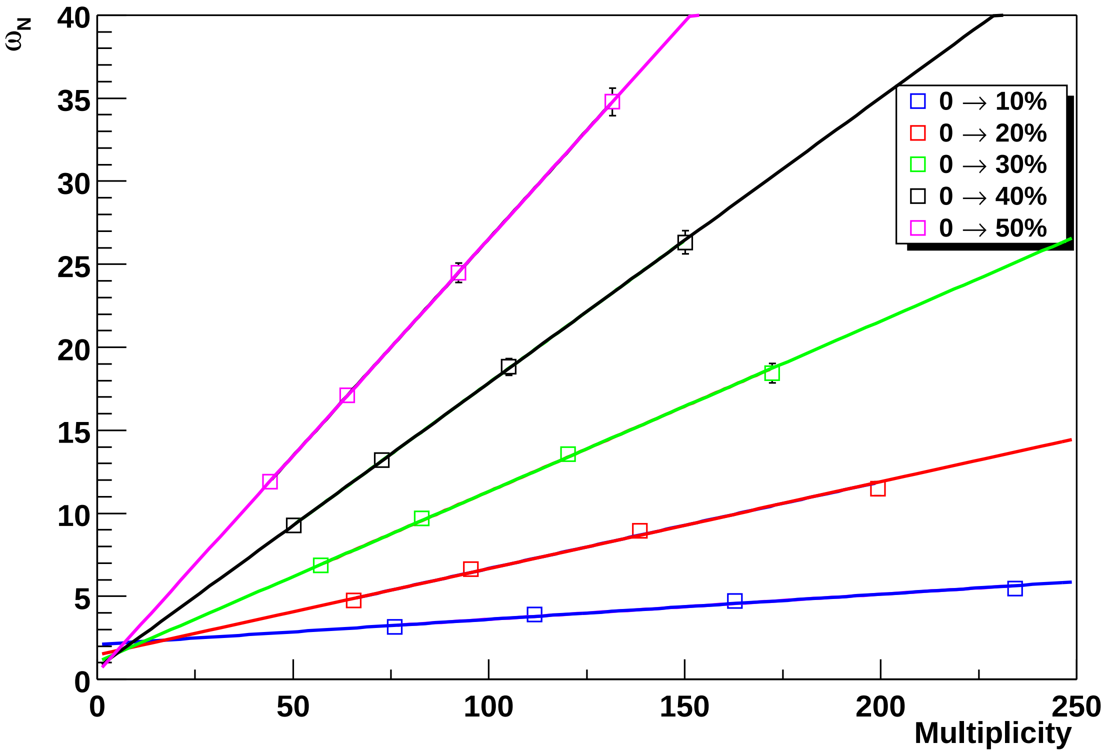

	ω_n	$\omega_{N_p}/\overline{N}_p$	χ^2/ndf
0→10%	2.11 ±0.27	0.015 ± 0.002	1.4/2
0→20%	1.46 ±0.33	0.052 ± 0.003	2.4/2
0→30%	1.06 ±0.40	0.102 ± 0.004	0.7/2
0→40%	0.68 ±0.48	0.172 ± 0.006	0.1/2
0→50%	0.39 ±0.57	0.262 ± 0.009	0.008/2
Average	1.14 ±0.42		

Figure 7.3: Fluctuations for BRAG simulated **HIJING** events with **inclusive** centrality bins. Statistical error bars are shown where larger than symbol size and the fit parameters are listed in the table below figure. The fitted values for ω_n decreases with increasing centrality. But the value is consistent with 1.

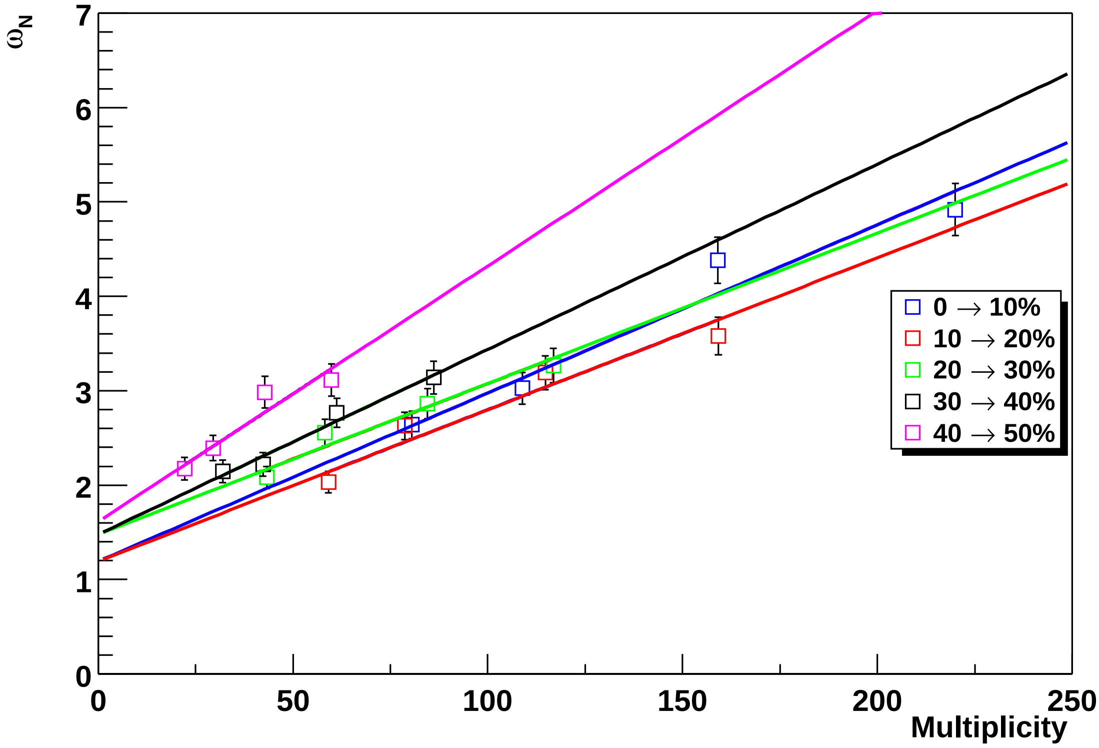

	ω_n	$\omega_{N_p}/\overline{N}_p$	χ^2/ndf
0 →10%	1.19 ±0.27	0.018 ± 0.002	3.1/2
10→20%	1.19 ±0.20	0.016 ± 0.002	3.8/2
20→30%	1.48 ±0.20	0.016 ± 0.003	1.9/2
30→40%	1.48 ±0.19	0.020 ± 0.004	0.9/2
40→50%	1.61 ±0.20	0.027 ± 0.005	2.3/2
Average	1.39 ±0.21		

Figure 7.4: Fluctuations for **data** with **exclusive** centrality bins. Error bars are statistical and the fit parameters are listed in the table below the figure. It is noticed that the exclusive bins are consistent, within errors, with the inclusive bins in figure 7.2.

Figures 7.4 and 7.5 show fluctuations vs. average multiplicity. They are similar to figures 7.2 and 7.3 but the centrality bins are now exclusive, i. e. 0 to 10%, 10% to 20% etc. Within the uncertainty all curves point back to the same intercept validating the assumptions of equation 7.3. There is however a difference between intercepts from data and from the HIJING simulation. The BRAG simulated HIJING events are $\omega_n \simeq 2.2$, whereas the data predict $\omega_n \simeq 1.4$. The slopes for each centrality are equal within the error, except for the most peripheral events (40-50%). A small increase in the fitted slopes is also noticed.

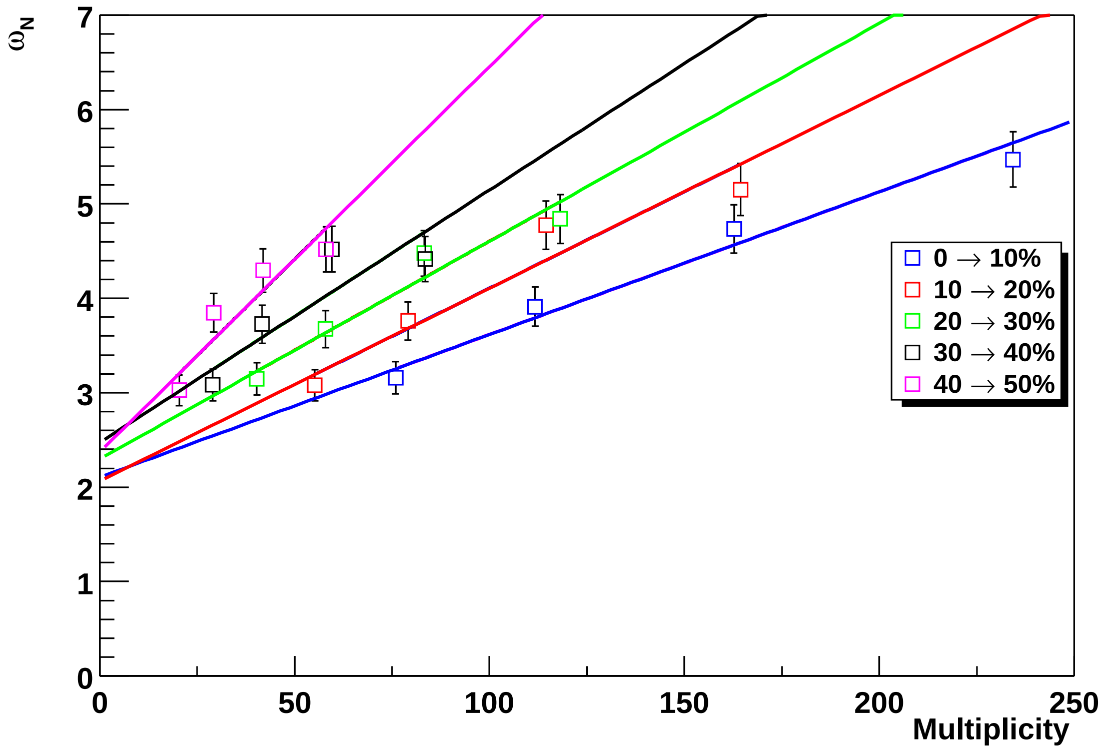

	ω_n	$\omega_{N_p}/\overline{N}_p$	χ^2/ndf
0 →10%	2.11 ±0.27	0.015 ± 0.002	1.4/2
10→20%	2.01 ±0.27	0.020 ± 0.003	3.7/2
20→30%	2.30 ±0.27	0.023 ± 0.004	1.9/2
30→40%	2.47 ±0.26	0.027 ± 0.005	6.4/2
40→50%	2.37 ±0.26	0.041 ± 0.007	4.8/2
Average	2.25 ±0.20		

Figure 7.5: Fluctuations for simulated **HIJING** events using **exclusive** centrality bins. The fit values for ω_n are now within the statistical error equal, which was not the case for the inclusive centrality bins in figure 7.3. Fit parameters are listed in the table below figure. An even better consistency

The effect of the vertex acceptance on the results has been investigated by changing the vertex opening from the initial $|z| \leq 2.5$ cm to the double and half the width, and thereafter repeating the analysis. The corresponding figures are shown in appendix E. The analysis shows that accepting vertices with $|z| \leq 1.25$ cm (figure E.1) does not change the estimated value of ω_n. An opening of the vertex to $|z| \leq 5.00$ cm (shown in figure E.2) does not, within the errors, show any systematic dependence between $|z| \leq 2.5$ cm and $|z| \leq 5.0$ cm.

It is interesting to investigate if the procedure of processing the event data from HI-

JING in the BRAG detector simulation causes some additional fluctuations. The way to determine this contribution is by examining a *raw* HIJING event and comparing this to a detector simulated (BRAG) file. The procedure has been to define virtual tiles in space with dimensions equal to the actual tiles and repeat the analysis to determine if there is a difference. In this analysis only pions, kaons and protons are used. The centrality cut is made in the charged particle distribution of pions, kaons and protons within the pseudorapidity range of $|\eta| \geq 2$. Figures 7.6 and 7.7 show the estimated intrinsic fluctuations for HIJING events without using BRAG for inclusive and exclusive centrality bins, respectively. These figures should be compared to figures 7.2 and 7.4.

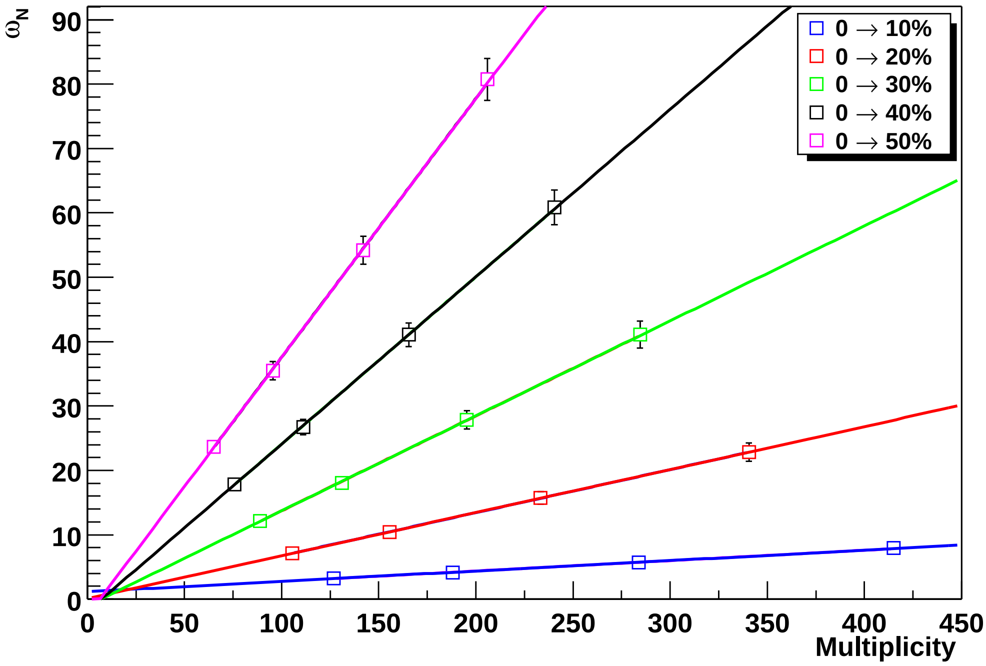

	ω_n	$\omega_{N_p}/\overline{N}_p$	χ^2/ndf
0 →10%	1.15 ±0.49	0.016 ±0.002	0.1/2
0 →20%	0.07 ±0.86	0.067 ±0.005	0.03/2
0 →30%	-1.03 ±1.24	0.147 ±0.009	0.06/2
0 →40%	-1.91 ±1.59	0.260 ±0.014	0.06/2
0 →50%	-2.59 ±1.89	0.402 ±0.020	0.1/2
Average	-0.86 ±1.31		

Figure 7.6: Fluctuations **without using BRAG for inclusive** centrality bins. The value of ω_n varies from 1.15 to -2.59. The corresponding statistical errors are also larger than seen in figures 7.2 and 7.3. It has not been possible to find any reason for these large errors. Note the relatively larger average multiplicity, than when compared to figure 7.3 and hence the larger scale on the figure.

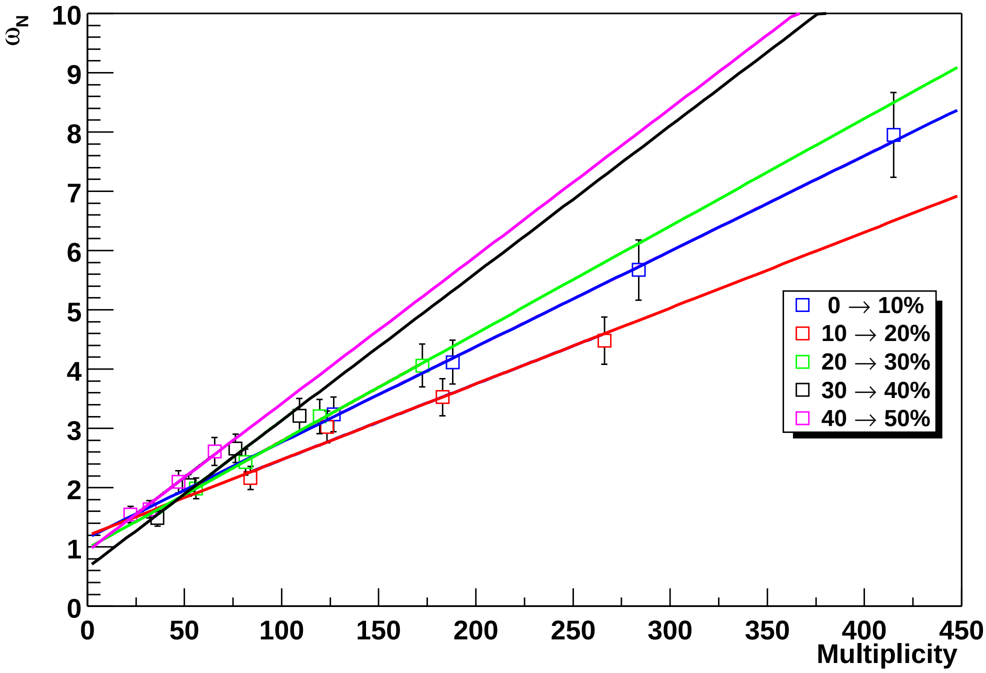

	ω_n	$\omega_{N_p}/\overline{N}_p$	χ^2/ndf
0 →10%	1.15 ±0.49	0.016 ± 0.002	0.1/2
10 →20%	1.19 ±0.32	0.013 ± 0.013	1.2/2
20 →30%	0.97 ±0.30	0.018 ± 0.003	0.1/2
30 →40%	0.65 ±0.23	0.025 ± 0.004	1.0/2
40 →50%	0.93 ±0.22	0.025 ± 0.006	0.6/2
Average	0.98 ±0.33		

Figure 7.7: Fluctuations for simulated **HIJING events without using BRAG**, and with **exclusive** centrality bins. From the figure it can be concluded that the slopes within the statistical errors are consistent and that the value of intrinsic fluctuations is approximately 1. The slopes are comparable to the ones in figure 7.5.

Comparing figure 7.7 with 7.5 one can observe that the fluctuations using BRAG in the analysis leads to an increase on ω_N of approximately 1. This should be corrected for when calculating the intrinsic fluctuations from the experimental data later in section 7.4.

Figure 7.8 summarizes the results for ω_n obtained in this section. The values are obtained from figures 7.2, 7.3, 7.4, 7.5, 7.6 and 7.7. In the figure it is observed that for the exclusive bins (bottom figure) for the HIJING simulation, the estimates are about one fluctuation unit higher than for data. Within the error, the data is around one fluctuation unit, even though the exclusive bins seem to rise for more peripheral events. For the HIJING not processed in BRAG the fluctuations are aligned around 1. For the inclusive bins the HIJING simulation that was not processed through BRAG shows negative values of ω_n.

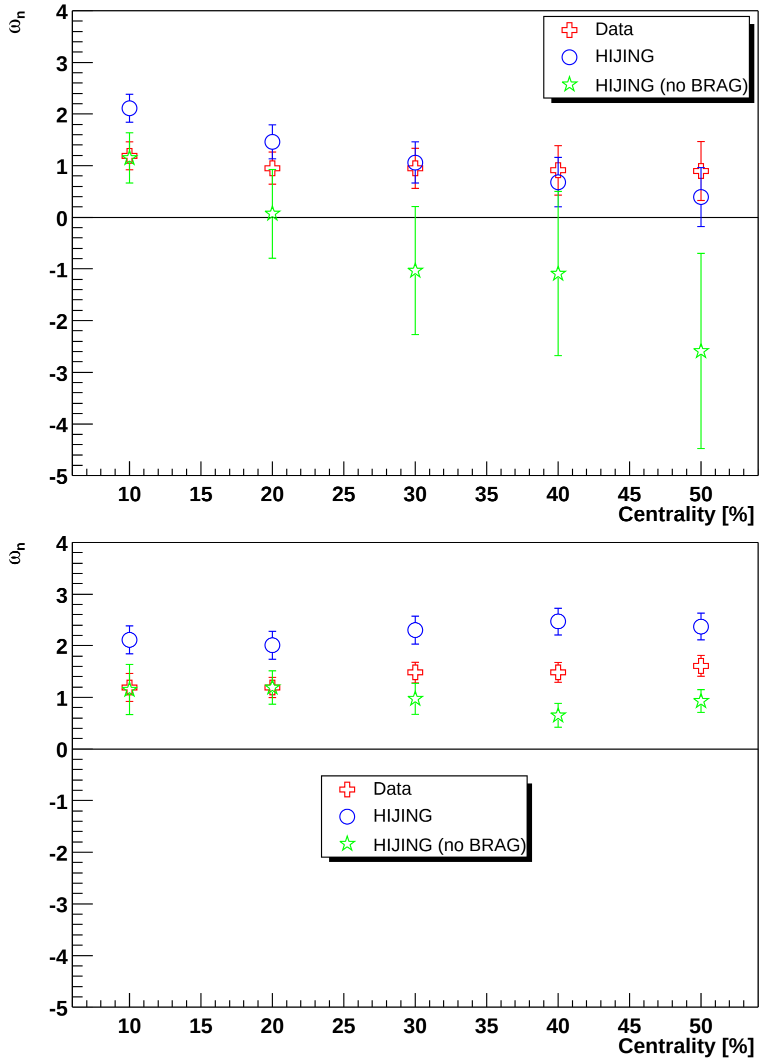

Figure 7.8: Estimating ω_n from fluctuation plots for data and HIJING (with and without using the simulations program BRAG) with inclusive (top) and exclusive (bottom) centrality bins. The negative estimates of ω_n are not understood for the inclusive centrality bins, especially not when comparing to the exclusive bins, where the estimates of ω_n seem to be 1, independent of centrality. From the inclusive plot two conclusions can be drawn. HIJING is approximately 2, which is one unit higher than data. BRAG affects HIJING by increasing fluctuation by approximately 1. The plotted errors correspond to the uncertainty in the fit.

In the following section the dependence of analyzing events as a function of rapidity bins will be examined. In general, the exclusive centrality cuts should be better defined, so they will be used in the following analysis.

7.2 Impact Parameter Fluctuation: Dependence on η

In equation 7.3 we have argued that ω is a function of multiplicity for different selections of collision centrality. The multiplicity for the figures in previous section have been obtained by selecting different tiles, i.e. different intervals in η. The multiplicity axis is therefore implicitly a pseudorapidity axis. This dependence will be examined in this section.

The η dependency described in equation 7.3 is further examined by calculating the fluctuations between tiles in a given ring, thus at the same η value, for various centralities. This is done in figures 7.9 to 7.11[1]. The procedure of making the plots has been the following

- The first group of points is obtained by treating tiles in a ring individually.
- The second group of points is obtained by adding the multiplicity of two tiles in a ring.
- The third group of points is obtained by adding the multiplicities for 3 tiles.
- The fourth point is obtained by adding the multiplicity for all four tiles in the ring.

In the figures in this section we effectively analyze the relation

$$\omega_N(\eta) = \omega_n(\eta) + \overline{N} \cdot \frac{\omega_{N_p}}{\overline{N}_p} \tag{7.5}$$

Since the fluctuation in the number of sources is not expected to depend on the rapidity, we would anticipate that the different curves would be parallel, but with different intercepts.

In figure 7.9 one may suspect that there is an error in the fit, since the same tile can contribute to several points, i.e. the points are not independent. This is however not the case. For data with a 0 to 10% centrality cut, as in figure 7.9, a similar plot for the fluctuations including tiles only once is shown in appendix E.2 in figure E.4 with corresponding fit values. It is noticed that there is no significant change in the fit parameters.

In figure E.3 (appendix E.2) the other centrality ranges, i.e. 10-20%, 20-30%, 30-40% and 40-50% are shown.

[1] and all figures in appendix E.2

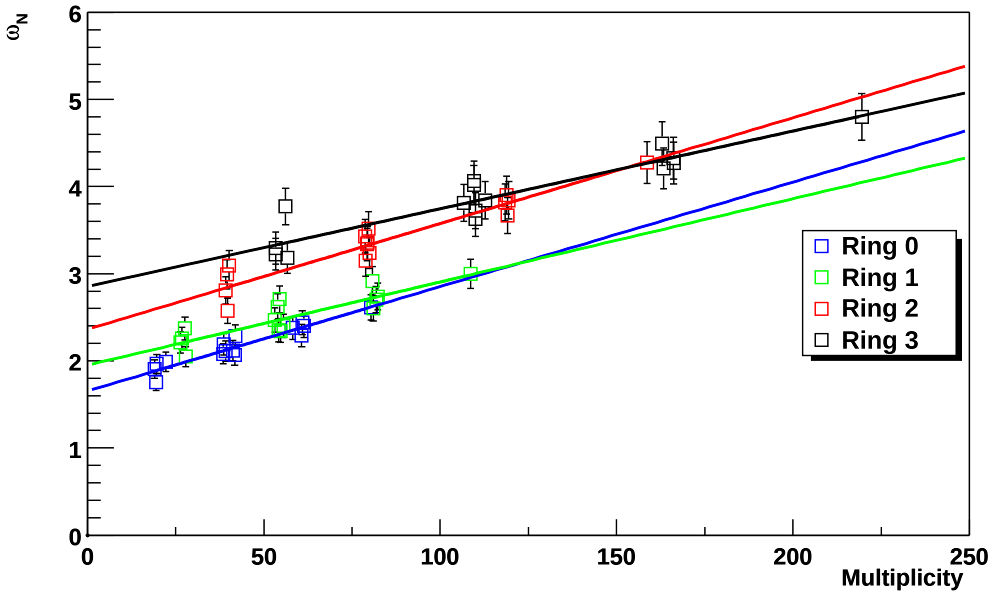

	η	$\omega_n(\eta)$	$\omega_{N_p}/\overline{N}_p$	χ^2/ndf
Ring 0	[-1.99;-1.73]	1.65 $\pm$0.08	0.012 $\pm$0.002	5.5/13
Ring 1	[-1.72;-1.36]	1.95 $\pm$0.09	0.010 $\pm$0.002	12/13
Ring 2	[-1.35;-0.83]	2.36 $\pm$0.11	0.012 $\pm$0.001	9.4/13
Ring 3	[-0.80;-0.03]	2.85 $\pm$0.14	0.009 $\pm$0.001	9.2/13
Average		2.20 $\pm$0.09	0.011 $\pm$0.001	

Figure 7.9: Investigating η dependency for **data** for rings 0 to 3 (0 to 10% central events). Error bars are statistical and the table below the figure lists the fit parameters. The intersection of the linear fit with the ω-*axis* is $\omega_n(\eta)$ and the slope of the line is $\omega_{N_p}/\overline{N}_p$, as described in equation 7.5.

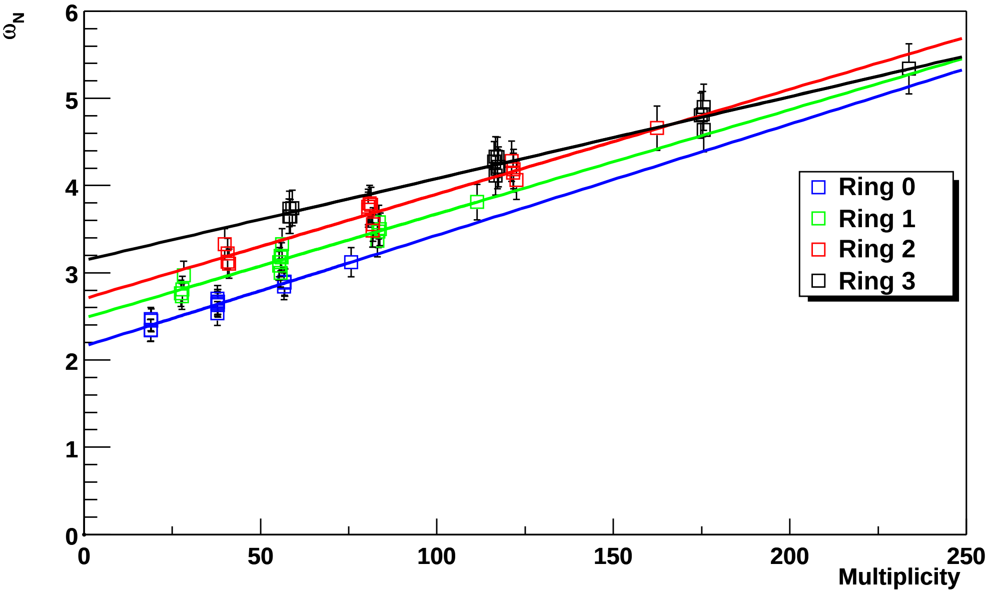

Ring	η	$\omega_n(\eta)$	$\omega_{N_p}/\overline{N}_p$	χ^2/ndf
0	[-1.99;-1.73]	2.16 $\pm$0.09	0.013 $\pm$0.002	1.8/13
1	[-1.72;-1.36]	2.48 $\pm$0.11	0.012 $\pm$0.002	4.0/13
2	[-1.35;-0.83]	2.70 $\pm$0.13	0.012 $\pm$0.001	4.1/13
3	[-0.80;-0.03]	3.14 $\pm$0.15	0.009 $\pm$0.001	1.4/13
Average		2.62 $\pm$0.11	0.012 $\pm$0.001	

Figure 7.10: Investigating η dependency for **BRAG simulated HIJING events** (0-10%). Error bars are statistical and the table below figure lists fit parameters.

In figure E.5 the other centrality ranges, i.e. 10-20%, 20-30%, 30-40% and 40-50% are shown, in the same way as previously with data (figure 7.10). The corresponding fit parameters are listed in the table below the figure.

The influence of using a wide vertex distribution for the HIJING simulations has been examined. The results are shown in figures E.6 and E.7 in appendix E.2 and the conclusion is that there is no significant effect of opening the vertex cut.

Since the intercepts ($\omega_N(\eta)$) for the fitted lines for simulated HIJING events are relatively higher than for data of figures 7.9 and 7.10 by $\Delta\omega_n \simeq 0.5$, an additional simulation has been made, using FRITIOF events to investigate a possible dependence on the choice of event generator. Similar plots are thus made for BRAG simulated FRITIOF events in figures E.8 and E.9. The 0-10% central events are presented in the following.

Finally the simulation without using BRAG is shown for 0 to 10% events in figure 7.11. The corresponding plots for 10-20%, 20-30%, 30-40% and 40-50% are found in figure E.10,

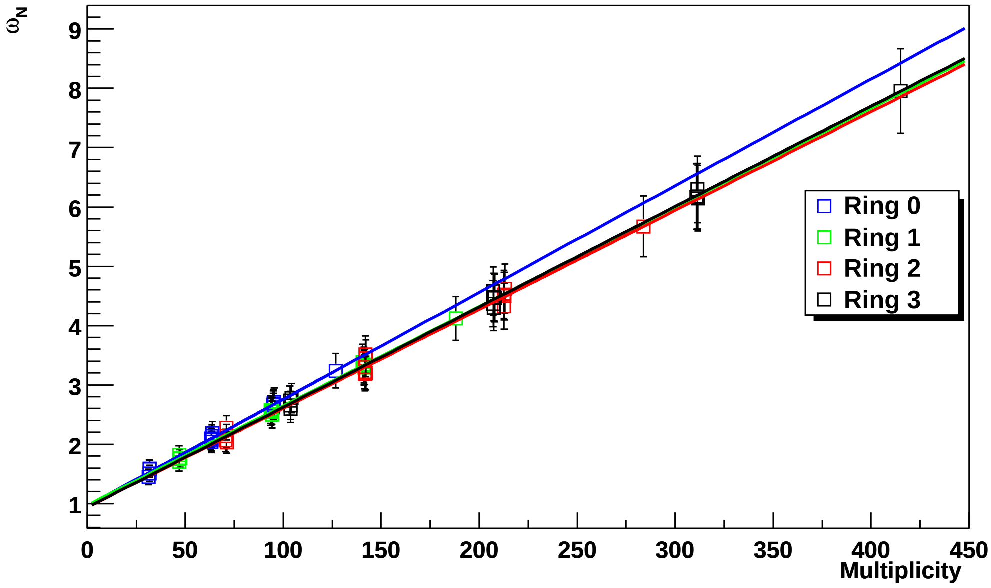

Ring	η	$\omega_n(\eta)$	$\omega_{N_p}/\overline{N}_p$	χ^2/ndf
0	[-1.99;-1.73]	0.96 ±0.11	0.018 ±0.002	1.1/13
1	[-1.72;-1.36]	0.97 ±0.13	0.016 ±0.001	0.5/13
2	[-1.35;-0.83]	0.94 ±0.16	0.017 ±0.001	2.3/13
3	[-0.80;-0.03]	0.93 ±0.21	0.017 ±0.001	0.6/13
Average		0.95 ±0.14	0.017 ±0.020	

Figure 7.11: Investigating η dependency for simulated **HIJING events without using BRAG**. It is concluded that all lines intercept in at $\omega = 1$ and are parallel. This indicates that there are only statistical fluctuations in the *raw* HIJING model, and that the estimates on ω_N from the BRAG simulated HIJING simulations in figure 7.10 are influenced by secondaries and energy deposit by slow particles and possibly also by the statistical and Monte Carlo algorithms employed in GEANT. Error bars on *data* are statistical and the table below the figure lists the fit parameters.

Figure E.10 in appendix shows a plot similar to 7.11 for the other exclusive centrality ranges. These fits for ω_N are (very) consistent with the estimated value shown here. The slopes are also very consistent, as shown in figure E.15 in appendix E.3. In the following section the estimated fluctuations (ω_N) are summarized. It is concluded that the data (figure 7.9) shows a relatively good consistency with the participant model theory. A systematic dependence of ω_n on η is observed. The overall level of ω_n varies between 1.65±0.08 and 2.85±0.14, with an average of 2.20±0.09. The HIJING simulation with and without (figure 7.10 and 7.11) the BRAG simulations show a significant increase in the amount of fluctuations (by about 1.5). This is interpreted as due to additional fluctuation related to the production of secondary particles and the detector response.

7.2.1 Summary of ω_N Estimates

The estimates of $\omega_N(\eta)$ in previous section are shown in figure 7.12 and discussed. The corresponding slopes $(\omega_{N_p}/\overline{N}_p)$ for the fits are shown in appendix E.3.

For the measured data (upper left in figure 7.12) a good consistency with the points representing different centralities is observed, i.e. no centrality dependence. This is in accordance with the assumption that the analysis procedure corrects for impact parameter fluctuations. The fluctuations decrease with η from approximately 3 at midrapidity to approximately 2 at $\eta \approx 2$. The error is the uncertainty of the linear fits from figures E.4 and E.3.

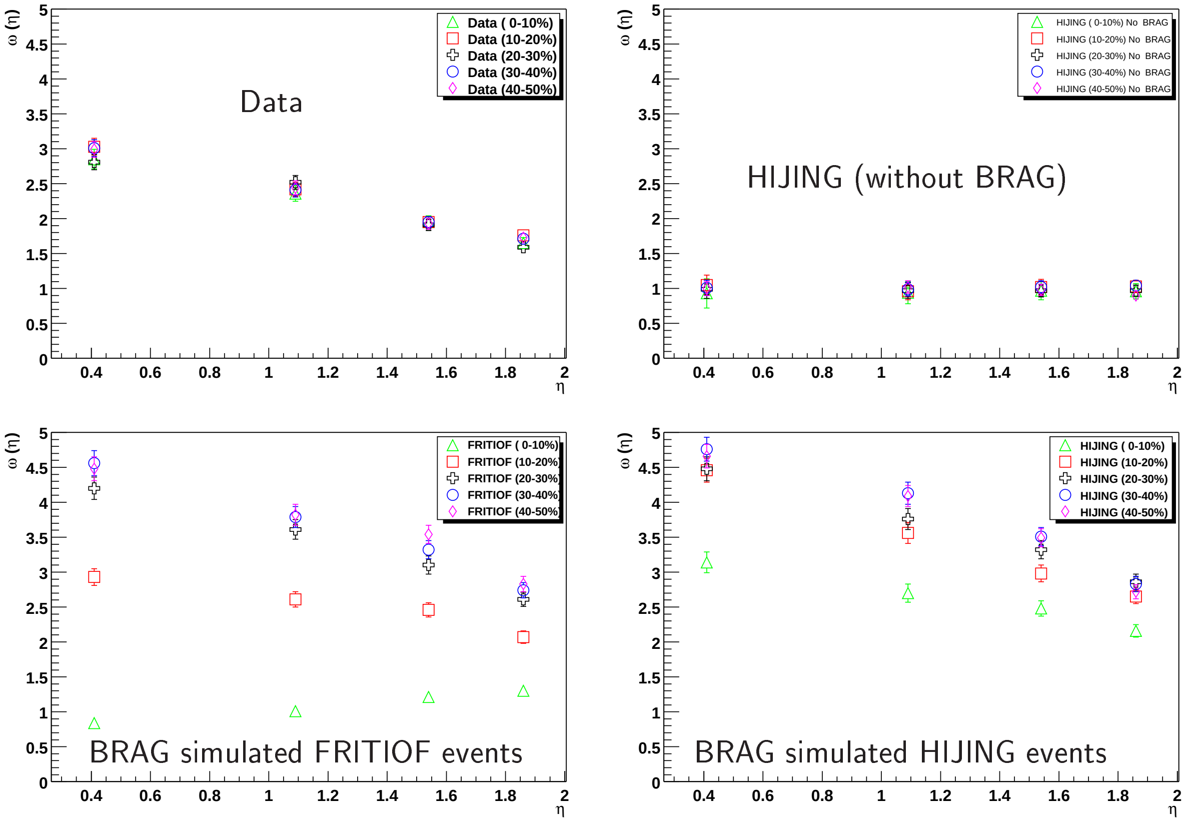

Figure 7.12: Fluctuations vs. η corrected for impact parameter fluctuations for data, FRITIOF and HIJING (with and without simulating) events. The upper left figure show data, the upper right for HIJING events without BRAG simulation. The lower left for BRAG simulated FRITIOF events and the lower right for BRAG simulated HIJING events. See explanation in text.

The HIJING events not processed by BRAG (upper right in figure 7.12) show that the fluctuations are 1 and constant. This indicates that HIJING only contributes with statistical fluctuations. Since the simulation does not include fluctuation contributions from secondary particle production or slow particles, one can now estimate this contribution by comparing this simulation to the BRAG simulated HIJING event in the lower right panel. This will be investigated in the following section. Also no centrality dependence is noticed. It is interesting that the difference in centrality for HIJING events occurs after the BRAG simulation. This could be due to a deficiency in the BRAG treatment of the most central collisions (highest multiplicities). The points and errors shown in upper right panel were drawn using fit values from figures 7.11 and E.10.

The fluctuation estimates by the BRAG simulated FRITIOF events (lower left panel in 7.12) are the most peripheral events (20-30%, 30-40% and 40-50%) consistent with the BRAG simulated HIJING events (lower right panel). But for the fluctuations from the most central (0-10%) events, the estimate of $\omega(\eta)$ from BRAG simulated FRITIOF events are not understood. This is believed to be a result of FRITIOF over predicting the multiplicity, as shown earlier in figure 5.8 but it is perhaps also due to a yet not understood effect in the BRAG detector simulation. The error plotted is the uncertainty in the linear fits from figures E.8 and E.9

Fluctuations estimated by HIJING events processed by the detector simulation BRAG show an increase for peripheral events, of approximately 1.5 as compared to data. For the central (0-10%) events, the fluctuations are approximately equal to the data and the 10-20% central FRITIOF events. This is explained by the larger multiplicity predicted by FRITIOF, shown in figure 5.8. The 0-10% most central FRITIOF events corresponds to the difference of the two spectra (HIJING and FRITIOF), and thus the HIJING 0-10% most central events are approximately equal to the 10-20% most central FRITIOF events. The fitted values for $\omega(\eta)$ does not change by changing the vertex acceptance from the initial $|z| \leq 2.50$ cm to $|z| \leq 0.45$. This can be verified by looking at figures E.6 and E.7. The points used to create the lower right figure were taken from figures 7.10 and E.5.

7.3 Fluctuations from Secondaries and Particle Momentum Distribution

The analysis in the previous sections suggests that it is possible to eliminate the influence of the fluctuations due to the number of sources and due to pseudorapidity bin size. The remaining fluctuation does however contain other contributions that are not related to source properties, but rather to the experimental method used to determine multiplicities. In particular two additional sources (labeled ω_ε in the following) of fluctuations should be considered

- Production of secondary particles
- Fluctuation in energy loss from slow particles

In the participant model shown in figure 7.1, the average energy deposit in the i^{th} tile $\overline{E}$ is assumed to be deposited by an average of N particles ($\overline{N}$) which in average deposits the energy $\overline{\varepsilon}$, i. e.

$$\overline{E} = \overline{N} \cdot \overline{\varepsilon} \tag{7.6}$$

In analogy with equation 7.3 we have

$$\omega_E \equiv \omega_\varepsilon + \overline{\varepsilon} \cdot \omega_N \tag{7.7}$$

where ω_ε is the fluctuation of the individual energy loss, i.e. $RMS^2/\overline{\varepsilon}$ and ω_N is the fluctuation of the number of particles. The fluctuation in total energy loss per unit average energy loss is approximately equal to the fluctuation in the number of particles due to this mechanism, i.e.

$$\frac{\omega_E}{\overline{\varepsilon}} = \frac{\omega_\varepsilon}{\overline{\varepsilon}} + \omega_N \tag{7.8}$$

7.3.1 Estimate of ω_{sec} and ω_{slow} using BRAG Simulated FRITIOF Events

The estimate of the contribution from secondaries is based on the simulations described in section 5.6. The mean and RMS values from the simulations including secondaries (simulation A) and the one without secondaries (simulation F) are now listed in tables 7.1 and 7.2, respectively.

η	Ring	Mean [GeV]	RMS	$\frac{\omega_\varepsilon}{\overline{\varepsilon}}$
[0.03;0.80]	4	0.001894	0.003090	2.662
[0.83;1.35]	5	0.002491	0.003652	2.149
[1.36;1.72]	6	0.003234	0.004289	1.759
[1.73;1.99]	7	0.003820	0.004674	1.497

Table 7.1: Fit values from the BRAG simulated FRITIOF events including secondaries (simulation A). Note that $\frac{\omega_\varepsilon}{\overline{\varepsilon}}$ = (RMS/Mean)^2. The values listed are from the graphs in section 5.6.

Figure 7.13 lists the values $\omega_\varepsilon/\overline{\varepsilon}$ from tables 7.1 and 7.2 as a function of η. The $\frac{\omega_E}{\overline{\varepsilon}}$ values are from tables 7.1 and 7.2. The figure shows that the contributions from slow particles are pseudorapidity dependent. The contribution from slow particles is assumed for each η *bin* to be the value of the simulation without secondaries. The contribution from secondaries is assumed to be the difference of the two simulations. The second term in the right hand side of equation 7.8 is discussed later in section 7.5.

The four points labeled *without secondaries* in figure 7.13 deviate by approximately by 0.9 at midrapidity and this deviation increases to 0.6 at $\eta \simeq 2$. The deviation from

η	Ring	Mean [GeV]	RMS	$\frac{\omega_\varepsilon}{\overline{\varepsilon}}$
[0.03;0.80]	4	0.001482	0.001395	0.886
[0.93;1.35]	5	0.001914	0.001617	0.714
[1.36;1.72]	6	0.002536	0.002001	0.623
[1.73;1.99]	7	0.003201	0.002469	0.595

Table 7.2: Fit values from the BRAG simulated FRITIOF events without secondaries (simulation F). Note that $\frac{\omega_\varepsilon}{\varepsilon} = (\text{RMS}/\text{Mean})^2$. The values listed are from the graphs in section 5.6.

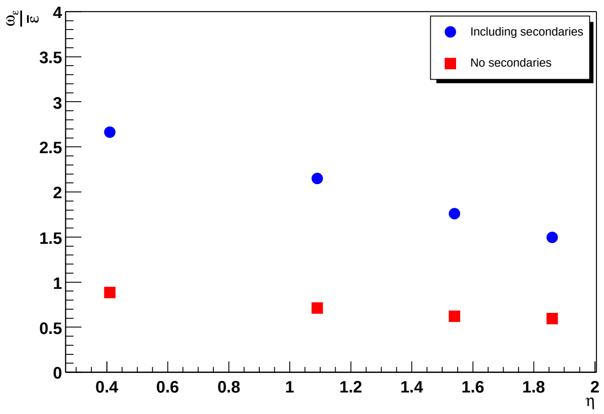

Figure 7.13: $\omega_\varepsilon/\overline{\varepsilon}$ vs. η (see equation 7.8). The estimates are based on BRAG simulated FRITIOF events described in section 5.6. In this plot the points *including secondaries* are used as an estimate of the correction $\omega_{sec} + \omega_{slow}$.

statistical fluctuations is believed to be an effect of slow particles depositing more energy in the tiles than a minimum ionizing particle (ω_{slow}). The additional effect of secondary fluctuations can be observed by comparing to the points from the simulation including secondaries. This difference is about 1.8 at midrapidity and decreases to 0.9 at $\eta \simeq 2$.

7.3.2 Estimate of ω_{sec} and ω_{slow} using *Raw* HIJING Events

An other way of determine the fluctuation from secondaries and slow particles is to process a HIJING simulation without using BRAG. In the simulation only pions, kaons and protons are *counted*. Defining virtual tiles as described earlier and thereafter repeating fluctuation calculations using the statistical module `BrStatistics`, the fluctuations are shown in figure 7.14.

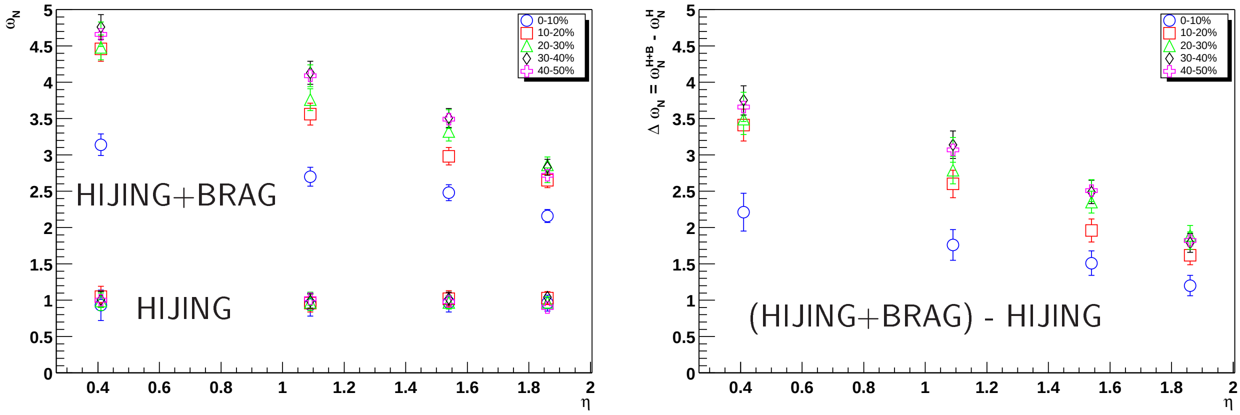

Figure 7.14: Fluctuations for HIJING events with and without BRAG. In left figure all points with $\omega > 2$ are for the BRAG simulated HIJING events, below for the *raw* HIJING events. The figure to the right shows the difference: (HIJING+BRAG) - HIJING. This difference is interpreted as the fluctuation contribution from $\omega_{sec} + \omega_{slow}$.

Comparing figures 7.13 and 7.14 it can be concluded that the estimates of $\omega_{sec} + \omega_{slow}$ is about 1 higher using HIJING events at midrapidity, than for the FRITIOF events. Since earlier multiplicity analysis with FRITIOF (figures 4.6 and 5.8) has shown that the FRITIOF model does not reproduce the number of charged particles produced, the second method shown in figure 7.14 and using HIJING is believed to a more accurate estimate.

7.4 Measured Intrinsic Fluctuation

The general assumption in this analysis is that the measured fluctuation (ω_m) is a sum of the following uncorrelated contributions

$$\omega_m = \omega_i + \omega_b + \omega_{slow} + \omega_{sec} + \omega_{vtx} \tag{7.9}$$

where

- ω_b is the impact parameter fluctuation.
- ω_{slow} is the contribution from slow particles which deposit more energy than minimum ionizing particles, which result in a higher measured multiplicity, i.e. momentum fluctuation.
- ω_{sec} is the fluctuation due to secondaries. The secondary particle production will contribute to the multiplicity, and therefore also to the fluctuations.
- ω_{vtx}, the uncertainty in vertex position, will contribute to uncertainty in determining the length the particle has traveled in the tile, and thereby the energy deposit.

The fluctuations from impact parameter has been evaluated in section 7.1. The influence of having a vertex opening of $\mid z \mid \leq 2.5$ cm was evaluated by HIJING simulation in section E.1 and was not found to be significant and thus $\omega_{vtx} \simeq 0$. Therefore the evaluation of the intrinsic fluctuations narrows down to

$$\omega_i = \omega_m - \omega_b - \omega_{sec} - \omega_{slow} \tag{7.10}$$

where $\omega_m - \omega_b$ is the measured fluctuation after correction for impact parameter fluctuations (see section 7.2). Figures 7.15 and 7.16 show ω_i as a function of η for the two different estimates of ω_{sec} and ω_{slow}. The error on the points is evaluated to be 0.5. This estimate is based on the assumption that the error from the following sources should be added linearly. The different contributions are from the following sources

- The systematic error on the multiplicity is 5%. This results in an error on ω of 5% from the argumentation in section 6.5. The total error on ω is therefore estimated to be about $3 \times 0.05 = 0.15$ at midrapidity and approximately $2 \times 0.05 = 0.1$ at $\eta \simeq 2$.
- Determination of $\omega_m - \omega_b$ has a typical error of 0.1. This estimate is made by evaluating the fits in figures 7.9 and E.3.
- Uncertainty in determining ω_{sec} and ω_{slow} from BRAG simulated FRITIOF events is evaluated to be 0.2 and 0.1, respectively. This contribution from these could however be larger.

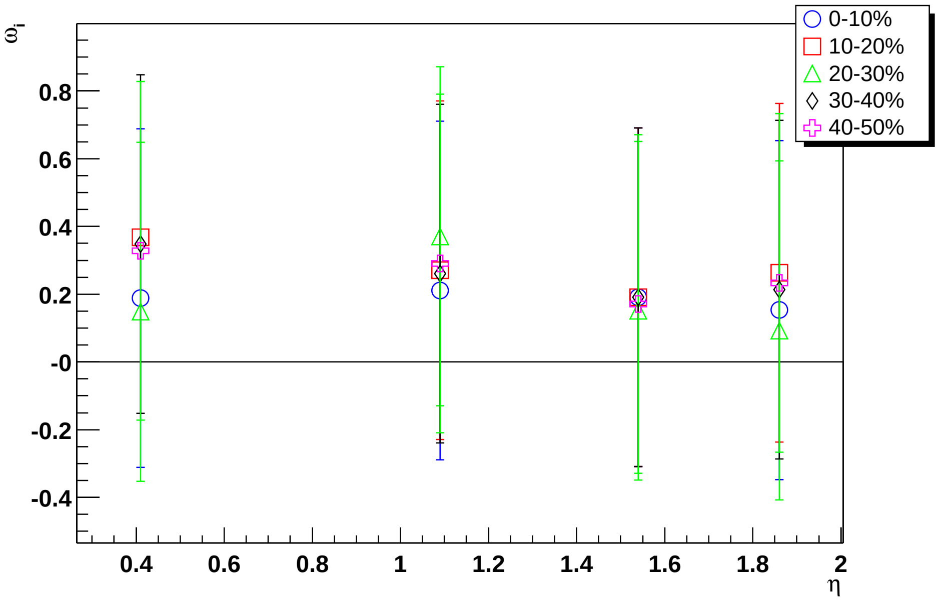

Figure 7.15: Intrinsic fluctuations vs. η obtained without scaling of the model dependent $\omega_{slow}+\omega_{sec}$. The fluctuation contribution from ω_{sec} and ω_{slow} is estimated using the BRAG simulated FRITIOF events as described in section 7.3.1. The error bar on ω_i has been set to 0.5 for reasons explained in text.

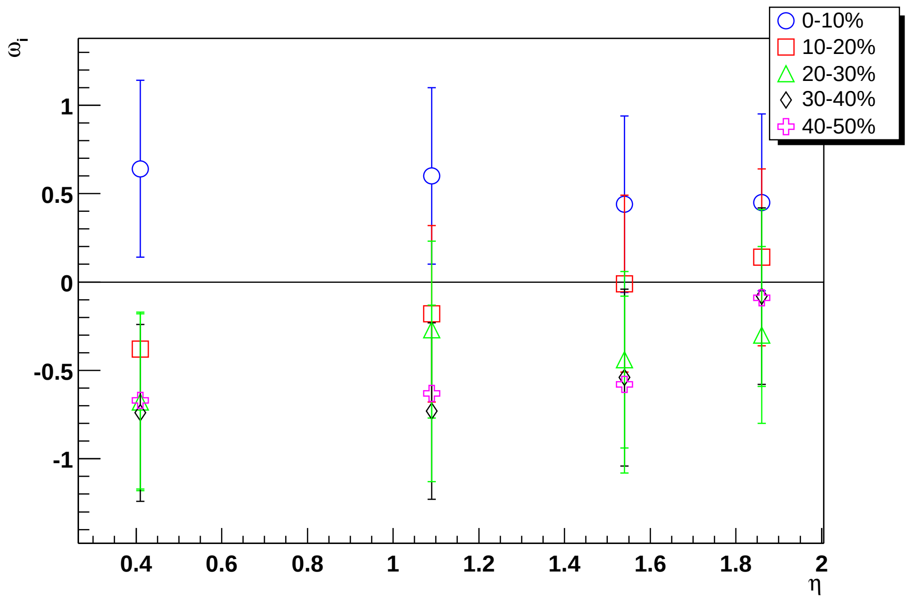

Figure 7.16: Intrinsic fluctuations vs. η obtained without scaling of the model dependent $\omega_{slow} + \omega_{sec}$. The fluctuation contribution from ω_{sec} and ω_{slow} is estimated using the comparison of the *raw* and BRAG simulated HIJING events as described in section 7.3.2. The error bar on ω_i has been set to 0.5, as in figure 7.15.

7.4.1 Correcting Intrinsic Fluctuations

The contributions are η dependent as shown earlier on. But it also seems from figure 7.12 that HIJING and FRITIOF predict systematically higher fluctuations than the data (figure 7.12), except for the very central simulations which show lower fluctuations. By comparing the $\omega_m - \omega_b$ from HIJING with data, the fraction $\omega_{Data}/\omega_{HIJING}$ is calculated for various η, using values from figures 7.9, E.3, 7.10 and E.5. The factor (shown in table E.1 in appendix E.4) is then used to scale the contribution from $\omega_{sec} + \omega_{slow}$ in equation 7.10, i.e.

$$\omega_{i,cor} = \omega_m - \omega_b - \frac{\omega_{Data}}{\omega_{HIJING}} \cdot (\omega_{sec} + \omega_{slow}) \tag{7.11}$$

The corrected values of the intrinsic fluctuation ($\omega_{i,cor}$) are shown in figures 7.17 and 7.18 for the two methods of estimating ω_{sec} and ω_{slow} which were described in sections 7.3.1 and 7.3.2, respectively.

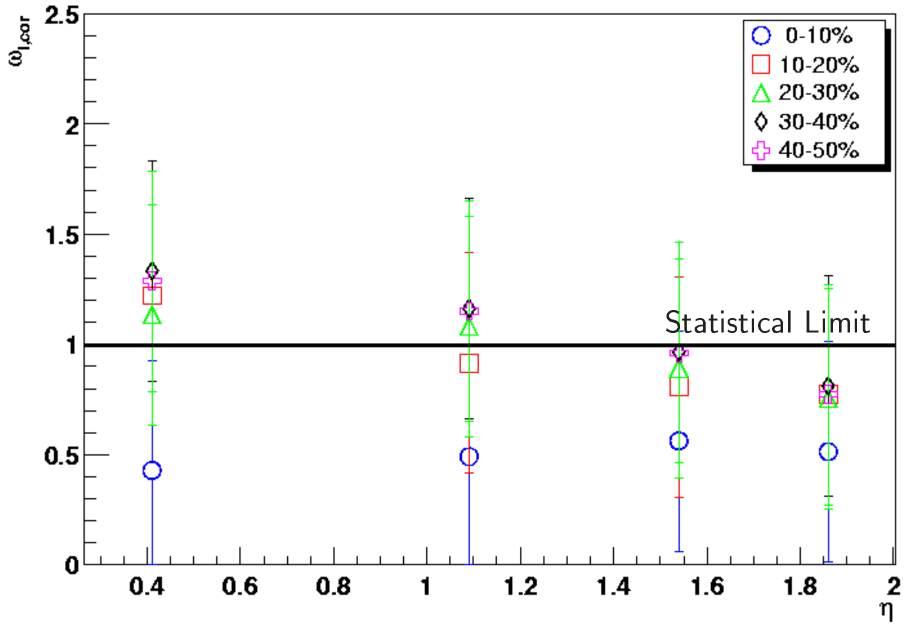

Figure 7.17: Intrinsic fluctuations after applying the correction described in equation 7.11. $\omega_{sec} + \omega_{slow}$ has been determined by using BRAG simulated FRITIOF events, as described in section 7.3.1. The error bar on $\omega_{i,cor}$ has been set to 0.5 as described in section 7.4.

The values of the intrinsic fluctuations in figures 7.17 and 7.18 are within the errors close to 1, but still a little below that value. In the following section expected values of the intrinsic fluctuation will be discussed.

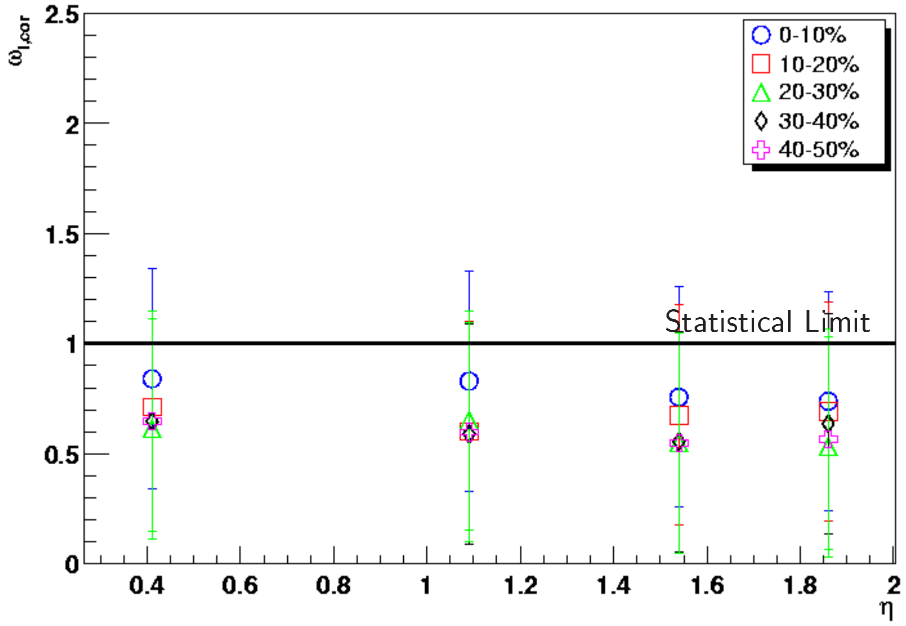

Figure 7.18: Intrinsic fluctuations with the correction described in equation 7.11. The method to determine ω_{sec} and ω_{slow} is by using the *raw* HIJING events, as described in section 7.3.2. Errors are evaluated as in figure 7.17.

7.5 Expected Intrinsic Fluctuation

The method of eliminating impact parameter fluctuations used in this analysis has been developed in cooperation with Henning Heiselberg[2] at NORDITA. In the following some model dependent expectations will be reviewed although it should be noted that no previous analysis of fluctuations exists using this method.

Assuming a statistical Poisson distribution the fluctuation can be shown [49] to be 1. If the binomial distribution with tossing probability p is assumed, the fluctuation is $\omega_N = 1 - p$. The probability for hitting a specific detector element, say a tile in the BRAHMS experiment is to the first order less than 1/40. So in this case $\omega_N \simeq 1$. For heavy ion collisions the purely statistical fluctuation is therefore approximately 1, whether it is Poissonian or binomial. The measured fluctuations in the analysis are close to this result.

Instead of assuming a statistical model, one could consider a thermal source, which in [49] is defined as

$$\omega_T = 1 + \frac{1}{e^{E_p/T} - 1} \tag{7.12}$$

where $(e^{E_p/T} - 1)^{-1}$ is the Boltzmann distribution for fermions of energy E_p. For a thermal model, the expected fluctuation $\overline{\omega}_{T_p}$ is 1.3, which is consistent with measurements at the NA49 experiment when impact parameter fluctuations are subtracted [49]. For pions we have $\overline{\omega}_{T_p} = 1.1$. For Boltzmann particles $\overline{\omega}_{T_p} = 1$ [43].

[2]email: heiselberg@nbi.dk

Previous studies of fluctuations in $p+p$ and $p+\overline{p}$ collisions in bubble chamber experiments [45], ISR [46] and UA5 [47] are indicated on figure 7.19 show a total production of 18 charged particles. This should from the right part of figure 7.19 correspond to a fluctuation in charged particle production of 5.3. This would also be the expected fluctuation at $\sqrt{s_{NN}}$ = 130 GeV if one had a detector covering 4π and if the physics were only a superposition of p+p collisions. Since a tile detector only covers a fraction of this, the expected fluctuation should approach 1, in agreement with results obtained in this analysis.

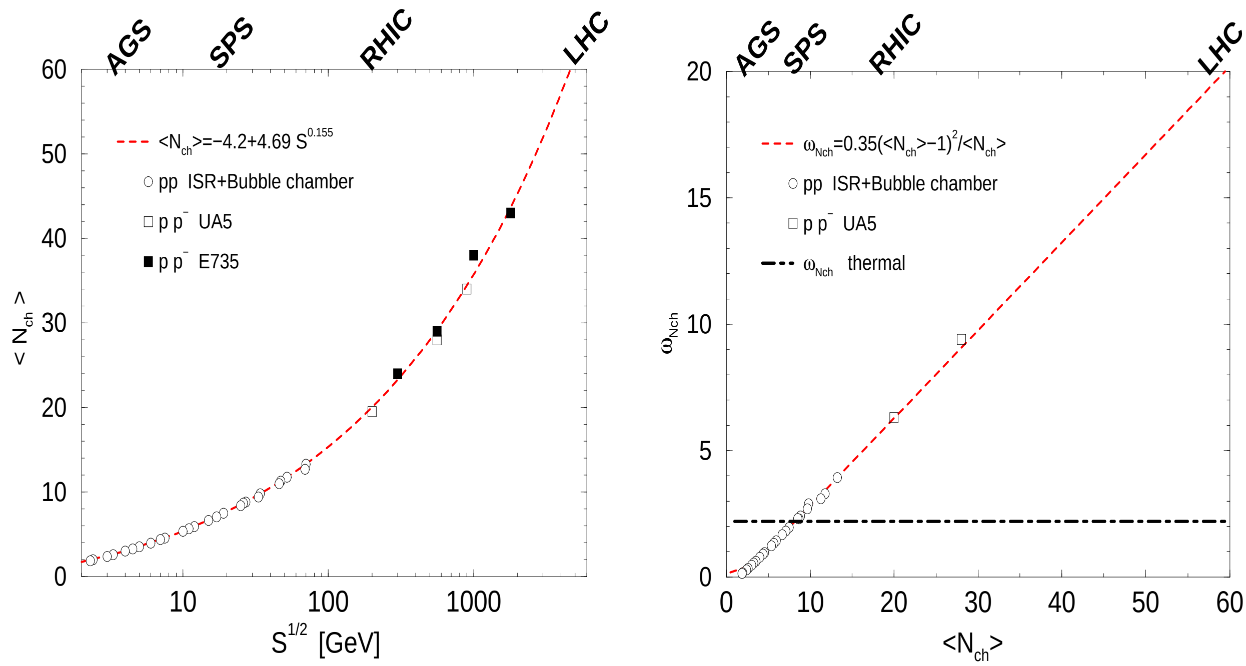

Figure 7.19: The left figure show the total production of charged particles in pp and $p\bar{p}$ collisions as a function of $\sqrt{s_{NN}}$. The right figure show the fluctuations in total produced charged particles. Experimental data from bubble chamber, ISR and UA5 experiments [49].

Chapter 8

Conclusion

In the present work an analysis of charged particle multiplicity fluctuation has been presented. The data analyzed were recorded by the BRAHMS experiment in year 2000 for Au+Au collisions at $\sqrt{s_{NN}} = 130$ GeV. The analysis has been performed in a pseudorapidity range of $-2 \leq \eta \leq 2$ using a scintillator array for charged particle multiplicity measurements and Čerenkov detectors for vertex determination.

Pseudorapidity distributions ($dN/d\eta$) have been calculated for various centralities and have been compared with published BRAHMS results. The analyzed data, BRAG simulated HIJING events and the BRAHMS published $dN/d\eta$ charged particle multiplicity distribution were consistent.

It has been shown that fluctuations are constant as a function of azimuthal angle (ϕ). Consistency in multiplicity and fluctuations between different tile rows has also been verified.

The work presents a new method of eliminating impact parameter fluctuations which has been developed in cooperation with Henning Heiselberg and has been successfully applied to data, *raw* HIJING events and BRAG simulated HIJING and FRITIOF events.

Two methods to estimate fluctuations from secondary particle production (ω_{sec}) and slow particles (ω_{slow}) have been presented. The first method is to remove certain BRAHMS detector components in BRAG and to turn off hadronic interactions; the other is to turn off the detector simulation. The two methods show different results. The difference between the two methods is approximately 1 unit in ω.

The final estimates of the intrinsic fluctuations is dependent on which method of removing ω_{sec} and ω_{slow} was used. The first method (figure 7.15) gives intrinsic fluctuations of approximately 0.3±0.5, whereas the other method (figure 7.16) gives varying fluctuations from approximately −0.7±0.5 to 0.6±0.5. The simulated fluctuations turned out to be systematically higher than for data (figure 7.12) and so a correction to the estimates of ω_{sec} and ω_{slow} was introduced in section 7.4.1. Applying this correction to the previous estimates, the new corrected intrinsic fluctuations was of the 0.8±0.5 to 1.3±0.5 (figure 7.17) for BRAG simulated FRITIOF events. For the estimates using *raw* HIJING events, the intrinsic fluctuations were at an almost constant value from 0.6±0.5 to 0.8±0.5, as shown in figure 7.18. Within the error these corrected results are consistent with Poissonian statistical fluctuations. No large fluctuations such as fluctuations from density droplets were detected in the analysis. The results indicate, on the contrary, that the fluctuations may be below 1. This does however require a smaller error to verify. If the fluctuation is below 1, it may indicate a fluid behavior [43, 44] of the hot and dense matter.

The measured fluctuations (top left panel in figure 7.12) are approximately 3 at midrapidity and drop to approximately 2 at $\eta \simeq 2$. By subtracting the various fluctuation contributions and applying the correction described in section 7.4.1, the fluctuations shown in figure 7.18 are consistent with a statistical behaviour.

Appendix A

Kinematic Variables

In heavy ion high energy physics the speed of particles is often comparable to the speed of light, and therefore all kinematic calculations should be performed relativistically. The energy per nucleon in the center of mass system of a relativistic heavy ion collision is referred to as $\sqrt{s_{NN}}$. It is for fixed target defined as:

$$\sqrt{s_{NN}} = \frac{E_b}{\sqrt{\frac{1}{2}(\gamma_{lab} + 1)}} \tag{A.1}$$

where E_b denotes the beam energy and γ_{lab} is the given as $\frac{E_b}{m_N c^2}$, where m_N is the nucleon mass. For a collider like RHIC it is simply

$$\sqrt{s_{NN}} = E_1 + E_2 \tag{A.2}$$

where E_1 and E_2 denotes the energy of each colliding beam. The transverse momentum and mass is defined respectively as

$$p_t = \sqrt{p_x^2 + p_y^2} \;\; and \tag{A.3}$$

$$m_t = \sqrt{m^2 + p_t^2} \tag{A.4}$$

where p_x and p_y are the components of $\mathbf{p}$ in the x and y direction respectively.

The velocity is not additive in relativistic calculations. Instead the rapidity y, is used. The rapidity is defined as

$$y = \frac{1}{2}\, ln\left(\frac{E + p_z}{E - p_z}\right) = \frac{1}{2}\, ln\left(\frac{1 + \beta cos\theta}{1 - \beta cos\theta}\right) \quad , \tag{A.5}$$

where the energy E is defined as $E^2 = \mathbf{p}^2 + m^2$, p_z is the momentum parallel to beam axis, $\beta \simeq c$ and θ is the scattering angle between the beam axis and $\mathbf{p}$. The rapidity only changes by an additive constant by Lorentz transforming along the beam axis as shown in equation A.6. The Lorentz transformation is as follows:

$$y' = y - \frac{1}{2}\ ln\left(\frac{1+\beta}{1-\beta}\right) \tag{A.6}$$

In the non-relativistic limit, the rapidity approaches parallel velocity divided by c. If the mass is unknown, one can use the pseudorapidity η defined as:

$$\eta = \frac{1}{2}\ ln\left(\frac{p+p_z}{p-p_z}\right) = -ln\left(tan\frac{\theta}{2}\right)\quad , \tag{A.7}$$

where p is the momentum of the particle. For high energies $y \approx \eta$ because $pc \gg mc^2$ and thus $E^2 = p^2c^2 + m^2c^4 \Rightarrow E \approx pc$.

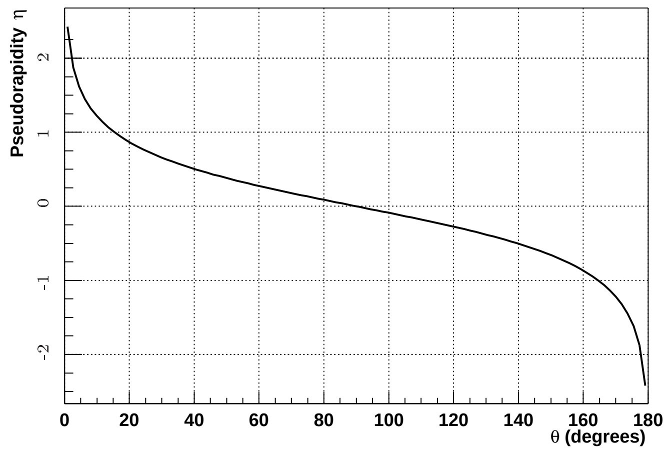

Figure A.1: The pseudorapidity as a function of scattering angle.

Appendix B

BRAG Simulations

Throughout the thesis simulated data has been used. Reading sections B.1 to B.4 should make it easier for others to make event generated files and BRAG simulations. Section B.5 contains graphs which were omitted in section 5.6.

B.1 Running the FRITIOF 7.02 Event Generator

The FRITIOF model can be downloaded from CVS, as described in the BRAT guide [68]. When everything is installed the file `fr.input` has to be edited in order to specify the simulation. An example of an input file for 1000 minimum bias (0 to 20 fermi) Au+Au collisions at $\sqrt{s_{NN}} = 130$ GeV for is shown below:

```
CMS AU AU NNNN 130. 1000 0. 20. 1 runMB1000ev.dat
```

The output file name is specified `fr.input` and is in zebra format[1].

B.2 Running the HIJING 1.36 Event Generator

The HIJING event generator is also downloaded form the CVS as described in the BRAT guide [68]. When HIJING has been installed the input for the simulation has to be defined in the file named `hijing.dat`. This file has to contain $\sqrt{s_{NN}}$ energy as the first argument, otherwise the simulation will be aborted. An example of an input file for 5000 minimum bias Au+Au collisions at $\sqrt{s_{NN}} = 130$ GeV is shown below:

```
'ECM (GeV)'
130.0
'A projectile'
197
'Z projectile'
```

[1]Information on this format can be found at `http://www.atd.ucar.edu/rdp/zebra/doc/Intro/Intro.html`.

```
79
'A target'
197
'Z target'
79
'bmin'
0.
'bmax'
20.
'nevents'
5000
```

In order to run the simulation, one should simply write `brhijing` in the directory where the `hijing.dat` is located, if `brhijing` is defined on system level. The output file is default written in zebra format and is named `tape1`.

The default HIJING includes physics such as *jet quenching* and *shadowing*, but it is possible to switch off these physics in the source file `hijing_main.f`. The options for *jet quenching* is `IHPR2` and for *shadowing* it is called `IHPR2(6)`.

B.3 Procedure used to make volumes inactive

In order to make specific parts of the detector inactive one should implement commands like: `set_tree beam z` in the `.kumac` file.[2] In the analysis this method did not work, and so instead BRAG was recompiled without the detector volumes.

Before recompiling BRAG some lines in the file `brag/src/user/zigeom.F` were commented out, in order to make beam pipe, silicon detectors, and the support for the tiles inactive during the simulation. The lines were:

```
call bd_prea
call bd_supp
call bd_endc
call bd_spaa
call bd_phot
call bd_beampipe
call bd_silicon
```

The way to recompile now is simply by writing:

```
make -f geant.mk clean_obj
./makegbr
```

[2]See example of kumac file in appendix B.4

B.4 Example of BRAG Macro

```
* Defining the geometry
  geoini
*
* Global setup
  set_tree bb afo
  set_tree mult afo
  set_tree zdc o
*
* Disable forward spectrometer
  set_tree fms1 z
  set_tree fms2 z
* Disable forward spectrometer
  set_tree mids z
*
  geodef
  geofin
* End of geometry definitions
*
* Switching off hadronic interactions. Default is 1.
  HADR 2
*
* Recalculation of physics parameters
  physi
*
  call gbr2c.f
  call init_detector
*
* kinematics
  evsplit 1
  cards spac 1
* Event generator input
  cards ukin 5 /nfs/hehi/hehi22/hehi/jakobsen/simu/frit702/130_auau_0_2.zdat
*
  kine 1 0. 130. 0. 180.  0. 360. 0 50
  swit 3 1
*
* Save the geometry, field and magnet settings
  setup/save geom   simulation_1000ev.geo
  setup/save field  simulation_1000ev.fld
  setup/save magnet simulation_1000ev.mag
*
```

```
* Binary data output file.
  call GBRFILE('simulation_1000ev.cdat')
*
* Simulate 1000 events
  analyze GBRANA 1000 1
*
  call GBREND
  quit
```

B.5 Additional Graphs

The following graphs were used in the data analysis in section 5.6. Table B.1 summarizes all number of entries, mean values and RMS for the graphs in this section.

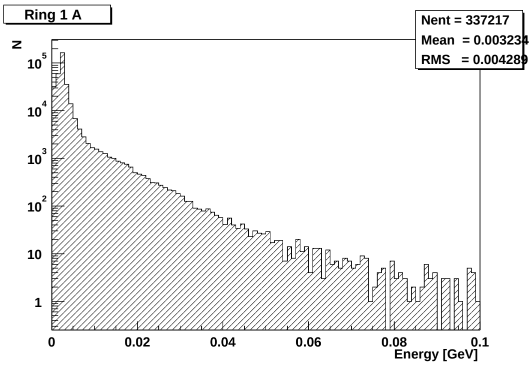

Figure B.1: Energy deposit in tiles for ring 1 with $\eta \in$ [-1.72;-1.36].

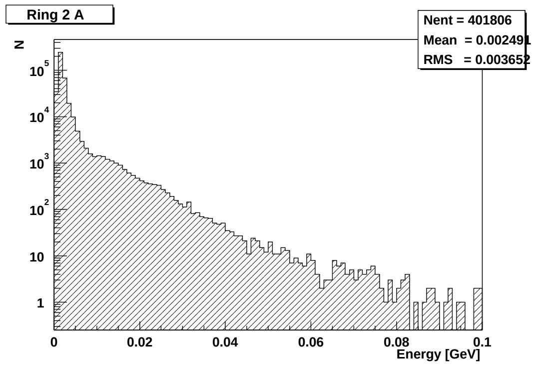

Figure B.2: Energy deposit in tiles for ring 2 with $\eta \in$ [-1.35,-0.83].

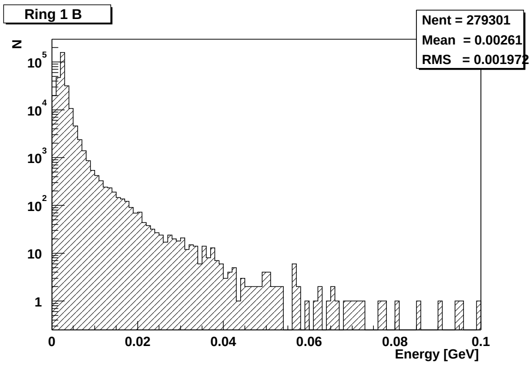

Figure B.3: Energy deposit in tiles for ring 1 with $\eta \in$ [-1.72,-1.36].

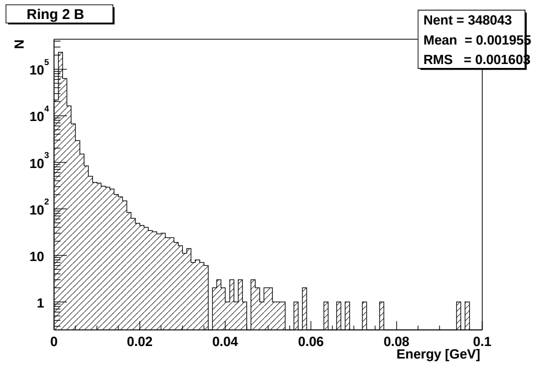

Figure B.4: Energy deposit in tiles for ring 2 with $\eta \in$ [-1.35;-0.83].

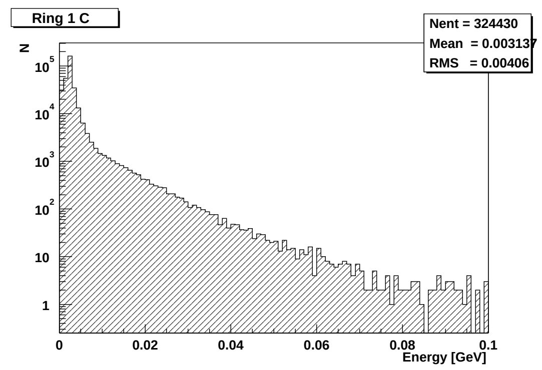

Figure B.5: Energy deposit in tiles for ring 1 with $\eta \in$ [-1.72;-1.36].

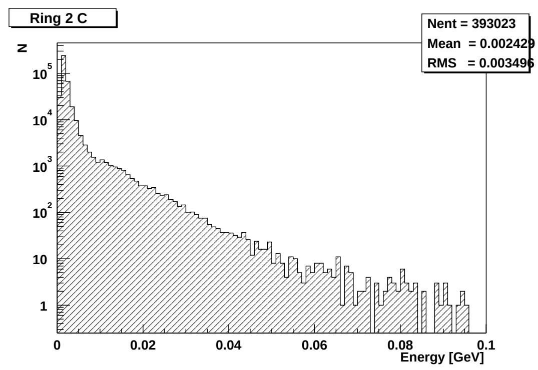

Figure B.6: Energy deposit in tiles for ring 2 with $\eta \in$ [-1.35;-0.83].

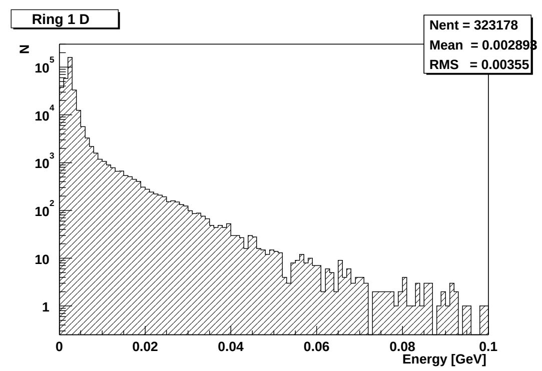

Figure B.7: Energy deposit in tiles for ring 1 with $\eta \in$ [-1.72;-1.36].

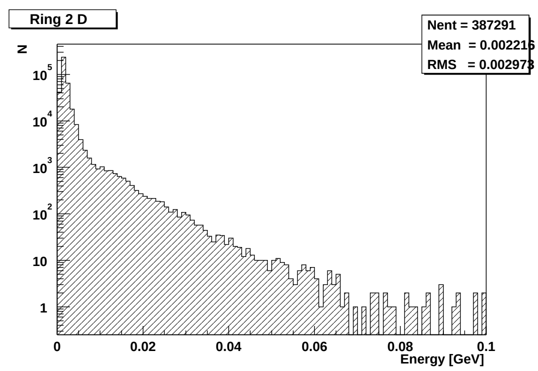

Figure B.8: Energy deposit in tiles for ring 2 with $\eta \in$ [-1.35;-0.83].

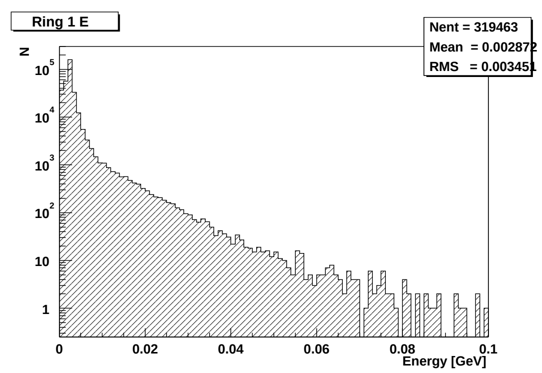

Figure B.9: Energy deposit in tiles for ring 1 with $\eta \in$ [-1.72;-1.36].

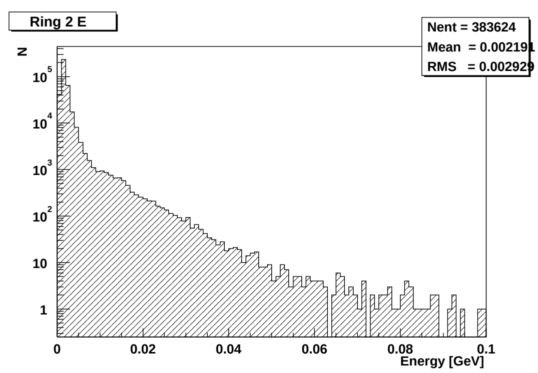

Figure B.10: Energy deposit in tiles for ring 2 with $\eta \in$ [-1.35;-0.83].

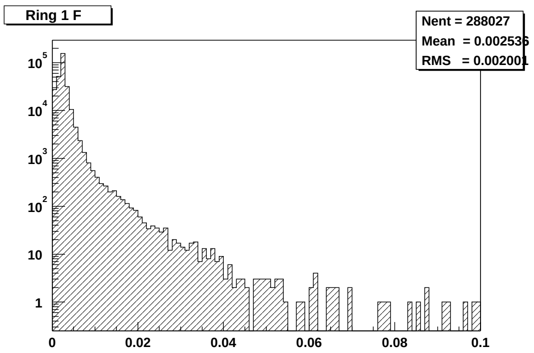

Figure B.11: Energy deposit in tiles for ring 1 with $\eta \in$ [-1.72;-1.36].

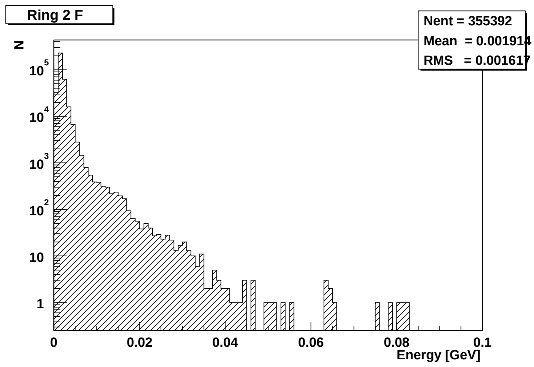

Figure B.12: Energy deposit in tiles for ring 2 with $\eta \in$ [-1.35,0.83].

Figure	N_{ent}	Mean	RMS
B.1	337217	0.003234	0.004289
B.2	401806	0.002491	0.003652
B.3	279301	0.002610	0.001972
B.4	348043	0.001955	0.001608
B.5	324430	0.003137	0.00460
B.6	393023	0.002429	0.003496
B.7	323178	0.002898	0.003550
B.8	387291	0.002216	0.002978
B.9	319463	0.002872	0.003451
B.10	383624	0.002191	0.002929
B.11	288027	0.002536	0.002001
B.12	355392	0.001914	0.001617

Table B.1: Summary of number of entries (N_{ent}), mean and RMS values for the graphs in this appendix.

Appendix C

Statistical Error on ω

The following calculations of the error on ω has been made using Bevington [86] and internal communication [87]. From the definition of ω in equation 6.11, we have defined the fluctuations for an element N as

$$\omega \equiv \frac{\overline{N^2} - \overline{N}^2}{\overline{N}} = \frac{\sigma_N^2}{\mu_N} = \omega(\mu_N, \sigma_N^2)$$

where μ_N ($\overline{N}$) is the mean value and σ_N^2 is the variance on N. Therefore:

$$\begin{aligned}
\sigma_\omega^2 &= \left(\frac{\partial\omega}{\partial\mu_N}\right)^2 \sigma_{\mu_N}^2 + \left(\frac{\partial\omega}{\partial\sigma_N^2}\right)^2 \sigma_{\sigma_N^2}^2 \\
&= \left(\frac{\partial}{\partial\mu_N}\frac{\sigma_N^2}{\mu_N}\right)^2 \sigma_{\mu_N}^2 + \left(\frac{\partial}{\partial\sigma_N^2}\frac{\sigma_N^2}{\mu_N}\right)^2 \sigma_{\sigma_N^2}^2 \\
&= \left(-\frac{\sigma_N^2}{\mu_N^2}\right)^2 \sigma_{\mu_N}^2 + \left(\frac{2\sigma_N}{\mu_N}\right)^2 \sigma_{\sigma_N^2}^2
\end{aligned}$$

From Bevington it can be derived, assuming that $\sigma_{N_i} = \sigma_N$, that

$$\sigma_{\mu_N}^2 = \frac{\sigma_N^2}{N_{ev}}$$

where N_{ev} denotes the number of events. Further we have

$$
\begin{aligned}
\sigma^2_{\sigma^2_N} &= \sigma^2_N \sum_{i=1}^{N_{ev}} \left(\frac{\partial \sigma^2_N}{\partial N_i} \right)^2 \\
&= \sigma^2_N \sum_{i=1}^{N_{ev}} \left(\frac{1}{N_{ev}-1} \frac{\partial}{\partial N_i} \sum_{j=1}^{N_{ev}} (N_j - \mu_N)^2 \right)^2 \\
&= \sigma^2_N \sum_{i=1}^{N_{ev}} \left(\frac{2}{N_{ev}-1} (N_i - \mu_N) \right)^2 \\
&= \frac{4\sigma^4_N}{N_{ev}-1}
\end{aligned}
$$

Inserting into the expression for σ^2_ω we obtain:

$$
\begin{aligned}
\sigma^2_\omega &= \frac{\sigma^4_N}{\mu^4_N} \frac{\sigma^2_N}{N_{ev}} + \frac{1}{\mu^2_N} \frac{4\sigma^4_N}{N_{ev}-1} \\
&= \frac{\omega^3}{N_{ev}\mu_N} + \frac{4\omega^2}{N_{ev}-1}
\end{aligned}
$$

Assume N_{ev} is large so that $N_{ev} - 1 \approx N$, then

$$
\sigma^2_\omega = \frac{\omega^2}{N_{\ ev}} \left(\frac{\omega}{\mu_N} + 4 \right)
$$

Finally, if $\mu_N \gg \omega$ we can ignore the ratio in the parenthesis and write

$$
\sigma^2_\omega = \frac{4\omega^2}{N_{ev}}
$$

Appendix D

The Participant Model

In section 7 equation 7.3 it was stated, that the intrinsic fluctuations (ω_n) in the number of produced particles could be written as $\omega_N = \omega_n + \omega_{N_p}$. We have that

$$N = \sum_{i=1}^{N_p} n_i$$

This implies that

$$\begin{aligned} N^2 &= n_1^2 + n_2^2 + ... + n_{N_p}^2 \\ &+ 2n_1 n_2 + 2n_1 n_3 + ... + 2n_1 n_{N_p} \\ &+ 2n_2 n_3 + 2n_2 n_4 + ... + 2n_2 n_{N_p} \\ &\vdots \\ &+ 2n_{N_{p-1}}\ n_{N_p} \end{aligned}$$

If $\overline{n}_1 = \overline{n}_2 = \ldots = n_{N_p} \equiv \overline{n}$ and if n_i and n_j are independent, i.e. $\overline{n_i n_j} = \overline{n_i} \cdot \overline{n_j}$, we have that

$$\overline{N^2} = \overline{N}_p \cdot \overline{n^2} + \overline{N_p(N_p - 1)} \cdot \overline{n}^2$$

and thus

$$
\begin{aligned}
\omega_N &= \frac{\overline{N^2} - \overline{N}^2}{\overline{N}} \\
&= \frac{\overline{N}_p \cdot \overline{n^2} + \overline{N_p^2} \cdot \overline{n}^2 - \overline{N_p} \cdot \overline{n}^2 - \overline{N_p}^2 \cdot \overline{n}^2}{\overline{N}_p \cdot \overline{n}} \\
&= \frac{\overline{N}_p \left(\overline{n^2} - \overline{n}^2\right) + \overline{n}^2 \left(\overline{N_p^2} - \overline{N_p}^2\right)}{\overline{N}_p \cdot \overline{n}} \\
&= \frac{\overline{n^2} - \overline{n}^2}{\overline{n}} + \overline{n} \cdot \frac{\overline{N_p^2} - \overline{N_p}^2}{\overline{N_p}} \\
&= \omega_n + \overline{n} \cdot \omega_{N_p}
\end{aligned}
$$

Appendix E

Evaluating Intrinsic Fluctuations

E.1 Changing Vertex Acceptance

In chapter 7 the dependence of vertex dependence was discussed. In this section of appendix E the figures referred to in the analysis are shown. The dependence has been examined by narrowing the vertex acceptance from $|z| \leq 2.50$ cm to $|z| \leq 1.25$ cm and opening the acceptance to $|z| \leq 5.00$ cm. The fluctuations vs. multiplicity for various inclusive centrality bins have then been drawn. Figures E.1 and E.2 show this for $|z| \leq 1.25$ cm and $|z| \leq 5.00$ cm respectively. The number of accepted events is influenced on the cut, and thus is 1200 analyzed events (0 to 10% central) halved and doubled for the two cuts. These numbers increase with a factor 5 when the centrality cut increases to 0 to 50%.

The two figures should be compared with figure 7.2 from chapter 7 where the vertex acceptance is $|z| \leq 2.50$ cm. When comparing to figure E.1 it is noticed that the value of ω_n is a little lower than for the $|z| \leq 2.50$ cm acceptance, but within the errors are they consistent. The error on ω_n is increases with centrality, which is not expected since the number of events used in analysis increases with centrality.

For the double vertex acceptance, i. e. $|z| \leq 5.00$ cm the equivalent distributions look as as shown in figure E.2. Within the errors I find no systematic dependence between $|z| \leq 2.50$ cm and $|z| \leq 5.00$ cm whereas there appears to be a slightly increased fluctuation effect.

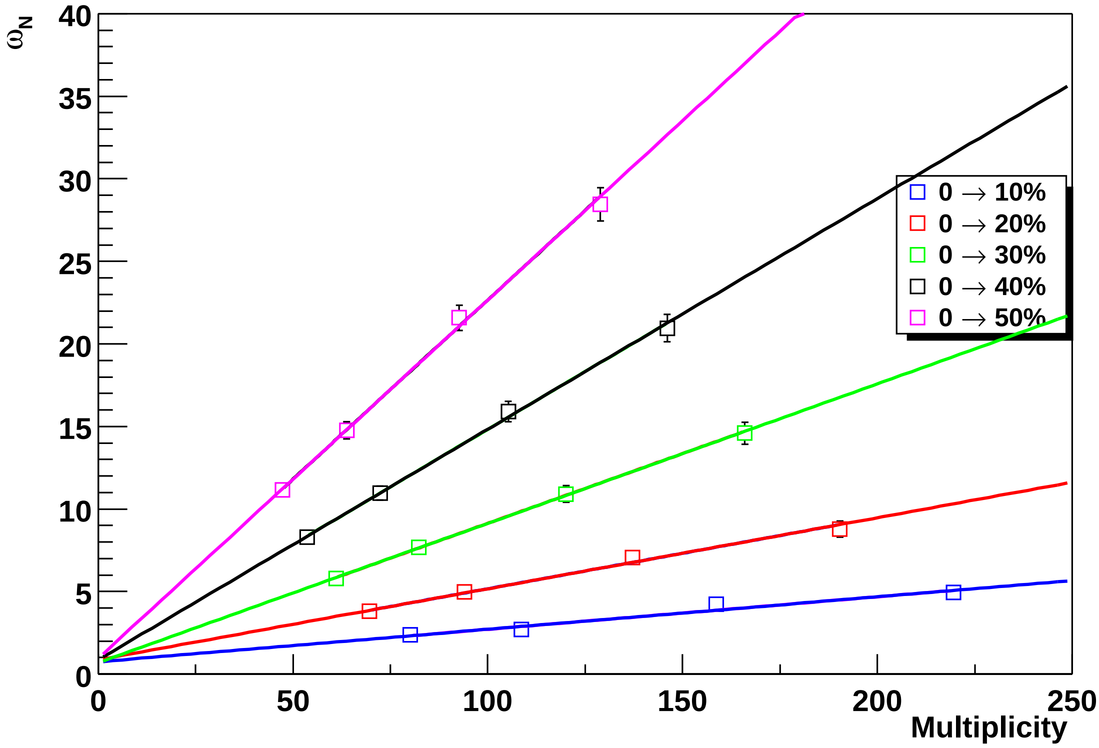

	ω_n	$\omega_{N_p}/\overline{N}_p$	χ^2/ndf
0 →10%	0.75 ±0.35	0.020 ± 0.003	2.2/2
0 →20%	0.87 ±0.41	0.043 ± 0.004	1.0/2
0 →30%	0.68 ±0.53	0.085 ± 0.006	0.1/2
0 →40%	0.86 ±0.66	0.140 ± 0.008	0.4/2
0 →50%	0.95 ±0.80	0.217 ± 0.012	0.7/2
Average	0.82 ±0.57		

Figure E.1: Fluctuations for **data** with **inclusive** centrality bins and $|z| \leq 1.25$ **cm**. Error bars are statistical and the fit parameters are listed in the table below figure. This vertex acceptance should be compared to the nominal vertex opening ($|z| \leq 2.5$ cm) shown in figure 7.2.

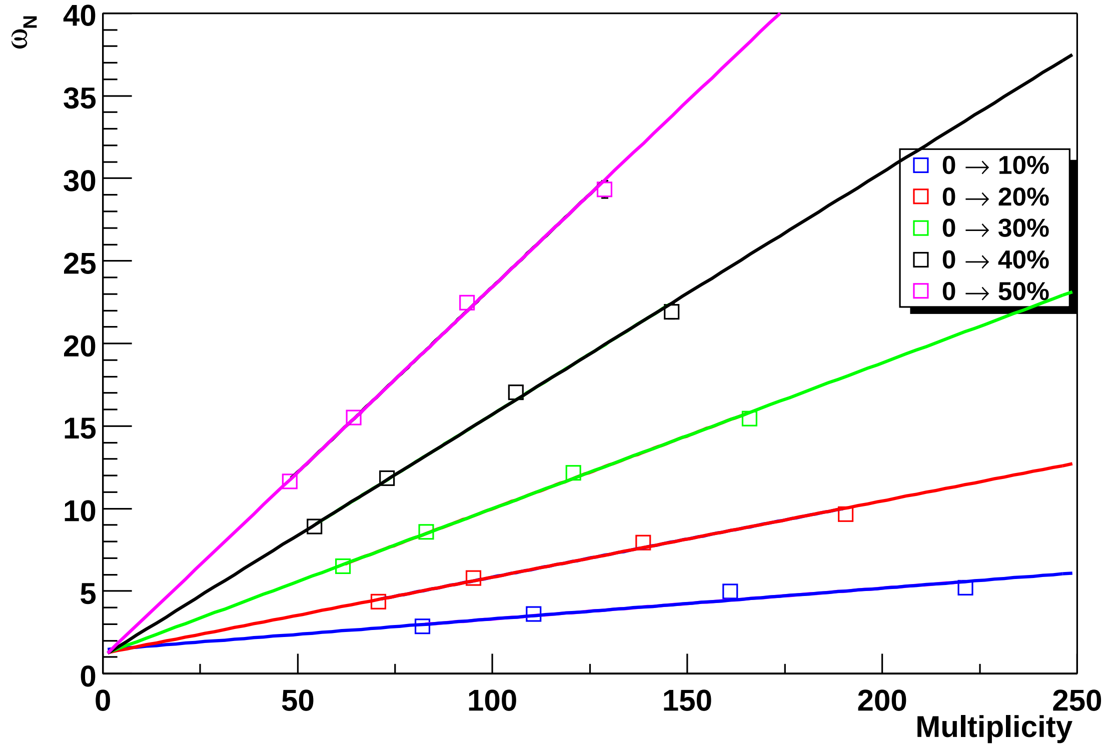

	ω_n	$\omega_{N_p}/\overline{N}_p$	χ^2/ndf
0 →10%	1.45 ±0.20	0.019 ± 0.002	11.7/2
0 →20%	1.23 ±0.24	0.046 ± 0.002	6.0/2
0 →30%	1.17 ±0.30	0.088 ± 0.003	3.2/2
0 →40%	1.05 ±0.36	0.146 ± 0.005	3.8/2
0 →50%	0.97 ±0.42	0.225 ± 0.006	3.1/2
Average	1.17 ±0.31		

Figure E.2: Fluctuations for **data** with **inclusive** centrality bins and $|z| \leq 5.00$ cm. Error bars are statistical and the fit parameters are listed in the table below figure. The effect of opening the vertex should be compared to the previous figure (E.1) and to 7.2 in section 7.

E.2 Fluctuation Dependency of η

In section 7.2 many figures and tables were omitted in order to make it easier to follow the steps in the analysis. This appendix contain these figures and tables [1].

Figure E.3 show the remaining fits for data with exclusive centrality bins. The fitted values for $\omega_n(\eta)$ are consistent with each other. It is noted that $\omega_n(\eta)$ increases from 1.6 to 3 as η goes from 2 to 0. The slope of the fits ($\omega_{N_p}/\overline{N}_p$) also seem consistent, not only for a given centrality cut, but also as a function of η.

Examining if there is an influence on the fit from the fact, that the multiplicity for a given tile, enters into more than one point. Figure E.4 shows this check and confirms that there is no difference between this method and the one used for figure 7.2. This check was repeated for other centralities.

The data in figures 7.2 and E.3 are now compared to simulations. Using BRAG simulated HIJING events, $\omega_n(\eta)$ and $\omega_{N_p}/\overline{N}_p$ are estimated in figures 7.5 and E.5. For the BRAG simulated HIJING events, the conclusion is that $\omega_n(\eta)$ now increases from 2.1 to 4.7. This is a factor 1-2 higher than data.

The influence of using a flat distributed vertex was also examined. Comparing two BRAG simulated HIJING events; one with a flat distribution ($|z| \leq 2.50$ cm) and one with $z = 0$ cm. The latter is shown for different centralities in figures E.6 and E.7. It should be mentioned that detector resolution in the digitization process *smears* the well defined vertex from the simulation in BRAG and so the vertices used in the analysis have vertex within the range $|z| \leq 0.45$ cm. The conclusion of this analysis is that there is no notable effect by changing this parameter.

Knowing that FRITIOF over predicts the multiplicity, it is still interesting to see what fluctuations that can be derived from this model. Simulations comparable to data in figures 7.2 and E.3 are shown in figures E.8 and E.9. The central (0-10%) FRITIOF simulation is not understood. The rest of the BRAG simulated FRITIOF events are more consistent with the BRAG simulated HIJING events. The value of $\omega_n(\eta)$ is generally a little lower for BRAG simulated FRITIOF than for BRAG simulated HIJING events.

Finally the fluctuations were examined for HIJING events that were not processed by the simulation program BRAG. This analysis was made in order to determine the effect secondaries and slow particles. The result with centrality ranging from 0 to 10% is included in the text (figure 7.11), but the other centrality ranges are shown in this appendix in figure E.10.

In order to be able to compare with the HIJING simulation similar plots to figure E.6 is now shown in figure E.7 for other centrality cuts.

[1] The size of the figures implicates that there can be only one figure per page. The text for the figures will therefore be on this page

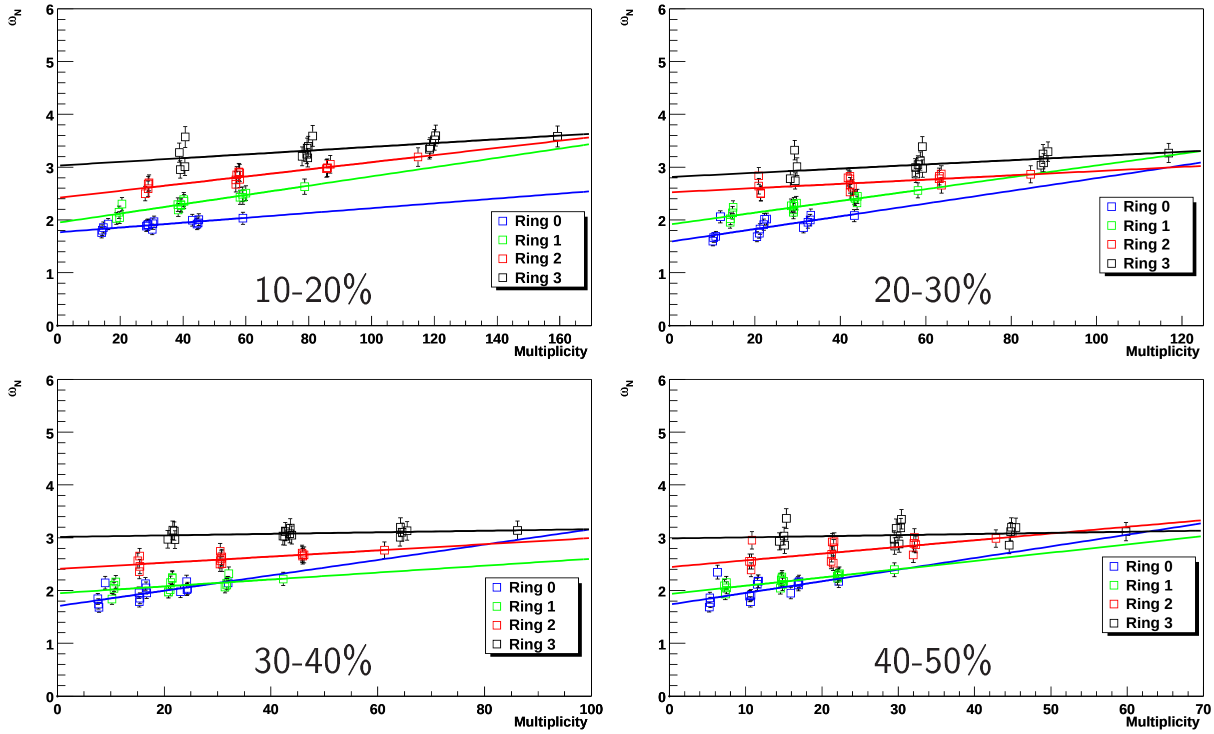

Centrality	Ring	η	$\omega_n(\eta)$	$\omega_{N_p}/\overline{N}_p$	χ^2/ndf
10-20%	0	[-1.99;-1.73]	1.76 ±0.07	0.005 ±0.002	2.7/13
10-20%	1	[-1.72;-1.36]	1.95 ±0.08	0.009 ±0.002	4.3/13
10-20%	2	[-1.35;-0.83]	2.42 ±0.10	0.007 ±0.002	17/13
10-20%	3	[-0.80;-0.03]	3.03 ±0.12	0.004 ±0.001	11/13
Average			2.29 ±0.08	0.006 ±0.002	
20-30%	0	[-1.99;-1.73]	1.59 ±0.07	0.012 ±0.003	20/13
20-30%	1	[-1.72;-1.36]	1.91 ±0.08	0.011 ±0.003	5.2/13
20-30%	2	[-1.35;-0.83]	2.52 ±0.10	0.004 ±0.002	19/13
20-30%	3	[-0.80;-0.03]	2.81 ±0.11	0.004 ±0.002	13/13
Average			2.21 ±0.08	0.008 ±0.002	
30-40%	0	[-1.99;-1.73]	1.71 ±0.07	0.015 ±0.004	17/13
30-40%	1	[-1.72;-1.36]	1.95 ±0.08	0.007 ±0.003	5.2/13
30-40%	2	[-1.35;-0.83]	2.41 ±0.10	0.006 ±0.003	4.5/13
30-40%	3	[-0.80;-0.03]	3.01 ±0.12	0.001 ±0.002	2.2/13
Average			2.27 ±0.08	0.007 ±0.003	
40-50%	0	[-1.99;-1.73]	1.73 ±0.07	0.022 ±0.006	29/13
40-50%	1	[-1.72;-1.36]	1.93 ±0.08	0.016 ±0.005	4.2/13
40-50%	2	[-1.35;-0.83]	2.44 ±0.10	0.013 ±0.004	18/13
40-50%	3	[-0.80;-0.03]	2.99 ±0.11	0.002 ±0.003	14/13
Average			2.27 ±0.08	0.013 ±0.004	

Figure E.3: Fluctuations vs. multiplicity for **data** with various centrality cuts. The upper left plot show the fluctuations with a centrality cut from 10 to 20%, upper right from 20 to 30%, lower left from 30 to 40% and lower right from 40 to 50% central events. Error bars are statistical and the values for the fits are listed in the table below figure.

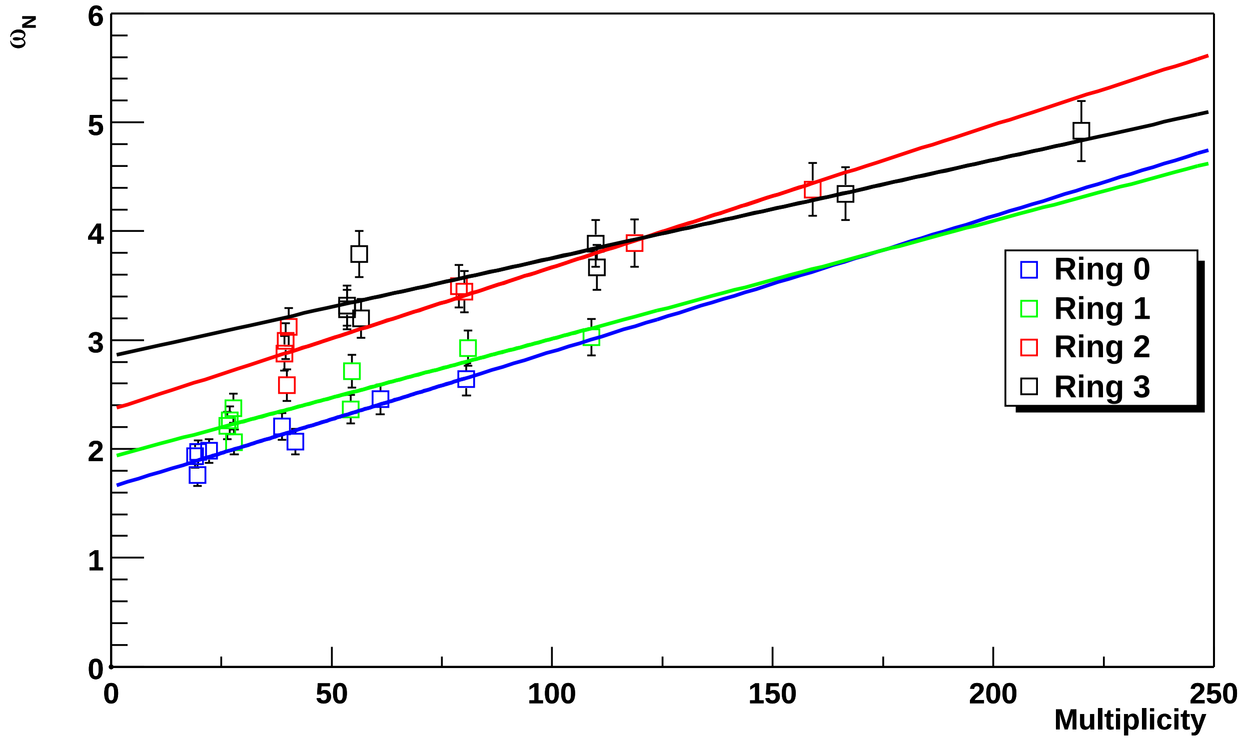

	η	$\omega_n(\eta)$	$\omega_{N_p}/\overline{N}_p$	χ^2/ndf
Ring 0	[-1.99;-1.73]	1.65 $\pm$0.08	0.012 $\pm$0.002	4.0/6
Ring 1	[-1.72;-1.36]	1.93 $\pm$0.10	0.011 $\pm$0.010	7.2/6
Ring 2	[-1.35;-0.83]	2.36 $\pm$0.13	0.013 $\pm$0.002	6.9/6
Ring 3	[-0.80;-0.03]	2.86 $\pm$0.15	0.009 $\pm$0.001	6.0/6
Average		2.20 $\pm$0.11	0.011 $\pm$0.005	

Figure E.4: Investigating η dependency for **data** for rings 0 to 3 (0 to 10% central events). For each *cluster* of points **a tile can only contribute once**, unlike in figure 7.9. Therefore only two points in second *cluster* contribute to the fit, and only one point in the third *cluster*. The results are consistent with the ones in figure 7.9. Error bars are statistical and the table below figure lists fit parameters.

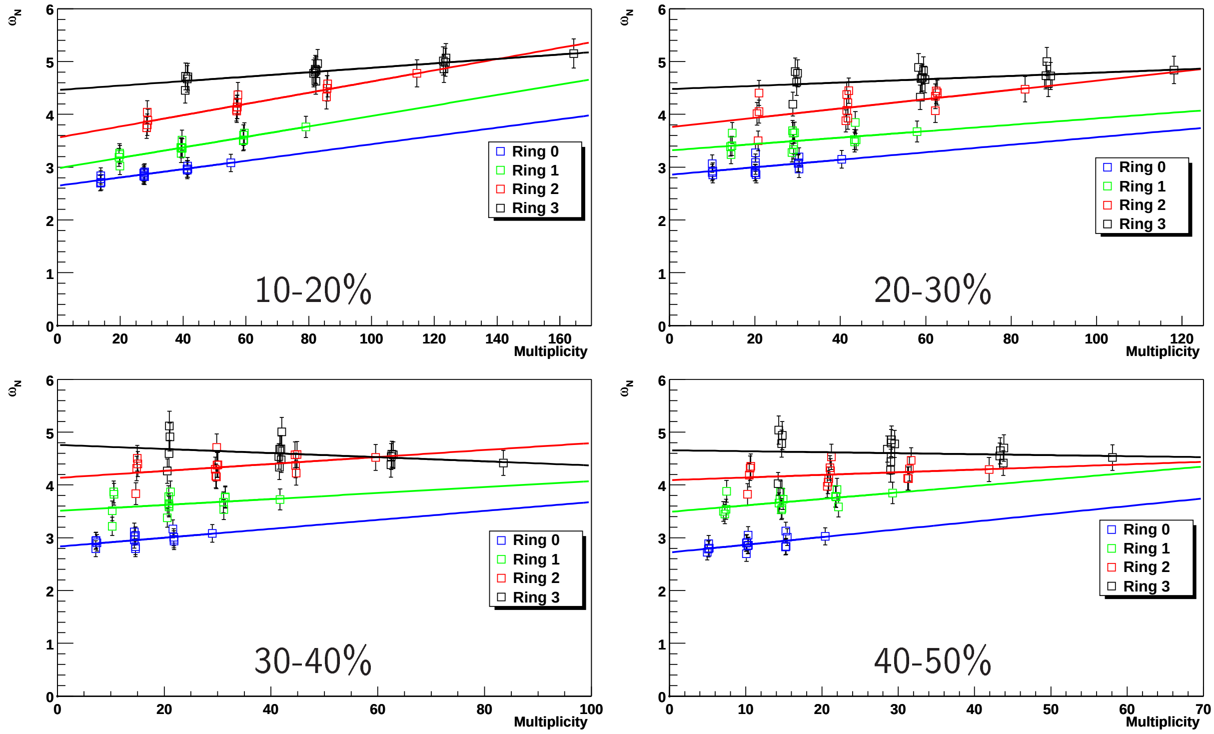

Centrality	Ring	η	$\omega_n(\eta)$	$\omega_{N_p}/\overline{N}_p$	χ^2/ndf
10-20%	0	[-1.99;-1.73]	2.65 $\pm$0.10	0.008 $\pm$0.003	0.9/13
10-20%	1	[-1.72;-1.36]	2.98 $\pm$0.12	0.010 $\pm$0.003	2.7/13
10-20%	2	[-1.35;-0.83]	3.56 $\pm$0.15	0.011 $\pm$0.002	2.8/13
10-20%	3	[-0.80;-0.03]	4.46 $\pm$0.17	0.004 $\pm$0.002	2.0/13
Average			3.41 $\pm$0.07	0.008 $\pm$0.002	
20-30%	0	[-1.99;-1.73]	2.86 $\pm$0.11	0.007 $\pm$0.005	6.4/13
20-30%	1	[-1.72;-1.36]	3.32 $\pm$0.13	0.006 $\pm$0.004	9.0/13
20-30%	2	[-1.35;-0.83]	3.76 $\pm$0.15	0.009 $\pm$0.003	17/13
20-30%	3	[-0.80;-0.03]	4.48 $\pm$0.17	0.003 $\pm$0.002	9.0/13
Average			3.61 $\pm$0.28	0.006 $\pm$0.007	
30-40%	0	[-1.99;-1.73]	2.83 $\pm$0.11	0.008 $\pm$0.006	5/13
30-40%	1	[-1.72;-1.36]	3.51 $\pm$0.13	0.006 $\pm$0.005	13/13
30-40%	2	[-1.35;-0.83]	4.13 $\pm$0.16	0.007 $\pm$0.005	11/13
30-40%	3	[-0.80;-0.03]	4.76 $\pm$0.17	-0.004 $\pm$0.003	11/13
Average			3.81 $\pm$0.13	0.004 $\pm$0.004	
40-50%	0	[-1.99;-1.73]	2.72 $\pm$0.10	0.015 $\pm$0.009	5.8/13
40-50%	1	[-1.72;-1.36]	3.49 $\pm$0.13	0.012 $\pm$0.008	6.4/13
40-50%	2	[-1.35;-0.83]	4.09 $\pm$0.15	0.005 $\pm$0.006	9.3/13
40-50%	3	[-0.80;-0.03]	4.66 $\pm$0.17	-0.002 $\pm$0.005	17/13
Average			3.74 $\pm$0.13	0.008 $\pm$0.006	

Figure E.5: Fluctuations vs. multiplicity for simulated HIJING events with various centrality cuts. The upper left plot show the fluctuations with a centrality cut from 10 to 20%, upper right from 20 to 30%, lower left from 30 to 40% and lower right from 40 to 50% central events. Error bars are statistical and the values for the fits are listed in the table below figure.

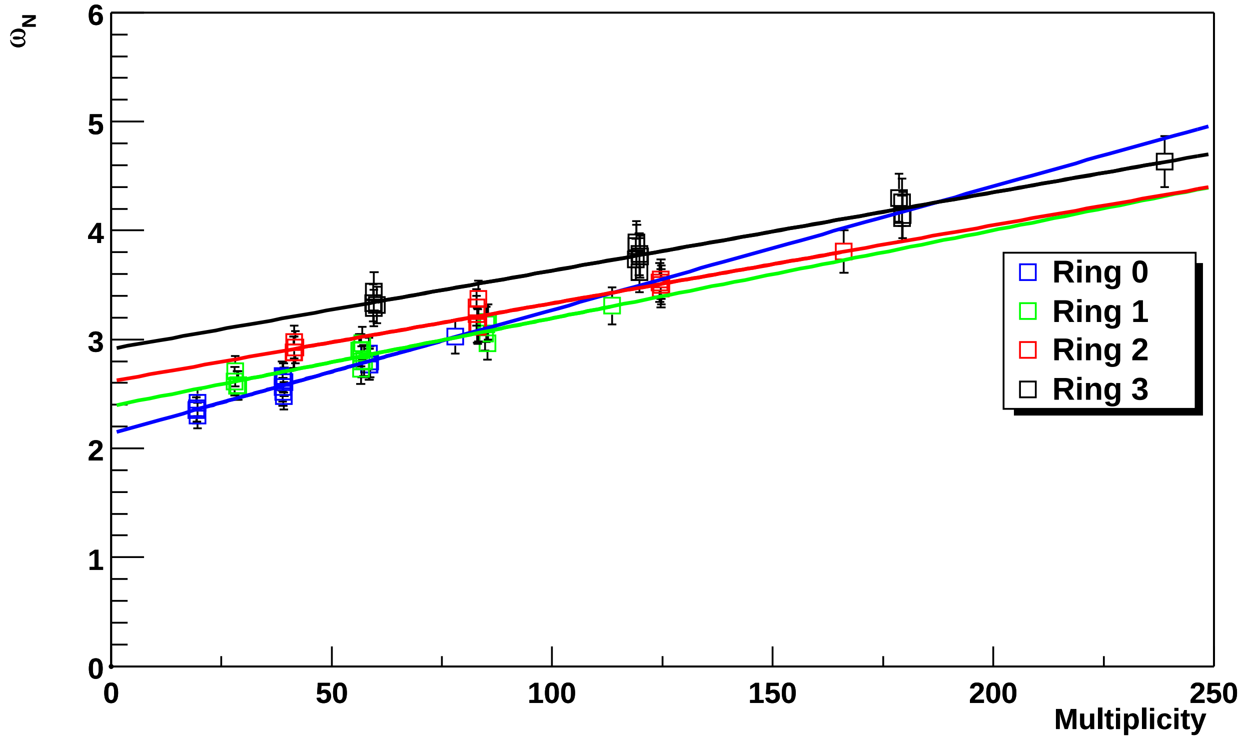

Ring	η	$\omega_n(\eta)$	$\omega_{N_p}/\overline{N}_p$	χ^2/ndf
0	[-1.99;-1.73]	2.14 ±0.09	0.011 ±0.002	2.4/13
1	[-1.72;-1.36]	2.39 ±0.10	0.008 ±0.002	3.4/13
2	[-1.35;-0.83]	2.62 ±0.11	0.007 ±0.001	2.3/13
3	[-0.80;-0.03]	2.91 ±0.12	0.007 ±0.001	2.3/13
Average		2.52 ±0.09	0.008 ±0.001	

Figure E.6: Investigating η dependency for BRAG simulated **HIJING** events with a vertex at **z=0**. Error bars are statistical and the table below figure lists fit parameters. The difference between this plot and figure 7.10 is that the vertex has in the simulation been fixed at z=0 instead of letting it move from -2.5 cm to 2.5 cm. It should be mentioned that the digitization *smears* the vertex a bit, so the actual cut on vertex is practically from -0.45 cm to 0.45 cm.

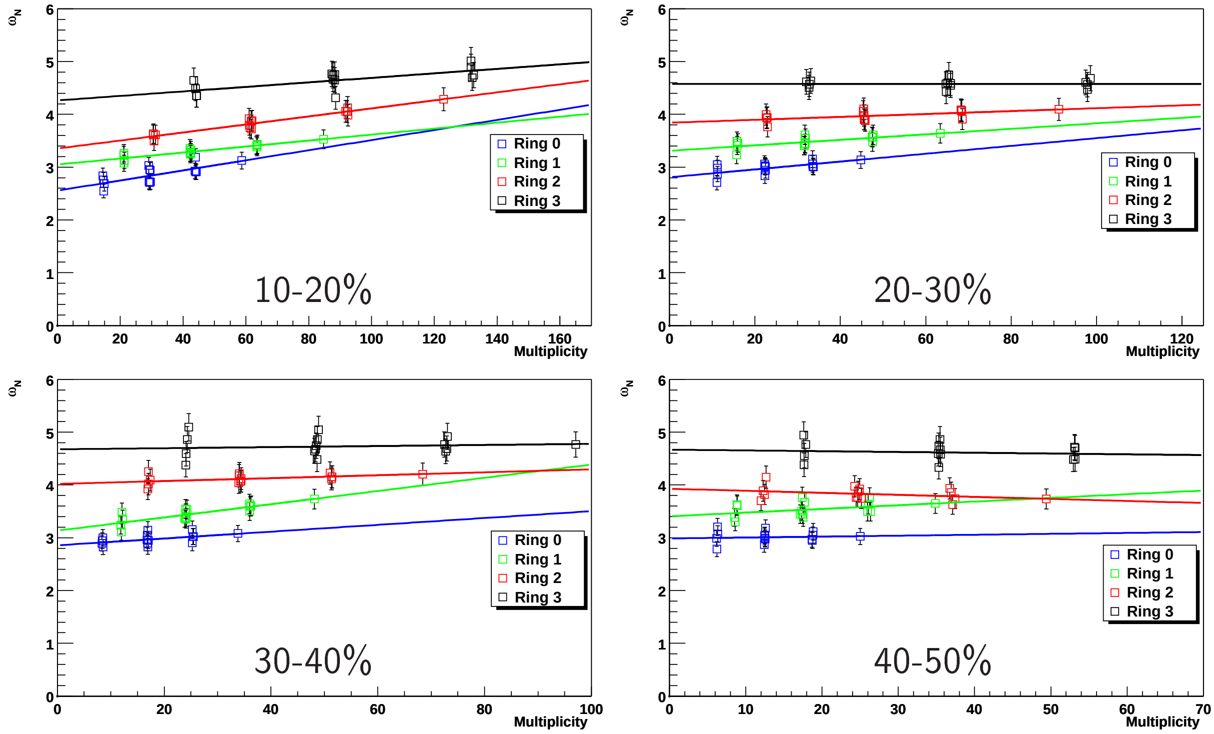

Centrality	Ring	η	$\omega_n(\eta)$	$\omega_{N_p}/\overline{N}_p$	χ^2/ndf
10-20%	0	[-1.99;-1.73]	2.55 ±0.10	0.010 ±0.003	9.8/13
10-20%	1	[-1.72;-1.36]	3.05 ±0.11	0.006 ±0.002	1.2/13
10-20%	2	[-1.35;-0.83]	3.35 ±0.13	0.008 ±0.002	1.5/13
10-20%	3	[-0.80;-0.03]	4.26 ±0.16	0.004 ±0.002	5.1/13
Average			3.30 ±0.11	0.007 ±0.002	
20-30%	0	[-1.99;-1.73]	2.81 ±0.10	0.007 ±0.004	5.3/13
20-30%	1	[-1.72;-1.36]	3.31 ±0.12	0.005 ±0.003	2.7/13
20-30%	2	[-1.35;-0.83]	3.84 ±0.13	0.003 ±0.003	2.3/13
20-30%	3	[-0.80;-0.03]	4.58 ±0.16	0.000 ±0.002	1.6/13
Average			3.63 ±0.12	0.004 ±0.003	
30-40%	0	[-1.99;-1.73]	2.86 ±0.10	0.006 ±0.005	5.0/13
30-40%	1	[-1.72;-1.36]	3.13 ±0.12	0.013 ±0.004	4.2/13
30-40%	2	[-1.35;-0.83]	4.02 ±0.14	0.003 ±0.004	2.0/13
30-40%	3	[-0.80;-0.03]	4.68 ±0.16	0.001 ±0.003	9.0/13
Average			3.67 ±0.12	0.006 ±0.004	
40-50%	0	[-1.99;-1.73]	2.99 ±0.10	0.002 ±0.007	6.9/13
40-50%	1	[-1.72;-1.36]	3.41 ±0.12	0.007 ±0.006	7.1/13
40-50%	2	[-1.35;-0.83]	3.93 ±0.13	-0.004 ±0.005	5.3/13
40-50%	3	[-0.80;-0.03]	4.67 ±0.16	-0.001 ±0.004	7.1/13
Average			3.75 ±0.12	0.001 ±0.005	

Figure E.7: Fluctuations vs. multiplicity for simulated **HIJING** events with a vertex at **z=0** for various centrality cuts. The upper left plot show the fluctuations with a centrality cut from 10 to 20%, upper right from 20 to 30%, lower left from 30 to 40% and lower right from 40 to 50% central events. Error bars are statistical and the values for the fits are listed in the table below figure.

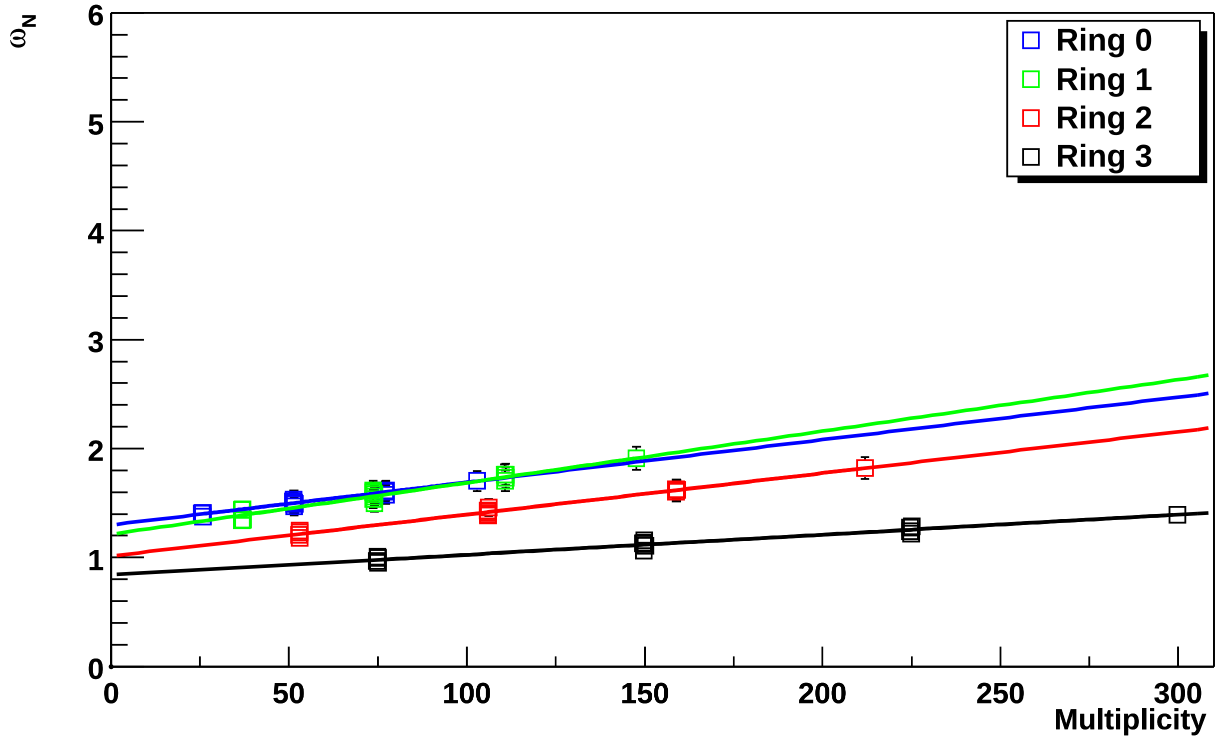

Ring	η	$\omega_n(\eta)$	$\omega_{N_p}/\overline{N}_p$	χ^2/ndf
0	[-1.99;-1.73]	1.30 ±0.05	0.004 ±0.001	0.6/13
1	[-1.72;-1.36]	1.21 ±0.06	0.005 ±0.001	3.1/13
2	[-1.35;-0.83]	1.01 ±0.05	0.004 ±0.000	1.2/13
3	[-0.80;-0.03]	0.84 ±0.04	0.002 ±0.000	2.6/13
Average		1.09 ±0.04	0.004 ±0.001	

Figure E.8: Investigating η dependency for BRAG simulated **FRITIOF** events. Error bars are statistical and the table below figure lists fit parameters. This figure is of special interest since we here see smaller fluctuations for tiles at midrapidity than at $\eta \approx 2$.

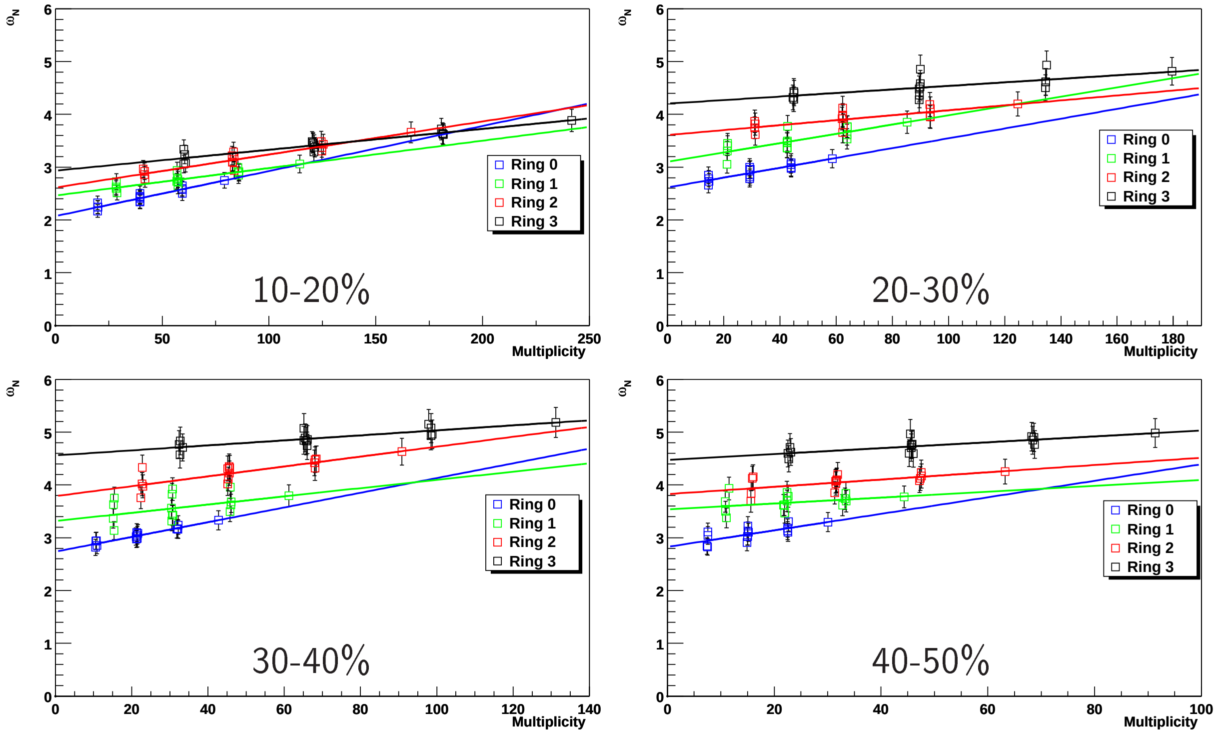

Centrality	Ring	η	$\omega_n(\eta)$	$\omega_{N_p}/\overline{N}_p$	χ^2/ndf
10-20%	0	[-1.99;-1.73]	2.07 ±0.09	0.009 ±0.002	2.4/13
10-20%	1	[-1.72;-1.36]	2.46 ±0.10	0.005 ±0.002	3.6/13
10-20%	2	[-1.35;-0.83]	2.61 ±0.11	0.006 ±0.001	4.2/13
10-20%	3	[-0.80;-0.03]	2.93 ±0.12	0.004 ±0.001	2.7/13
Average			2.52 ±0.09	0.006 ±0.001	
20-30%	0	[-1.99;-1.73]	2.61 ±0.10	0.009 ±0.003	2.7/13
20-30%	1	[-1.72;-1.36]	3.10 ±0.13	0.009 ±0.003	6.9/13
20-30%	2	[-1.35;-0.83]	3.61 ±0.14	0.005 ±0.002	4.5/13
20-30%	3	[-0.80;-0.03]	4.20 ±0.16	0.003 ±0.002	4.9/13
Average			3.38 ±0.12	0.007 ±0.002	
30-40%	0	[-1.99;-1.73]	2.74 ±0.11	0.014 ±0.005	1.0/13
30-40%	1	[-1.72;-1.36]	3.32 ±0.13	0.008 ±0.004	17/13
30-40%	2	[-1.35;-0.83]	3.79 ±0.15	0.009 ±0.003	5.3/13
30-40%	3	[-0.80;-0.03]	4.56 ±0.18	0.005 ±0.002	1.8/13
Average			3.60 ±0.13	0.009 ±0.003	
40-50%	0	[-1.99;-1.73]	2.83 ±0.11	0.016 ±0.007	5.0/13
40-50%	1	[-1.72;-1.36]	3.54 ±0.13	0.006 ±0.005	7.2/13
40-50%	2	[-1.35;-0.83]	3.82 ±0.15	0.007 ±0.004	4.9/13
40-50%	3	[-0.80;-0.03]	4.48 ±0.17	0.006 ±0.003	1.9/13
Average			3.67 ±0.13	0.009 ±0.004	

Figure E.9: Fluctuations vs. multiplicity for BRAG simulated FRITIOF events with various centrality cuts. The upper left plot show the fluctuations with a centrality cut from 10 to 20%, upper right from 20 to 30%, lower left from 30 to 40% and lower right from 40 to 50% central events. Error bars are statistical and the values for the fits are listed in the table below figure.

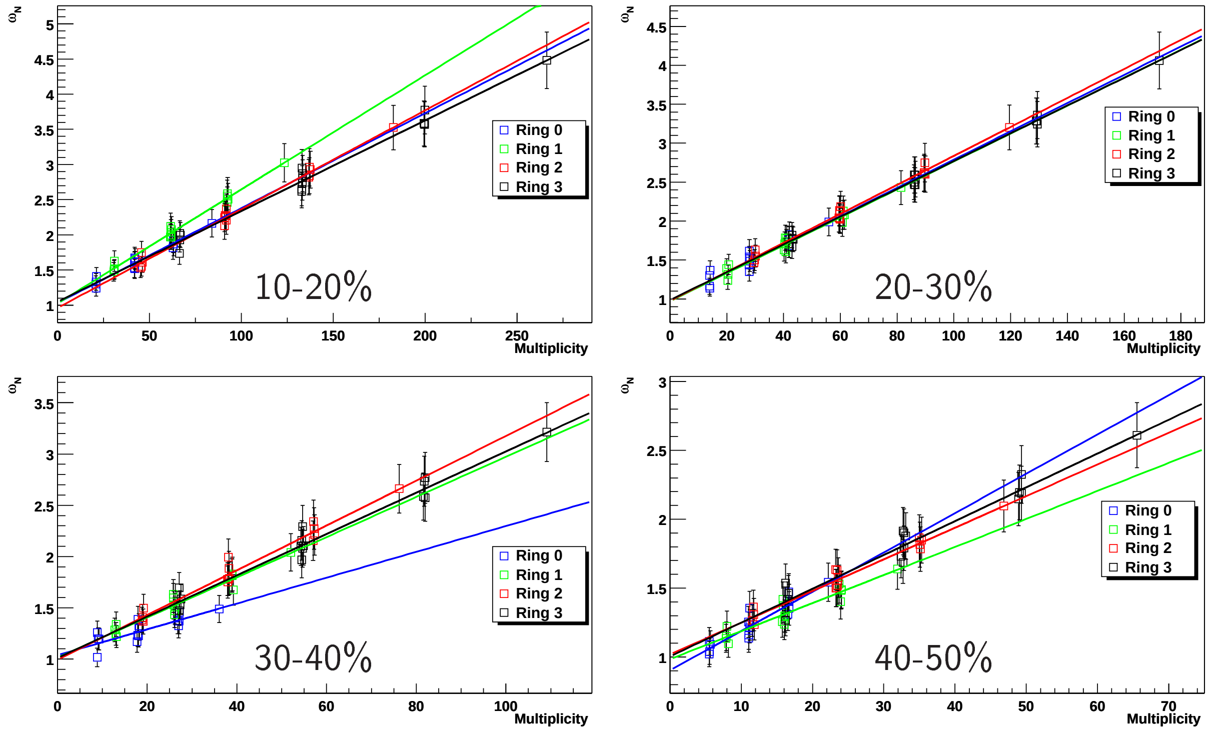

Centrality	Ring	η	$\omega_n(\eta)$	$\omega_{N_p}/\overline{N}_p$	χ^2/ndf
10-20%	0	[-1.99;-1.73]	1.03 ±0.09	0.013 ±0.002	2.3/13
10-20%	1	[-1.72;-1.36]	1.02 ±0.11	0.016 ±0.002	1.3/13
10-20%	2	[-1.35;-0.83]	0.96 ±0.12	0.014 ±0.001	2.2/13
10-20%	3	[-0.80;-0.03]	1.05 ±0.14	0.013 ±0.001	3.3/13
Average			1.02 ±0.10	0.014 ±0.001	
20-30%	0	[-1.99;-1.73]	0.97 ±0.08	0.018 ±0.003	5.8/13
20-30%	1	[-1.72;-1.36]	0.97 ±0.09	0.018 ±0.003	3.1/13
20-30%	2	[-1.35;-0.83]	0.97 ±0.11	0.019 ±0.002	1.5/13
20-30%	3	[-0.80;-0.03]	0.99 ±0.13	0.018 ±0.002	0.9/13
Average			0.98 ±0.09	0.018 ±0.002	
30-40%	0	[-1.99;-1.73]	1.04 ±0.07	0.013 ±0.004	6.2/13
30-40%	1	[-1.72;-1.36]	1.02 ±0.09	0.020 ±0.003	3.0/13
30-40%	2	[-1.35;-0.83]	0.99 ±0.10	0.022 ±0.003	2.5/13
30-40%	3	[-0.80;-0.03]	1.01 ±0.11	0.020 ±0.002	3.4/13
Average			1.02 ±0.08	0.019 ±0.002	
40-50%	0	[-1.99;-1.73]	0.90 ±0.07	0.029 ±0.006	3.7/13
40-50%	1	[-1.72;-1.36]	0.98 ±0.08	0.020 ±0.004	3.0/13
40-50%	2	[-1.35;-0.83]	1.02 ±0.09	0.023 ±0.004	1.8/13
40-50%	3	[-0.80;-0.03]	1.00 ±0.10	0.025 ±0.003	4.5/13
Average			0.98 ±0.08	0.024 ±0.004	

Figure E.10: Fluctuations vs. multiplicity for simulated **HIJING** events **without using BRAG** and with various centrality cuts. The different centrality cuts are shown on figures and one conclusion from this figure is that $\omega_n(\eta)$ is 1 (within the error), i.e. the measured fluctuations are purely statistical. Error bars are statistical and the values for the fits are listed in the table below figure.

E.3 Summarized $\omega_{N_p}/\overline{N}_p$ Estimates

The estimations on the slope ($\omega_{N_p}/\overline{N}_p$) of data and simulations in figures E.11, E.12, E.13 and E.14 are shown in this section.

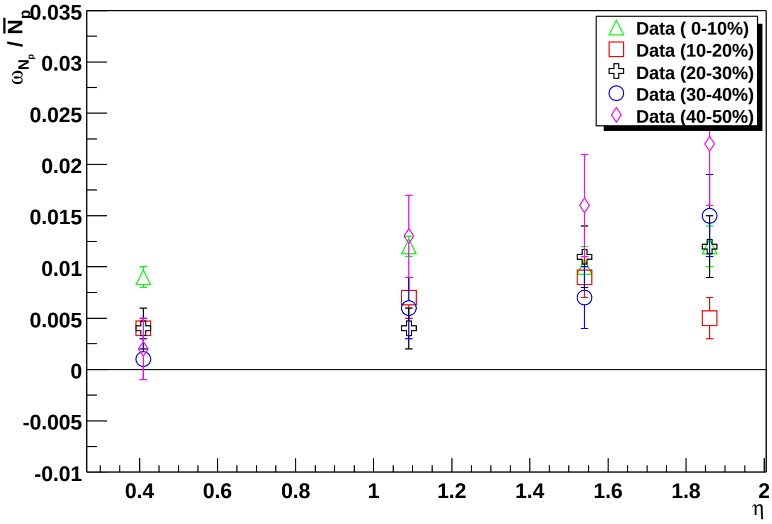

Figure E.11: $\omega_{N_p}/\overline{N}_p$ for **data**. The slope the peripheral events (0-50%) is increasing slightly, while for the more central is consistent with a constant value. The uncertainties are from the tables in figures E.4 and E.3.

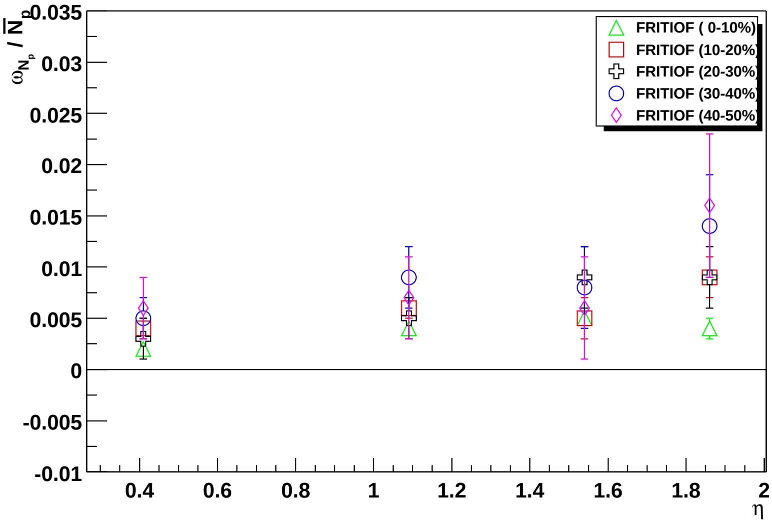

Figure E.12: $\omega_{N_p}/\overline{N}_p$ for **BRAG simulated FRITIOF** events. The slopes for the FRITIOF event are more consistent within the same η bin, when compared to the ones in figure E.11. The uncertainties are from the tables in figures E.8 and E.9.

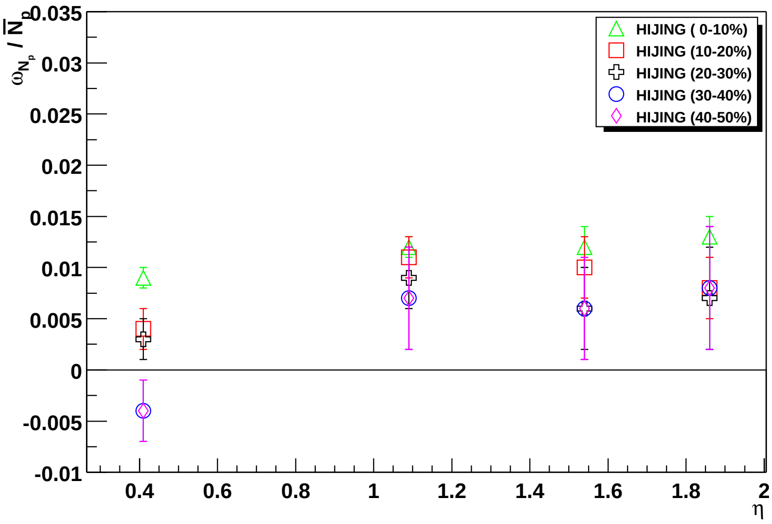

Figure E.13: $\omega_{N_p}/\overline{N}_p$ for **BRAG simulated HIJING** events. The vertex acceptance is here $\mid z \mid \leq$ **2.5 cm**. Again slopes are consistent, except for events located at the central ring. For this η the more peripheral events have negative slopes. The uncertainties are from the tables in figures 7.10 and E.5.

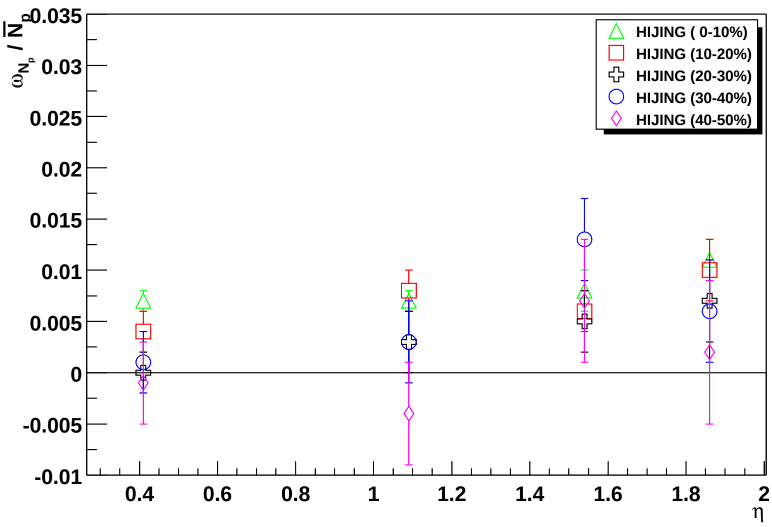

Figure E.14: $\omega_{N_p}\overline{N}_p$ for **BRAG simulated HIJING** events. The vertex acceptance is here $\mid z \mid \leq$ **0.45 cm**. As in figure E.13 negative slopes are shown. But now only for the most peripheral events (40-50%). The uncertainties are from the tables in figures E.6 and E.7.

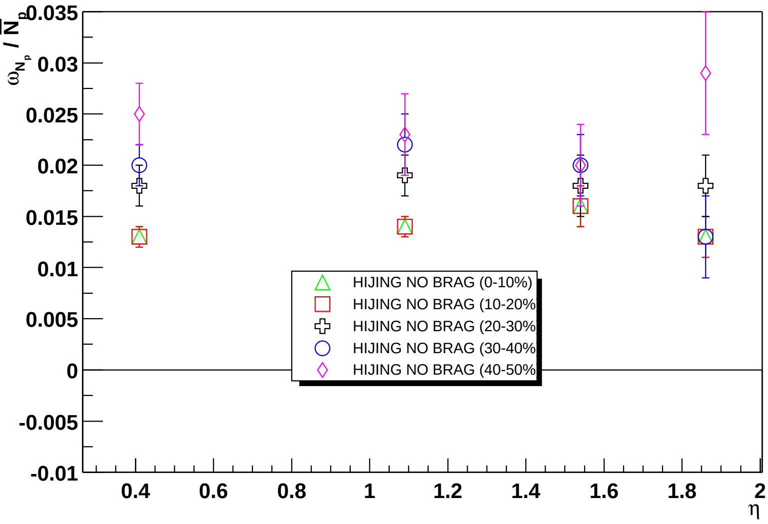

Figure E.15: $\omega_{N_p}\overline{N}_p$ for **raw HIJING** events. The uncertainties are from the tables in figures 7.11 and E.10

E.4 Correcting Intrinsic Fluctuations

Correction factors for intrinsic fluctuations evaluated in section 7.4.1. The values are used to scale figures 7.15 and 7.16 to figures 7.17 and 7.18.

Centrality	η	$\omega_{Data}/\omega_{HIIJNG}$
0-10%	[-1.99;-1.73]	0.76
0-10%	[-1.72;-1.36]	0.79
0-10%	[-1.35;-0.83]	0.87
0-10%	[-0.80;-0.03]	0.91
10-20%	[-1.99;-1.73]	0.66
10-20%	[-1.72;-1.36]	0.65
10-20%	[-1.35;-0.83]	0.70
10-20%	[-0.80;-0.03]	0.68
20-30%	[-1.99;-1.73]	0.56
20-30%	[-1.72;-1.36]	0.58
20-30%	[-1.35;-0.83]	0.67
20-30%	[-0.80;-0.03]	0.63
30-40%	[-1.99;-1.73]	0.60
30-40%	[-1.72;-1.36]	0.56
30-40%	[-1.35;-0.83]	0.58
30-40%	[-0.80;-0.03]	0.63
40-50%	[-1.99;-1.73]	0.64
40-50%	[-1.72;-1.36]	0.55
40-50%	[-1.35;-0.83]	0.60
40-50%	[-0.80;-0.03]	0.64

Table E.1: Correction factors for intrinsic fluctuations. The values are used to scale figures 7.15 and 7.16 to figures 7.17 and 7.18.

Appendix F

The BRAHMS Collaboration

I. G. Bearden[8], D. Beavis[1], C. Besliu[11], Y. Blyakhman[7], J. Brzychczyk[4], B. Budick[7], H. Bøggild[8], C. Chasman[1], C. H. Christensen[8], P. Christiansen[8], J. Cibor[5], R. Debbe[1], E. Enger[2], J. J. Gaardhøje[8], K. Grotowski[4], K. Hagel[9], O. Hansen[8], A. Holm[8], A. K. Holme[2], H. Ito[12], E. Jakobsen[8], A. Jipa[11], J. I. Jørdre[10], F. Jundt[3], C. E. Jørgensen[8], T. Keutgen[9], E. J. Kim[6], T. Kozik[4], T. M. Larsen[2], J. H. Lee[1], Y. K. Lee[6], G. Løvhøiden[2], Z. Majka[4], A. Makeev[9], B. McBreen[1], M. Mikelsen[2], M. Murray[9], J. Natowitz[9], B. S. Nielsen[8], K. Olchanski[1], J. Olness[1], D. Ouerdane[8], R. Płaneta[4], F. Rami[3], D. Röhrich[10], B. H. Samset[2], D. Sandberg[8], S. J. Sanders[12], R. A. Sheetz[1], Z. Sosin[4], P. Staszel[8], T. F. Thorsteinsen[10†], T. S. Tveter[2], F. Videbæk[1], R. Wada[9], A. Wieloch[4], and I. S. Zgura[11]

[1] Brookhaven National Laboratory, Upton, New York 11973, USA
[2] University of Oslo, Department of Physics, Oslo, Norway
[3] Institut de Recherches Subatomiques and Université Louis Pasteur, Strasbourg, France
[4] Jagiellonian University, Krakow, Poland
[5] Institute of Nuclear Physics, Krakow, Poland
[6] Johns Hopkins University, Baltimore, Maryland 21218, USA
[7] New York University, New York, New York 10003, USA
[8] Niels Bohr Institute, University of Copenhagen, Denmark
[9] Texas A&M University, College Station,Texas 77843, USA
[10] University of Bergen, Department of Physics, Bergen, Norway
[11] University of Bucharest, Romania
[12] University of Kansas, Lawrence, Kansas 66049, USA
[†] *Deceased*

Bibliography

[1] J. Bondorf et al., *Hot and Dense Matter*, Niels Bohr Institute, Copenhagen, 1996

[2] S. Weinberg, *The First Three Minutes - A Modern View of the Origin of the Universe*, Basic Books, 1973

[3] K. Krane, *Introductory Nuclear Physics*, John Wiley & Sons., New York, 1988

[4] J. Brehm & William J. Mullin, *Introduction to the structure of Matter*, John Wiley & Sons., 1989

[5] B. Martin & G. Shaw, *Particle Physics*, John Wiley & Sons., 1992

[6] B. Samset, *Vertex Determination in the BRAHMS Experiment and Measurements of Centrality Dependent Charged Particle Production in Au+Au Collisions at* $\sqrt{s_{NN}}$ *= 130 GeV*, Master Thesis, University of Bergen, 2001

[7] E. Laermann, *Recent Results from Lattice QCD Simulations*, Nucl. Phys. **A610**, 1996 1c

[8] J. Harris, *Relativistic Heavy Ion Physics and the Relativistic Heavy Ion Collider*. Prepared for Lake Louise Winter Institute: Quantum Chromo Dynamics, Lake Louise, Alberta, Canada, 15-21 Feb, 1998

[9] J. I. Jørdre, *Performance of the Time Projection Chambers of the BRAHMS experiment at RHIC*, Master Thesis, University of Bergen, 2000

[10] C. Jørgensen, *Charged Particle Production in Au + Au Collisions at* $\sqrt{s_{NN}}$ *= 130 GeV*, Master Thesis, Niels Bohr Institute, Copenhagen, 2001

[11] E. L. Feinberg, *Landau Hydrodynamical Model as a Basis for Treating Relativistic Heavy Ion Collisions*, Lebedev Inst., 1991.

[12] F. Videbæk & O. Hansen, *Highly relativistic nucleus-nucleus collision: The central rapidity region*, Phys. Rev. **C52** 2684, 1995

[13] I. G. Bearden et al. (BRAHMS Collaboration), *Rapidity dependence of antiproton to proton ratios in Au+Au collisions at* $\sqrt{s_{NN}}$ *= 130 GeV*, Phys. Rev. Lett. **87** 112305, 2001

[14] C. Adler et al. (STAR Collaboration), *midrapidity anti-proton to proton ratio from Au+Au collisions at* $\sqrt{s_{NN}}$ *= 130 GeV*, submitted to Phys. Rev Lett. **86** 4778-4782, 2001

[15] H. Bøggild et al. *Coulomb effect on single particle distributions*, Phys. Lett. **B373** 339, 1996

[16] J. Bjorken, *Highly relativistic nucleus-nucleus collisions: The central rapidity region*, Phys. Rev. 27, p. 140, 1983

[17] T. Matsui and H. Satz, *J/ψ Suppression by Quark-Gluon Plasma Formation*, Phys. Lett. **B178** 416, 1986

[18] ALICE Collaboration: `http://alicewww.cern.ch/`

[19] M. C. Abreu, *Evidence for deconfined quarks and gluons from the J/Ψ supression pattern measured in Pb + Pb collisions at CERN-SPS*, Phys. Lett. **B477** 28, 2000

[20] NA50 Collaboration, *Anomalous J/Ψ suppression in Pb-Pb Collisions at 150 A GeV/c*, Quark Matter Conference, 1996

[21] I. G. Bearden et al., *Strange Meson Enhancement in PbPb Collisions.* nucl-ex 9907013, 1999

[22] F. Antinori et al., *Production of strange and multistrange hadrons in nucleus nucleus collisions at the SPS*, Nucl. Phys.,**A661** 130-139, 1999

[23] M. M. Aggarwal et al. (WA98 Collaboration), Phys. Rev. Lett. **83** 926, 1999

[24] STAR HTML Documentation: `http://www.star.bnl.gov/`

[25] C. Adler et al. (STAR Collaboration), *Multiplicity Distribution and Spectra of Negatively Charged Hadrons in Au + Au Collisions at $\sqrt{s_{NN}} = 130$ GeV*, Phys. Rev. Lett. **87**, 112303, 2001

[26] K. Adcox et al. (PHENIX Collaboration), *Measurement of the midrapidity transverse energy distribution from $\sqrt{s_{NN}} = 130$ GeV Au+Au collisions at RHIC*, Phys. Rev. Lett. **87**, 052301, 2001

[27] K. Adcox et al. (PHENIX Collaboration), *Suppression of Hadrons with Large Transverse Momentum in Central Au+Au Collisions at $\sqrt{s_{NN}} = 130$*, Submitted to Phys. Rev. Lett. 2001-07-05, nucl-ex 0109003

[28] B. B. Bach et al. (PHOBOS Collaboration), *Ratios of charged antiparticles to particles near midrapidity in Au+Au collisions at $\sqrt{s_{NN}} = 130$ GeV*, Phys. Rev. Lett. **87**, 102301, 2001

[29] PHENIX HTML Documentation: `http://www.phenix.bnl.gov/`

[30] B. B. Bach et al. (PHOBOS Collaboration), *Charged particle multiplicity near midrapidity in central Au+Au collisions at $\sqrt{s_{NN}} = 56$ and 130 GeV*, Phys. Rev. Lett. **85**, 3100, 2000

[31] I. G. Bearden et al. (BRAHMS Collaboration) *Charged particle densities from Au+Au collisions at $\sqrt{s_{NN}} = 130$ GeV*, Phys. Lett. **B523** 227-233, 2001

[32] Bearden et al. (BRAHMS Collaboration) *Charged particle densities from Au+Au collisions at $\sqrt{s_{NN}} = 200$ GeV*, nucl-ex 00112001, Submitted to Phys. Rev. Lett. , 2001

[33] K. Adcox et al. (PHENIX Collaboration), *Centrality Dependence of Charged Particle Multiplicity in Au + Au Collisions at* $\sqrt{s_{NN}}$ *= 130 GeV*, Phys. Rev. Lett. **86**, 3500-3505, 2001

[34] PHOBOS HTML Documentation: `http://www.phobos.bnl.gov/`

[35] S. Voloshin for the STAR Collaboration, *Multiplicity and Mean Transverse Momentum Fluctuations in Au + Au Collisions at RHIC*, nucl-ex 0109006, 2001

[36] A. Hansen, *Light Nuclei Production In Ultra Relativistic Heavy Ion Collisions*, Ph. D. Thesis, Niels Bohr Institute, 1999

[37] L. A. Pshenichnov et al., *Mutual heavy ion dissociation in peripheral collisions at ultrarelativistic energies*, nucl-th 0101035, 2001

[38] F. Videbæk, *Results from the BRAHMS Experiment at RHIC*, Proceedings of the QM01 Conference, Stony Brook, 2001

[39] J. Binney et al, *The Theory of Critical Phenomena*, Oxford University Press, Oxford, 1992

[40] R. Debbe *Stop the press!!: Rings out of RICH*, Internal BRAHMS Analysis Note #15, 2000

[41] H. Ito and S. Sanders *Charged Particle Multiplicities from Si Strip Detectors and Scintillator Tiles*, Internal BRAHMS Analysis Note #26, 2000

[42] G. Bali et al., *Confining Forces and String Formation From the Lattice*, hep-lat 9410002

[43] H. Heiselberg, private communication.

[44] J. J. Gaardhøje, private communication.

[45] J. Whitmore, Phys. Rep 27 187, 1976

[46] H. Bøggild et al., Annu. Rev. Nucl. Sci. 451, 1974

[47] G. J. Alner et al. (UA5 Collaboration), Phys. **C33**, 1986

[48] I. Mishustin, Private Communication, Niels Bohr Institute, 2000

[49] H. Heiselberg, *Event-by-Event Physics in Relativistic Heavy-Ion Collisions*, Physics Reports 351, 161-194, 2001

[50] S. Jeon and V. Koch, *Fluctuations of Particle Ratios and the Abundance of Hadronic Resonances*, Phys. Rev. Lett. **83** 5435, 1999

[51] S. Jeon and V. Koch, *Charged Particle Ratio Fluctuation as a Signal for QGP*, Phys. Rev. Lett. **85** 2076, 2000

[52] M. Asakawa, U. Heinz and B. Müller, *Fluctuation Probes of Quark Confinement*, Phys. Rev. Lett. **85** 2072, 2000

[53] RHIC Design Manual, *RHIC Design Manual*, `http://www.rhichome.bnl.gov/NT-share/rhicdm/`, Brookhaven National Laboratory, New York, Rev. Date: October 2000

[54] H. Appelshäuser et al. (NA49 Collaboration), *Event-by-event fluctuations of average transverse momentum in central Pb+Pb collisions at 158 GeV per Nucleon*, hep-ex 9904014, 2001

[55] M. M. Aggarwal et al. (WA98 Collaboration), *Event-by-Event Fluctuations in Particle Multiplicities and Transverse Energy Produced in 158·A GeV Pb+Pb Collisions*, nucl-ex 0108029, 2001

[56] S. V. Afanasev et al. (NA49 Collaboration), *Event-by-Event fluctuations in Pb + Pb Collisions at the CERN SPS*, Published in *Providence 1999, QCD and multiparticle production* 413-418, Aug 1999.

[57] I. G. Bearden et al. (BRAHMS Collaboration), *BRAHMS Conceptual Design Report*, Brookhaven National Laboratory, New York, 1994, updated 1995

[58] I. G. Bearden et al. (BRAHMS Collaboration), *The BRAHMS Experiment at RHIC*, Brookhaven National Laboratory, New York, 2001

[59] Particle Data Group, *Particle Physics Booklet*, Springer, 2000

[60] P. Christiansen, *Pion interferometry in central 158 GeV/Nucleon Pb+Pb collisions at the CERN SPS*, Master Thesis, University of Copenhagen, 1999

[61] P. Staszel, *Drift chambers for BRAHMS experiment at RHIC facility* Internal BRAHMS note

[62] P. Staszel, *Short note on the analysis of April T3 test run*, Internal BRAHMS Analysis Note #34, 2001

[63] Y. Blyakhman, *Beam-Beam Counters and Charged Particle Multiplicity in the Brahms Experiment at RHIC*, Ph. D Thesis, University of New York, 2001

[64] S. Sanders, *Charged Particle Multiplicities at BRAHMS*, 17^{th} Winter Workshop on Nuclear Dynamics, Park City, Utah, 2001

[65] M. Murray, *Zero Degree Calorimetry for BRAHMS*, Internal BRAHMS Note #14, 1998

[66] M. Murray, *The RHIC Zero Degree Calorimeters*, nucl-ex 0008005, 2000

[67] W. R. Leo, *Techniques for Nuclear and Particle Physics Experiments*, Springer-Verlag, 1994

[68] BRAHMS Collaboration: `http://pii3.brahms.bnl.gov/ brahmlib/`

[69] GEANT HTML Documentation: `http://wwwinfo.cern.ch/asd/geant4/geant4.html`

[70] A. Galoyan et al., *Simulation of Nucleus-Nucleus Interactions in the Framework of the FRITIOF Model at the Energy of 3.3 GeV/nucleon* nucl-th 0010083, 2000

[71] H. Pi, *An Event Generator for Interactions Between Hadrons and Nuclei - FRITIOF Version 7*, Computer Physics Communiations, 71:173, 1992

[72] X. Wang and M. Gyulassy, Comput. Phys. Commun. 83(1994) 307

[73] Pythia HTML Documentation:
`http://www.thep.lu.se/~torbjorn/Pythia.html`

[74] S. A. Bass et al., *Microscopic Models for Ultrarelativistic Heavy Ion Collisions*, Prog. Part. Nucl. Phys. **41**, 225, nucl-th/9803035

[75] BRAHMS Collaboration, BRAT HTML Documentation:
`http://pii3.brahms.bnl.gov/~brahmlib/brat/`

[76] J. J. Gaardhøje, *Analysis of Charged particle Multiplicity data*, Internal BRAHMS Analysis Note #11, 2000

[77] H. Ito & S. Sanders *Charged Particle Multiplicities from Si Strip Detectors and Scintillator Tiles*, Internal BRAHMS Analysis Note #26, 2001

[78] H. Heiselberg & A. D. Jackson, *Anomalous Multiplicity Fluctuations from Phase Transitions in Heavy Ion Collisions*, nucl-ex 0006021, 2000

[79] C. H. Christensen, ROOT HTML Documentation on Principal Components Analysis
`http://root.cern.ch/root/html/TPrincipal.html`

[80] M. Sørensen, *En Introduktion til Sandsynlighedsregning*, Matematisk Institut, Københavns Universitet, 2000

[81] J. H. Lee, *From ADC to* $dN/d\eta$, Internal BRAHMS Analysis Note #14, 2000

[82] E. Jakobsen, *Estimation of Background Corrections in Multiplicity Array*, Internal BRAHMS Analysis Note #20, 2000

[83] C. Adler et al., *Identified Particle Elliptic Flow in Au+Au Collisions at* $\sqrt{s_{NN}} = 130$ *GeV*, Phys. Rev. Lett. **87** 182301, nucl-ex 0107003, 2001

[84] H. Heiselberg, *Event-By-Event Physics in Relativistic Heavy-Ion Collisions*, Physics Reports 351, 161-194, 2001

[85] R. Debbe, *Calibration of Tiles with Cosmic Rays*, Internal BRAHMS Analysis Note #12, 2000

[86] P. Bevington & D. Robinson, *Data Reduction and Error Analysis for the Physical Sciences*, McGraw-Hill, ISBN 0-07-113845-5, 1994

[87] Private Communication, C. H. Christensen and P. Christiansen, Niels Bohr Institute, 2001